

**Monte Carlo Simulation of Transition
Radiation and Detectors in High Energy
Physics**

Steven John Aplin¹

The thesis is submitted in partial fulfilment of the requirements for
the award of the degree of Doctor of Philosophy of the University of Portsmouth.

In collaboration with the Deutsch Elektronen Synchrotron

January, 2004

¹E-mail steven.aplin@mail.desy.de

Abstract

This thesis describes a study of the electromagnetic phenomena of transition radiation, the radiation which is emitted when a charged particle traverses the interface between two media of differing dielectric properties.

The main goal of this study is the mathematical modelling and simulation of transition radiation under relativistic conditions for particle identification in experimental high energy physics.

Of particular interest is the implementation of a mathematical model in the detector description and simulation tools of experimental high energy physics. The mathematical model developed has been verified using experimental data obtained from a prototype of a transition radiation detector.

The application of the mathematical model within a high energy physics experiment is demonstrated by the detailed analysis and optimisation of a transition radiation detector for the high energy physics experiment, HERA-*B* “An Experiment to Study CP Violation in the *B* System using an Internal Target at the HERA Proton Ring” which was based on a full simulation within the complete frame work of the experiment.

The application of the mathematical model for use in the further development of transition radiation detectors is demonstrated in the analysis of a new concept of transition radiation detector. The concept uses a strong magnetic field to separate transition radiation photons from the incident charged particle and is presented for use at TESLA, “The Superconducting Electron-Positron Linear Collider with an Integrated X-Ray Laser Laboratory”.

Contents

1	Transition Radiation - Theory and Analysis of Physical Models	6
1.1	Theory of Transition Radiation	6
1.2	Wave Theory of Transition Radiation	21
1.2.1	General Case	21
1.2.2	Vacuum to Medium Case	25
1.2.3	Medium to Vacuum Case	27
2	Mathematical Modelling of Transition Radiation	31
2.1	Practical Theory of Transition Radiation.	31
2.1.1	Analysis of Transition Radiation from a single interface . .	35
2.2	Theory of Transition Radiation for Periodic Structures	42
2.2.1	Generation of Transition Radiation in a Periodic Structure	42
2.2.2	Analysis of Transition Radiation in Periodic Structures . .	48
2.3	Propagation of Transition Radiation in Periodic Structures	57
2.3.1	Main Processes	57
2.3.2	Analysis of Transition Radiation Spectrum Including Ab- sorption Processes within a Periodic Structure	61
2.4	Detection of Transition Radiation	65
2.4.1	Detection of X-ray Transition Radiation	65
2.4.2	Background Signal	69
2.4.3	Analysis of Ionisation losses in thin gas proportional chambers	77

2.5	Monte Carlo Simulation of Transition Radiation for High Energy Physics	82
2.5.1	Simulation Programme	82
2.5.2	Analysis and verification of MC Simulation	87
3	Analysis and Optimisation of the HERA-B TRD	100
3.1	Introduction	100
3.1.1	HERA Accelerator Facility	101
3.1.2	The HERA- <i>B</i> detector	103
3.2	HERA-B TRD	115
3.2.1	Analysis and Optimisation of the HERA-B TRD	116
4	Proposal of a TRD for TESLA	126
4.1	Introduction	126
4.2	Physics of the TESLA Project	127
4.3	Linear electron-positron collider at an energy of 500 GeV to 1 TeV	128
4.3.1	TESLA Spectrometer	129
4.4	Transition Radiation Detector for the TESLA Experiment	135
4.4.1	New Concept of a TRD	136
4.4.2	TESLA TRD design and analysis	138
5	Conclusion	152

List of Figures

1.1	<i>A schematic illustration of transition radiation emission from a charge e moving with velocity v along the z axis, normally incident upon the boundary between vacuum and an ideal conductor of dielectric constant ε_1, which lies along the y axis. P denotes the point of observation and θ the angle at which the transition radiation is emitted at a frequency of ω.</i>	8
1.2	<i>A schematic illustration of transition radiation emission from a charge e moving with velocity v along the z axis, normally incident upon the boundary between media with dielectric constants ε_1 and ε_2, which lies along the y axis. P denotes the point of observation and θ the angle at which the transition radiation is emitted at a frequency of ω.</i>	22
2.1	<i>The computed differential yield (keV/keV) as a function of $\hbar\omega$, the transition radiation photon energy, for a charged relativistic particle with a Lorentz factor $\gamma = 10000$ traversing a single mylar-air interface. $\hbar\omega_1\gamma = 10$ keV and $\hbar\omega_2\gamma = 250$ keV.</i>	36
2.2	<i>The computed differential yield (keV/keV) as a function of $\hbar\omega$, the transition radiation photon energy, for a charged relativistic particle traversing a single mylar-air interface, for different Lorentz factor, over the range $\gamma = 100 - 20,000$ (increasing left to right).</i>	37

2.3	<i>Cylindrical plot showing the angular distribution of transition radiation intensity from a relativistic charged particle ($\gamma = 1800$) normally incident on an interface between two dielectrics, whose direction is denoted by the arrow marked e. It can be seen that the emission of transition radiation photons is azimuthally symmetric about the trajectory of the particle and is confined to a narrow forward cone.</i>	39
2.4	<i>Angular distribution of transition radiation intensity from a relativistic charged particle for the range $\gamma = 1000 - 2000$. The distribution for $\gamma = 1800$ is the projection of the cylindrical plot from Fig. 2.3. It can be seen that the emitted radiation is peaked in the forward direction at an angle $\theta \sim \gamma^{-1}$.</i>	41
2.5	<i>Analogy of interference effects from two interfaces producing transition radiation and double slit interference</i>	43
2.6	<i>Schematic diagram of a charged particle traversing a periodic structure of slabs with thickness l_1 consisting of a medium with dielectric constant ϵ_1 spaced at a distance of l_2 within a medium with dielectric constant ϵ_2. l_1 and l_2 remain constant throughout the periodic structure. R_k (R_{k+1}) represents the distance from point at which the particle traverses foil k ($k + 1$) to the point of observation P. θ_k (θ_{k+1}) represents the angle between R_k (R_{k+1}) and the particle trajectory.</i>	44

2.7	<i>The computed differential yield (keV/keV) normalised to the number of interfaces as a function of $\hbar\omega$, the transition radiation photon energy, for a charged relativistic particle traversing a periodic structure of mylar-air interfaces, for different Lorentz factor, over the range $\gamma = 100 - 20,000$ (increasing left to right as in Fig. 2.1). Modulation of the spectrum due interference is clearly visible. . . .</i>	50
2.8	<i>The computed differential yield (keV/keV) normalised to the number of interfaces as a function of $\hbar\omega$, the transition radiation photon energy, for a charged relativistic particle traversing a periodic structure of mylar-air interfaces, for different l_1.</i>	52
2.9	<i>The computed differential yield (keV/keV) normalised to the number of interfaces as a function of $\hbar\omega$, the transition radiation photon energy, for a charged relativistic particle traversing a periodic structure of mylar-air interfaces, for different l_2.</i>	53
2.10	<i>Surface plot showing the energy of the last maximum as a function of l_1 and l_2 for 20 GeV electrons.</i>	54
2.11	<i>Surface plot showing the energy of the last maximum as a function of l_1 and l_2 for 50 GeV electrons.</i>	55
2.12	<i>Mass attenuation coefficient of Photons in Xe, over the energy range 1-500 keV (Berger, Hubbell, Seltzer, Coursey & Zucker 1999).</i>	59
2.13	<i>Mass attenuation coefficient of Photons in Mylar over the energy range 1-500 keV(Berger et al. 1999).</i>	64

2.14	<i>The computed differential yield (keV/keV) normalised to the number of interfaces as a function of $\hbar\omega$, the transition radiation photon energy, for a charged relativistic particle traversing a periodic structure of mylar-air interfaces taking absorption within the radiator into account, for different Lorentz factor, over the range $\gamma = 100 - 20,000$ (increasing left to right as in Fig. 2.1).</i>	66
2.15	<i>Mass attenuation coefficients as a function of X-ray energy for Xenon (black line) and Krypton (grey line) over the energy range 1-500 keV (Berger et al. 1999).</i>	68
2.16	<i>The computed differential yield (keV/keV) normalised to the number of interfaces as a function of $\hbar\omega$, the transition radiation photon energy, for a charged relativistic particle traversing a periodic structure of mylar-air interfaces taking absorption in Xe into account, for different Lorentz factor, over the range $\gamma = 100 - 20,000$ (increasing left to right as in Fig. 2.1). The effect of the characteristic absorption edges of the L and K shells in Xe on the spectrum is clearly visible at 4.8 keV and 35 keV respectively.</i>	70
2.17	<i>Classical Landau distribution (smooth curve) of dE/dx losses and that obtained from MC simulation (histogram). The MC distribution is clearly wider than the Landau distribution and the influence of the tail in the region 4-6 keV is also more significant for MC .</i>	81
2.18	<i>Schematic Flow diagram showing the interaction between the different programmes needed for full simulation of transition radiation</i>	83

2.19	<i>Experimental test-beam area at DESY (above) and the experimental setup from TRD prototype studies (below). The two overlapping scintillation counters used for coincidence triggering are labled as S1 and S2, the spectroscopic scintillation counter used for the veto is labelled as SA.</i>	88
2.20	<i>The number of transition radiation hits vs threshold for different transition radiation radiators as measured on a test beam, and comparison with Monte Carlo predictions (solid line) (Egorychev, Savelev & Aplin 2000).</i>	91
2.21	<i>Histograms showing Energy deposit spectrums from prototype studies without radiator. Experimental data is represented by triangular point markers and MC data is represented by the solid line.</i>	93
2.22	<i>Histograms showing Energy deposit spectrums from prototype studies with radiator. Experimental data is represented by triangular point markers and MC data is represented by the solid line.</i>	95
2.23	<i>The normalised difference between MC and experimental data for each energy bin between 1-20 keV, without radiator (ionisation losses only).</i>	96
2.24	<i>The normalised difference between MC and experimental data for each energy bin between 1-20 keV, with radiator (including transition radiation process).</i>	97
2.25	<i>The number of transition radiation hits vs threshold for different transition radiation radiators as measured on a test beam, and comparison with Monte Carlo predictions (solid line) including new Monte Carlo results for the new polypropylene fibre radiator.</i>	98
3.1	<i>Schematic overview of the HERA storage ring</i>	102

3.2	<i>(Schematic overview of the HERA storage ring (above). Filling scheme of proton bunches in HERA. 180 of the 220 bunches are filled divided into three trains of 60 bunches. The bunches are separated by 96 ns (below).</i>	102
3.3	<i>Schematic overview of the HERA-B spectrometer</i>	104
3.4	<i>The target system consists of eight wire arranged into two stations. Each wire is independently steered by an integrated servo system. To increase the interaction rate the wires are moved further into the beam halo, to reduce the interaction rate the wire are moved out</i>	106
3.5	<i>Schematic diagram of the VDS layout. The VDS consists of eight superlayer. Each super layer consists of eight single or double sided silicon micro-strip detectors.</i>	108
3.6	<i>Overview of the main tracking system of the HERA-B spectrometer. The superlayers of both the ITR and OTR are shown in their three distinct groupings. The outermost regions of the angular coverage are covered by the OTR and the innermost regions by the ITR.</i>	108
3.7	<i>The layout and segmentation of the ECAL. The three regions of different cell size are shown for the Inner, Middle and Outer ECAL</i>	111
3.8	<i>The MUON system consists of three iron loaded concrete hadron absorber and four superlayers In the region of higher occupancy close to the beam gas pixel chambers are used, while the outer lying region is covered by tube chambers equipped with both wire and pad readout.</i>	112
3.9	<i>Overview of the different trigger levels and their associated rate reduction and decision times</i>	114

3.10	<i>Schematic view of the geometric implementation in GEANT of the HERA-B TRD. KEY: TRSL = overall GEANT Volume, TR01-2 = TRD superlayers, TRB* = TRD module (straws embedded in radiator material), TRTU = straw tube proportional chambers . .</i>	118
3.11	<i>A full MC event in the HERA-B spectrometer</i>	119
3.12	<i>Shown are both Super-layers TR01 and TR02 and their orientation to one another</i>	120
3.13	<i>TRD in front of OTR Super-layer TC02, all other Sub systems have been removed to give a clear view</i>	121
3.14	<i>Histograms showing the energy distribution for Straw tubes (top) and transition radiation hits distribution (bottom) for electrons and pions 30 GeV/c.</i>	123
3.15	<i>MC calculation of the Rejection Power vs electron efficiency for the HERA-B TRD</i>	124
4.1	<i>Schematic view of the TESLA spectrometer, the near sides of each detector have been cut away to allow the detectors at different depths to be seen</i>	130
4.2	<i>Schematic view of the transition radiation radiator and Si-pixel TRD concept</i>	139
4.3	<i>Separation, δ, between particle track and transition radiation photons for proposed Si-pixel TRD geometry. Values of δ - for a radiator thickness of 8 cm at $\theta = 90^\circ$</i>	141
4.4	<i>Two dimensional plot of δ vs absorbed transition radiation photons energy ($\theta = 90^\circ$) for electrons with a momentum of 30 GeV/c . .</i>	142
4.5	<i>The energy spectrum of the transition radiation photons absorbed in Si-pixel detector ($p = 30$ GeV/c, $\theta = 90^\circ$.)</i>	143

4.6	<i>Distribution of the number of detected transition radiation photons ($p = 30 \text{ GeV}/c$, $\theta = 90^\circ$.)</i>	144
4.7	<i>Two dimensional plot of δ vs absorbed transition radiation photons energy ($\theta = 30^\circ$) for electron momentum of $30 \text{ GeV}/c$.</i>	145
4.8	<i>The energy spectrum of the transition radiation photons absorbed in Si-pixel detector ($p = 30 \text{ GeV}/c$, $\theta = 30^\circ$.)</i>	146
4.9	<i>Distribution of the number of detected transition radiation photons ($p = 30 \text{ GeV}/c$, $\theta = 30^\circ$.)</i>	147
4.10	<i>Pion misidentification probability as a function of the momentum for electron efficiency = 90%: solid line - determined by charge sharing between Si-pixels; dashed line - determined by transition radiation radiation from pions(not dependent on η).</i>	150
5.1	<i>Implementation of simulation programme in GEANT</i>	166
5.2	<i>GEANT initialisation</i>	167
5.3	<i>GEANT event handling</i>	168
5.4	<i>GEANT GUTREV</i>	169
5.5	<i>GEANT GUTRAK</i>	170
5.6	<i>GEANT GTVOL</i>	171
5.7	<i>GEANT GUSTEP</i>	172
5.8	<i>Simulation programme TRDSIM.F</i>	173
5.9	<i>Simulation programme TRPHOT.F</i>	174
5.10	<i>Simulation programme TRSIDE.F</i>	175

Preface

Lepton identification is one of the most crucial aspects of high energy physics experiments and particle identification based on transition radiation can be used as an effective experimental method for electron identification in such experiments.

Transition radiation is the electromagnetic radiation that is emitted when a charged particle traverses the boundary between two media of differing dielectric properties. In more formal terms, transition radiation is the result of the reformation of the charge's associated field under conditions where either the medium through which the charged particle is propagating changes, or there occurs a change in the properties of that medium.

The existence of transition radiation was first suggested by Frank & Ginzburg (1945) where they argued that a uniformly moving charged particle must emit radiation when it crosses the boundary between two media. They derived its angular distribution for the case when the charged particle moves from vacuum into an ideal conductor. Their method was to consider the radiation as resulting essentially from the annihilation of the charge with its image induced by the charge in the conductor.

The calculation of transition radiation for the case of two dielectric media was first carried out by Beck (1948). His approach was to use the method of images for finding the field of the particle in the two media and then to introduce the transition radiation field in order to satisfy a boundary condition on the field

with time.

The same case was subsequently treated by Garibian (1958) in his search for wave solutions in the radiation zone. Garibian then went on to solve a boundary value problem with the fields expanded in plane incoming and outgoing waves.

Other aspects of transition radiation have also been considered in the literature. Pafomov (1958), Garibian & Chalikian (1959) considered the case of transition radiation in a slab. The case of emission from a stack of slabs was first addressed by Garibian (1959) and has been given exhaustive treatment by Artru, Yodh & Mennessier (1975). Transition radiation in wave guides was discussed by Barsukov (1960). X-ray production by transition radiation in a slab was treated theoretically by Garibian (1971). The relation between transition radiation and Cherenkov radiation has been investigated by Zrelov & Ruzicka (1978). Ramsey & Mackee (1978) have studied the contribution of transition radiation to X-ray production by protons. Recent work by Saveliev (2002) has led to the development of a theoretical description of transition radiation in the prewave zone, i.e. close to the trajectory of the incident charged particle.

The theoretical calculations of Garibian (1958) predicted that for highly relativistic particles most of the radiation is emitted in the X-ray region and that its intensity is dependent on the Lorentz factor γ of the incident charged particle. It is these characteristics which are particularly appealing to experimental high energy physics (HEP), especially for the purposes of particle identification.

Applications of transition radiation in HEP experiments require detailed simulation and analysis of transition radiation within the experimental environment. The main method of mathematical modelling used for such purposes is the Monte Carlo (MC) method.

Mathematical modelling is one of the most powerful tools available to HEP experiments, of which two main areas exist, event generation and full detector

simulation.

Event generation is performed by dedicated physics simulation programmes, known as physics generators, examples of these are the programmes Pythia and Fritioff, available as part of the LUND package (Sjostrand 1993).

Detector simulation and analysis is crucial during detector development and optimisation of detector parameters due to the prohibitive cost and limited availability of experimental test beam access. It also plays a vital role in the development of reconstruction algorithms that are needed for analysis of experimental data.

Due to the scale and complexity of HEP experiments, simulation studies have become essential to design and optimise the detectors, develop and test the reconstruction, and analysis programmes and to interpret the experimental data. The general tool used for such purposes in the field of HEP is GEANT (Brun, Hagelberg, Hansroul & Lassalle 1978), a detector description and simulation tool, available in the CERN Programme Library.

Whilst Transition Radiation Detectors (TRD) are now commonly used in HEP, to date no simulation of transition radiation or transition radiation detectors has been included in the standard MC tools currently used in HEP.

The latest version of the CERN detector simulation software GEANT4 does include a parameterisation model of transition radiation which allows estimation of detector performance, but it is unable to perform the detailed simulation needed for an accurate study of transition radiation applications (Apostolakis, Giani, Maire, Bagulya & Grichine 2000).

This thesis sets out the analysis and mathematical modelling of transition radiation as a phenomena of classical electromagnetism, and the development of its practical application for use in high energy physics experiments.

Chapter One presents a review of the theory of transition radiation beginning

with a discussion of the original work by Frank and Ginzburg which introduced transition radiation as a phenomena of classical electrodynamics. Garibian's work on a wave approach to the theory of transition radiation is then presented, which laid the foundations for the modern study of transition radiation. This is necessary as there is still no complete theoretical description of transition radiation within the literature and standard texts on classical electrodynamics e.g. Jackson (1998).

Chapter Two presents the development of a detailed mathematical model of transition radiation for highly relativistic conditions, and a tool to simulate the generation of transition radiation applicable to experimental high energy physics. This is then developed for periodic structures of media with different dielectric properties, which introduces the processes of interference and the propagation of transition radiation through media. Following on from this the study is further developed to include the processes of detection used for transition radiation and the treatment of the main background processes. In addition alongside detailed results are presented which were obtained from the mathematical simulation which show the main characteristics of transition radiation and how these can be accurately modelled.

The implementation of the full simulation programme within the GEANT detector description and simulation tool is described and this demonstrates the application of the simulation programme within the wider context of high energy physics simulation. Finally a study to verify the simulation programme is presented based on experimental data obtained from test beam results of a prototype TRD.

Chapter Three presents the application of the simulation programme within a large scale HEP experiment, HERA-*B* "An Experiment to Study CP Violation in the *B* System using an Internal Target at the HERA Proton Ring" situated

at the Deutsch Elektronen Synchrotron (DESY), Hamburg. The implementation of the simulation programme into the software environment of HERA-B, ARTE, is shown together with the main results of a Monte Carlo study of particle identification within the HERA-*B* experiment using transition radiation, which was used to optimise the design of the HERA-*B* TRD.

Chapter Four presents the analysis of a transition radiation detector which uses a strong magnetic field to separate transition radiation from the incident charged particle (background signal). The new concept TRD is presented for use at the future linear collider TESLA “The Superconducting Electron-Positron Linear Collider with an Intergrated X-Ray Laser Laboratory” which will be used for a next generation HEP experiment. The detailed analysis of the performance of such a detector was performed via a Monte Carlo study. This was performed using the transition radiation simulation programme which was extended to simulate the new conditions and changes in technology proposed for detection. The results show that this new concept of TRD could make a significant contribution to particle identification in future HEP experiments.

Chapter 1

Transition Radiation - Theory and Analysis of Physical Models

In this chapter a number of increasingly sophisticated theoretical models are outlined. Each model predicts the emission of transition radiation when a charged particle traverses the boundary between two media of different dielectric properties and produces formula for the energy of the emitted transition radiation.

Beginning with the original work of Frank & Ginzburg (1945) which considered an electron incident on a ideal conductor the discussion goes on to describe the approach of Garibian (1958) which includes a charged particle traveling through media of different dielectric properties and magnetic permeability. This is concluded with the case of a charged particle moving from vacuum to a medium and then from a medium to vacuum which form the basis of the simulation used in the subsequent chapters.

1.1 Theory of Transition Radiation

As has already been stated the phenomena of transition radiation was first described by Frank & Ginzburg (1945), where they considered the case of an electron

normally incident on the boundary between a vacuum and a perfect conductor. This led them to derive a formula for the energy radiated in a unit solid angle, in the relativistic case

$$W(\omega, \theta) = \frac{e^2 v^2 \sin^2 \theta}{\pi^2 c^3 (1 - \beta \cos^2 \theta)^2}$$

where e is the charge of an electron, v is its velocity, θ is the angle of emission of the transition radiation, c is the velocity of light in vacuum, and $\beta = \frac{v}{c}$.

In summary.

Consider a non relativistic electron normally incident upon a boundary between a vacuum and an ideal conductor of dielectric constant ε_1 , as shown in Fig. 1.1,

- An electron moving uniformly in a homogeneous medium radiates, if its velocity exceeds the phase velocity of light in that medium, the phenomenon known as the Cherenkov Effect.
- In vacuum an electron may only radiate when its velocity is altered, the phenomenon known as Bremsstrahlung.
- The fundamental difference between radiation phenomena in vacuum and in a refracting medium is not only determined by the possibility of exceeding the velocity of light in such a medium.
- In a refracting medium the electromagnetic field associated with the electron depends both on its velocity and the optical properties of the medium.

For simplicity the field of the electron may be said to be equal to the field of the electron in vacuum and of its image induced in the conductor moving towards it.

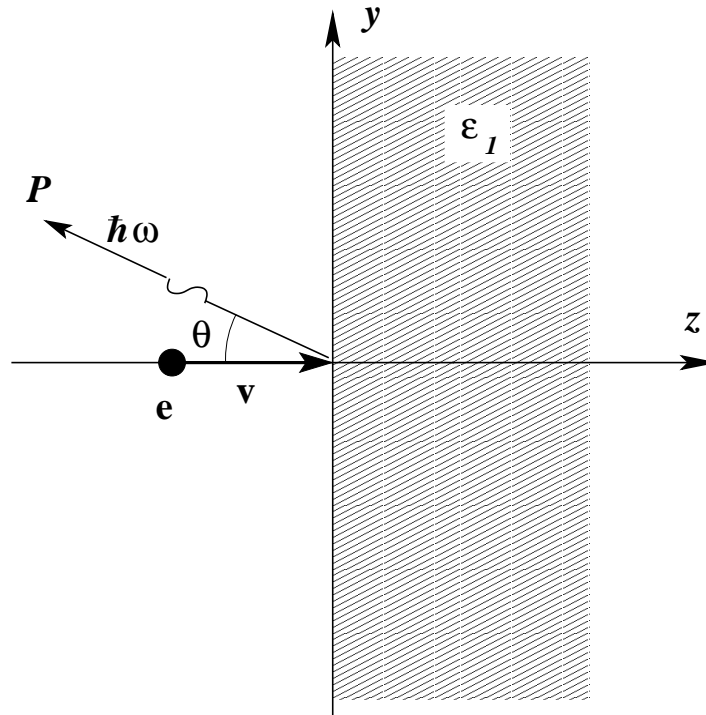


Fig. 1.1: A schematic illustration of transition radiation emission from a charge e moving with velocity v along the z axis, normally incident upon the boundary between vacuum and an ideal conductor of dielectric constant ϵ_1 , which lies along the y axis. P denotes the point of observation and θ the angle at which the transition radiation is emitted at a frequency of ω .

From the point of view of the field in the vacuum, the electron and its image cease to exist once the electron crosses the boundary. As a first approximation the crossing of the boundary by the electron may be seen to give rise to exactly the same radiation as that which would be due to the instantaneous stopping with infinite acceleration and annihilation at the boundary of the electron and its image.

In such a case this may be seen to be analogous to that of an electric dipole located at the boundary. The power radiated by an accelerated charge may be derived in terms of dipole radiation using Larmor's power formula (Jackson 1998)

$$P = \frac{q^2 a^2(t')}{6\pi c^3}$$

where q is charge, $a(t')$ acceleration, and the retarded time t' is given by

$$t' = t - \frac{r}{c}$$

where r is the radial distance from the charge and t is time, assuming that the electron is brought instantaneously to rest at the boundary, the acceleration may be said to be infinite. It is then possible to describe the acceleration as a Dirac delta function $\delta(t')$ of infinite magnitude acting over zero time. The integral of this gives the velocity of the electron, v as

$$v^2 = \int a(t')^2 \delta(t') dt$$

Due to the presence of both the electron and its image, the charge will be double, leading to a four fold increase in the energy radiated per unit solid angle, though in practice the total energy radiated proves to be only twice as large as the radiation takes place only in a single hemisphere. As a result the spectral density of the total radiation energy, i.e. the energy per unit interval of frequency ω is equal to

$$W(\omega) = \frac{4e^2 v^2}{3\pi c^3} \tag{1.1}$$

where q is replaced by e the charge of the electron.

A more complete description can only be achieved by considering not only the charge of the incident charged particle but also its associated field.

At this stage, so as to remain consistent with the work of Frank & Ginzburg (1945), only transition radiation in the backward direction, i.e. optical region, will be considered.

In such a case only radiation with wave length much larger than the dimensions of atoms and the distance between them is of interest. Therefore each of the media in which the electron is moving may be treated as homogeneous and specified by a complex dielectric constant $\varepsilon'_{1,2}$

$$\varepsilon'_{1,2} = \varepsilon_{1,2} - i \frac{4\pi\sigma_{1,2}}{\omega}$$

where the indices 1 and 2 refer, both here and in the following, to the first and second medium respectively, σ is the conductivity, and ω is the frequency of the radiation. The electron moves from the first medium into the second, the direction of velocity being normal to the plane boundary surface, as shown in Fig. 1.1.

The interesting region of the field lies within the wavezone, i.e. within one wavelength of the emitted transition radiation, observed from infinity, at not too small angles with respect to the boundary surface. Therefore the field in the first medium will be treated first.

This problem may be solved in a very elementary way using the reciprocity theorem, or in a more general and more rigorous way by reduction to the Sommerfeld (1909) problem of the field of a vertical dipole situated at a certain distance from a boundary surface between two media.

In both methods the field of the moving charge must be represented as the field of a system of fixed dipoles, in which case the field is described by Maxwell's equations, the current density $j(x, y, z, t)$ due to the moving charge being equal

to

$$j(x, y, z, t) = j_z = -ev\delta(z + vt)\delta(x)\delta(y) \quad (1.2)$$

where v is taken as the negative direction of the z axis, the Dirac delta functions assure that the moving charge only moves along the z axis and is located at $z = vt$. Fig. 1.1. All quantities, electric field strength $\mathbf{E}(\omega)$, current, etc. must be expanded into Fourier integrals

$$j = \int_{-\infty}^{+\infty} j(\omega)e^{i\omega t}d\omega; \mathbf{E} = \int_{-\infty}^{+\infty} \mathbf{E}(\omega)e^{i\omega t}d\omega \quad (1.3)$$

etc. As it is not possible to directly solve Maxwell's equations, the Hertz vector $\mathbf{\Pi}(\omega)$ is introduced with the help of the relations:

$$\left. \begin{aligned} \mathbf{E}(\omega) &= \frac{1}{\varepsilon'(\omega)}\nabla \cdot \mathbf{\Pi}(\omega) + k_0^2\mathbf{\Pi}(\omega) \\ \mathbf{H}(\omega) &= ik_0\nabla \times \mathbf{\Pi}(\omega) \\ k_0 &= \frac{\omega}{c} \end{aligned} \right\} \quad (1.4)$$

where k is the wave number, and $\mathbf{H}(\omega)$ the magnetic field strength.

Maxwell's equations are equivalent to the wave equation for $\mathbf{\Pi}(\omega)$:

$$\Delta\mathbf{\Pi}(\omega) + k_0^2\varepsilon'\mathbf{\Pi}(\omega) = -4\pi\mathbf{p}(\omega) \quad (1.5)$$

where ε' is the complex dielectric constant of the medium, while the polarisation vector $\mathbf{p}(\omega)$ is defined via $\mathbf{j}(\omega)$

$$\mathbf{p}(\omega) = \frac{\mathbf{j}(\omega)}{i\omega}$$

in the present case \mathbf{j} , \mathbf{p} and $\mathbf{\Pi}(\omega)$ are all directed along the z axis. Using equation (1.2) it is possible to obtain for \mathbf{p} ,

$$\begin{aligned} \mathbf{p}(\omega) &= -\frac{1}{2\pi i\omega} \int_{-\infty}^{+\infty} \mathbf{j}(\omega)e^{-i\omega t}dt \\ &= \frac{ie}{2\pi\omega} e^{i\frac{\omega}{v}z}\delta(x)\delta(y) \end{aligned} \quad (1.6)$$

A uniformly moving electron is thus equivalent to a line of dipoles distributed along the z axis with a moment per unit length of

$$\frac{ie}{2\pi\omega} e^{i\frac{\omega}{v}z}$$

this allows the field at a distant point to be represented as the result of the interference of plane waves from separate dipoles.

Considering now the field of an electron at the point of observation P, which having moved uniformly from infinity in the direction of the negative z axis is brought instantaneously to rest at the point $z = 0$. For simplicity it is assumed that all space is filled by the first medium and that consequently, no boundary surface exists.

Under such conditions the solution of equation (1.5) with the value of \mathbf{p} from (1.6) is given as follows

$$\mathbf{\Pi}(\omega) = \int_0^{+\infty} \mathbf{\Pi}_z(\omega) dz = \frac{ie}{2\pi\omega} \int_0^{+\infty} \frac{e^{i(\omega\frac{z}{v} - k_1 R)}}{R} dz \quad (1.7)$$

In equation (1.7), $\mathbf{\Pi}_z(\omega)$ represents the field at the point of observation P due to the dipoles situated over the segment dz near the point z , $k_1 = \frac{\omega}{c}\sqrt{\epsilon'}$, and R is the distance from the dipole to the point of observation P. The integration is performed over the coordinates of all the dipoles.

Note that only the part of the field related to the sudden stopping of the electron is of interest. At the point where the radiation takes place, in the region of $z = 0$, for large R it is possible to use the approximation $k_1 R = k_1 R_0 - k_1 z \cos \theta$ in the exponential factor in the integral (1.7) and $R = R_0$ in the denominator, where R_0 is the distance from the point $z = 0$.

The integration of equation (1.6) for small values of z can therefore, be carried out; since the value of the integral (1.7) is determined by its lower limit i.e. close to the boundary, the value of the field within the wavezone is equal to

$$\mathbf{\Pi}(\omega) = -\frac{e}{2\pi\omega R_0} \frac{e^{-ik_1 R_0}}{\left(\frac{\omega}{v} + k_1 \cos \theta\right)} \quad (1.8)$$

The radiation field arising when an electron passes from one medium into another can be found in a similar way. In fact it can be represented as a sum of two fields, firstly that of an electron moving in the first medium and stopping at its boundary, and secondly of an electron moving in the second medium starting from the boundary surface. The fields of each of the dipoles which determine the resulting field at P can be found by making use of the reciprocity theorem.

The field ${}^P_z \mathbf{\Pi}$ observed at P created by a dipole situated at z in the medium 1 ($z < 0$) is found to be

$${}^P_z \mathbf{\Pi}(\omega) = \frac{ie}{2\pi\omega} \left\{ \frac{e^{i\omega(\frac{z}{v} - k_1 R_z)}}{R_z} - f \frac{e^{i\omega(\frac{z'}{v} - k_1 R_{z'})}}{R_{z'}} \right\} \quad (1.9)$$

where f is the Fresnel coefficient for the amplitude of the reflected wave with an electrical vector lying in the plane of incidence, while the quantities z' and $R_{z'}$ determining the phase and the amplitude of the reflected wave are equal to the coordinate of the image of the point z on the boundary surface (i.e. $z' = -z$) and to the distance from P to z' .

Hence in analogy with equation (1.8) it is found that the field of the electron stopped in the medium 1 at the boundary surface is equal to

$$\mathbf{\Pi}_1(\omega) = \int_0^\infty {}^P_z \mathbf{\Pi}(\omega) dz = -\frac{e}{2\pi\omega R_0} e^{-ik_1 R_0} \left\{ \frac{1}{\frac{\omega}{v} + k_1 \cos \theta} + f \frac{1}{\frac{\omega}{v} - k_1 \cos \theta} \right\} \quad (1.10)$$

If medium 2 is a perfect conductor then $\mathbf{\Pi}_1(\omega)$ gives the complete field corresponding to the transition of the charge e from the medium 1 into the medium 2, where f must be set to unity. As can be seen from equation (1.10) Hertz' vector is equal, in this case, to the sum of the fields of two charges, moving in opposite directions. For non-relativistic velocities this leads to a simple doubling of the field amplitude. If medium 2 is not a perfect conductor then the field of

the dipoles lying within it must be taken into account. This field is equal to

$$\mathbf{\Pi}_2(\omega) = \frac{e}{2\pi\omega R_0} e^{-ik_1 R_0} (1+f) \frac{\varepsilon'_1}{\varepsilon'_2} \frac{1}{\left(\frac{\omega}{v} - \sqrt{k_2^2 - k_1^2 \sin^2 \theta}\right)}$$

The total field $\mathbf{\Pi}(\omega)$ equal to the sum of $\mathbf{\Pi}_1(\omega)$ and $\mathbf{\Pi}_2(\omega)$ is given by

$$\begin{aligned} \mathbf{\Pi}(\omega) = & \frac{e}{2\pi\omega R_0} e^{-ik_1 R_0} \left\{ \frac{2k_1 \cos \theta}{\frac{\omega^2}{v^2} - k_1^2 \cos^2 \theta} \right. \\ & \left. + (1+f) \left(\frac{k_1^2/k_2^2}{\frac{\omega}{v} - \sqrt{k_2^2 - k_1^2 \sin^2 \theta}} - \frac{1}{\frac{\omega}{v} - k_1 \cos \theta} \right) \right\} \end{aligned} \quad (1.11)$$

where $(\varepsilon'_1/\varepsilon'_2 = k_1^2/k_2^2)$.

It is now possible to present a more rigorous solution of the problem of the radiation emitted by electron, due to its passage from one medium into another. The equations for $\mathbf{\Pi}(\omega)$ when the half space $z > 0$ is filled by the medium 1 and the half space $z < 0$ by the medium 2, is as follows

$$\begin{aligned} z > 0 : \Delta \mathbf{\Pi}_1(\omega) + k_1^2 \mathbf{\Pi}_1(\omega) &= -4\pi \mathbf{p}(\omega) \\ z < 0 : \Delta \mathbf{\Pi}_2(\omega) + k_2^2 \mathbf{\Pi}_2(\omega) &= -4\pi \mathbf{p}(\omega) \end{aligned}$$

On the boundary surface $z = 0$ the tangential components of \mathbf{E} and \mathbf{H} must be continuous. In the case of a dipole this leads to the following conditions for $\mathbf{\Pi}(\omega)$:

$$\begin{aligned} \mathbf{\Pi}_1(\omega) &= \mathbf{\Pi}_2(\omega) \\ \frac{1}{k_1^2} \frac{\partial \mathbf{\Pi}_1(\omega)}{\partial z} &= \frac{1}{k_2^2} \frac{\partial \mathbf{\Pi}_2(\omega)}{\partial z} \end{aligned} \quad (1.12)$$

If a dipole exists at a single point only, i.e. for a certain value $z = z'$, a more general case must be considered since Sommerfeld's problem is often supposed to refer to the case of a dipole lying on the boundary surface, i.e. $z = 0$. The generalisation for the case of an arbitrary distance z' is obtained using the formula

$$\begin{aligned}
\frac{e^{-ik_1 R_1}}{R_1} &= \int_0^\infty \frac{\lambda J(\lambda r) e^{-\sqrt{\lambda^2 - k_1^2}(z-z')}}{\sqrt{\lambda^2 - k_1^2}} d\lambda; z > z' \\
\frac{e^{-ik_1 R_1}}{R_1} &= \int_0^\infty \frac{\lambda J(\lambda r) e^{+\sqrt{\lambda^2 - k_1^2}(z-z')}}{\sqrt{\lambda^2 - k_1^2}} d\lambda; z < z'
\end{aligned} \tag{1.13}$$

where $R_1 = \sqrt{r^2 + (z - z')^2}$, $r^2 = x^2 + y^2$, $\lambda^2 = \frac{\omega^2}{c^2}\varepsilon - \frac{\omega^2}{v^2}$ and J are Bessel functions of zero order.

If the dipole with a moment equal to unity is situated in the medium 1, i.e. $z' > 0$, at a distance z' , then it can be shown that

$$\left. \begin{aligned}
\Pi_1(\omega) &= \frac{2k_2^2}{k_1^2 + k_2^2} \frac{e^{-ik_1 R_1}}{R_1} + \frac{k_1^2 - k_2^2}{k_1^2 + k_2^2} \left(\frac{e^{-ik_1 R_1}}{R_1} - \frac{e^{-ik_1 R_2}}{R_2} \right) \\
&\quad + \int_0^\infty f_1(\lambda) J(\lambda r) e^{-\sqrt{\lambda^2 - k_1^2} z} d\lambda \\
f_1(\lambda) &= \frac{2k_1^2 k_2^2 \lambda \left(\sqrt{\lambda^2 - k_1^2} - \sqrt{\lambda^2 - k_2^2} \right)}{(k_1^2 + k_2^2) N \sqrt{\lambda^2 - k_1^2}} e^{-\sqrt{\lambda^2 - k_1^2} z'} \\
\Pi_2(\omega) &= \frac{2k_2^2}{k_1^2 + k_2^2} \frac{e^{-ik_1 R_1}}{R_1} + \int_0^\infty f_2(\lambda) J(\lambda r) e^{-\sqrt{\lambda^2 - k_2^2} z} d\lambda \\
f_2(\lambda) &= \frac{2k_2^4 \lambda \left(\sqrt{\lambda^2 - k_1^2} - \sqrt{\lambda^2 - k_2^2} \right)}{(k_1^2 + k_2^2) N \sqrt{\lambda^2 - k_2^2}} e^{-\sqrt{\lambda^2 - k_1^2} z'} \\
&\quad + \frac{2k_2^2 \lambda}{(k_1^2 + k_2^2) \sqrt{\lambda^2 - k_2^2}} \left(e^{-\sqrt{\lambda^2 - k_1^2} z'} - e^{-\sqrt{\lambda^2 - k_2^2} z'} \right)
\end{aligned} \right\} \tag{1.14}$$

where

$$R_1 = \sqrt{r^2 + (z - z')^2}, \quad R_2 = \sqrt{r^2 + (z + z')^2}, \quad N = k_1^2 \sqrt{\lambda^2 - k_2^2} + k_2^2 \sqrt{\lambda^2 - k_1^2}$$

For $k_1 = k_2$, $f_1 = f_2 = 0$ and $\Pi_1(\omega) = \Pi_2(\omega) = e^{-ik_1 R_1}/R_1$, the field of a dipole in a homogeneous space is obtained. For $z' = 0$ Sommerfeld's solution is obtained. Finally for $k_2 \rightarrow \infty$, i.e. medium 2 is a perfect conductor, $f_1 = 0$, $\Pi_1(\omega) = \frac{e^{-ik_1 R_1}}{R_1} + \frac{e^{-ik_1 R_2}}{R_2}$ and $\Pi_2(\omega) = 0$ as expected.

If the dipole is situated in medium 2 at a distance z' from the boundary then the field in medium 1, i.e. $\mathbf{\Pi}_1(\omega)(z' < 0)$, which is of interest, is equal to the expression for $\mathbf{\Pi}_2(\omega)$ in (1.14) with z replaced by $-z$, z' by $-z'$ and k_1 by k_2 . To find the field of the electron in medium 1 it is necessary to integrate the field $\mathbf{\Pi}_1(\omega)(z')$, multiplied by $\frac{ie}{2\pi\omega}e^{i\frac{\omega}{v}z'}$, with respect to dz from $-\infty$ to $+\infty$. Making use of (1.13) and (1.14), this can be done (for $z > 0$) with the following expression obtained as a result

$$\begin{aligned} \mathbf{\Pi}(\omega, z, r) = & \frac{ie}{\pi\omega} \left\{ \int_0^\infty \frac{\lambda J(\lambda r) e^{i\frac{\omega}{v}z}}{\lambda^2 - k_1^2 + \frac{\omega^2}{v^2}} d\lambda - \int_0^\infty \frac{\lambda J(\lambda r) e^{-\sqrt{\lambda^2 - k_1^2}z}}{\lambda^2 - k_1^2 + \frac{\omega^2}{v^2}} d\lambda \right. \\ & + \int_0^\infty \frac{k_2^2}{N} \left(\frac{\frac{k_1^2}{k_2^2}}{\sqrt{\lambda^2 - k_2^2} + i\frac{\omega}{v}} + \frac{1}{\sqrt{\lambda^2 - k_1^2} - i\frac{\omega}{v}} \right) \times \\ & \left. \times J(\lambda r) e^{-\sqrt{\lambda^2 - k_1^2}z} \lambda d\lambda \right\} \end{aligned} \quad (1.15)$$

The first of these integrals describes the field of a uniformly moving electron in the absence of a boundary surface when $k_1 = k_2$, in such a case only this term remains. From here on this term will be left aside and $\mathbf{\Pi}(\omega)$ will denote only the difference between $\mathbf{\Pi}(\omega)$ and the first term in equation (1.15).

For $k_2 \rightarrow \infty$, i.e. for a perfect conductor, it can be seen that

$$\mathbf{\Pi}(\omega) = \frac{e}{\pi v} \int_0^\infty \frac{\lambda J(\lambda r) e^{-\sqrt{\lambda^2 - k_1^2}z}}{\sqrt{\lambda^2 - k_1^2}(\lambda^2 - k_1^2 + \frac{\omega^2}{v^2})} d\lambda \quad (1.16)$$

This expression can be obtained directly by taking into account that in this case $\mathbf{\Pi}_1(\omega) = \frac{e^{-ik_1 R_1}}{R_1} + \frac{e^{-ik_1 R_2}}{R_2}$ and $\mathbf{\Pi}_2(\omega) = 0$.

In this case equation (1.16) describes the field due to the instantaneous stopping of the electron and its image. In the non-relativistic approximation, when

$$|k_1^2| = |\varepsilon_1'| \frac{\omega^2}{c^2} \ll \frac{\omega^2}{v^2} \quad (1.17)$$

expression (1.16) reduces, to the following (see (1.13))

$$\mathbf{\Pi}(\omega) = -\frac{ev}{\pi\omega^2} \frac{e^{-ik_1 R_0}}{R_0}, \quad R = \sqrt{r^2 + z^2}$$

i.e. the radiation is the same as that due to a vertical dipole with the moment $\frac{ev}{\pi\omega^2}$ situated at the point $x = y = z = 0$. Under the condition (1.17) for an arbitrary k_2 , it is found that:

$$\mathbf{\Pi}(\omega) = -\frac{ev}{2\pi\omega^2} \frac{k_2^2 - k_1^2}{k_2^2} \int_0^\infty \frac{2k_2^2}{N} J(\lambda r) e^{-\sqrt{\lambda^2 - k_1^2} z} d\lambda \quad (1.18)$$

The integral in equation (1.18) represents the Sommerfeld expression for the field of a single dipole situated in medium 1 on its boundary surface with medium 2. The magnitude of the dipole which is equivalent with respect to the radiation of frequency ω to the electron crossing the boundary, is equal to $-\frac{ev}{2\pi} \frac{k_2^2 - k_1^2}{k_2^2}$. As has already been mentioned for $k_2 \rightarrow \infty$, the integral in equation (1.18) is equal to $2e^{-ik_1 R_0}/R_0$.

In order to obtain equation (1.18) from equation (1.15) under the condition (1.17), it is necessary to take into account that if

$$|k_2^2| = |\varepsilon_2'| \frac{\omega^2}{c^2} \ll \frac{\omega^2}{v^2}$$

then equation (1.18) follows immediately; if, however the term $\sqrt{\lambda^2 - k_1^2}$ cannot be neglected as compared with $\frac{\omega}{v}$ in view of the significance of $|\varepsilon_2'|$ then by virtue of condition (1.17), simultaneously $|k_2^2| \gg |k_1^2|$ and as can be seen from equation (1.15), this expression can again be reduced to the form of equation (1.18) with $(k_2^2 - k_1^2)/k_2^2$ replaced by unity.

The equations (1.16) and (1.18) determine the field in the whole half space $z > 0$. For practical purposes it is interesting to investigate the properties of the field at points which are very distant (in comparison with the wave length) from the point $x = y = z = 0$ and for not too large angles θ see Fig. 1.1. It is therefore possible to obtain in this case a relatively simple expression for $\mathbf{\Pi}(\omega)$ and hence for $\mathbf{E}(\omega), \mathbf{H}(\omega)$ and for the radiated energy $W(\omega)$.

Here it is possible to use the well known formula

$$\frac{e^{-ik_1 R_0}}{R_0} = -\frac{ik_1}{2\pi} \int_0^{2\pi} d\phi \int_0^{\pi/2 - i\infty} e^{ik_1(x \sin \theta \cos \phi + y \sin \theta \sin \phi + z \cos \theta)} \sin \theta d\theta \quad (1.19)$$

where ϕ is the azimuth and θ the angle between R_0 and the z axis. It must be taken into account that in the case of a transition from expressions of the type (1.13) and (1.19) it must be considered that

$$\sqrt{\lambda^2 - k_1^2} = ik_1 \cos \theta \quad (1.20)$$

Using equations (1.13), (1.19) and (1.20), and leaving aside the first term, equation (1.15) may be reduced to the form

$$\left. \begin{aligned} \mathbf{\Pi}(\omega) &= \frac{ek_1}{4\pi^2\omega} \int_0^{2\pi} \int_0^{\pi/2-i\infty} A e^{ik_1(x \sin \theta \cos \phi + y \sin \theta \sin \phi + z \cos \theta)} \sin \theta d\theta d\phi \\ A &= -\frac{2ik_1 \cos \theta}{\frac{\omega^2}{v^2} - k_1^2 \cos^2 \theta} - i(1+f) \times \\ &\quad \times \left(\frac{k_1^2}{k_2^2 \left(\frac{\omega}{v} + \sqrt{k_2^2 - k_1^2 \sin^2 \theta} \right)} - \frac{1}{\frac{\omega}{v} - k_1 \cos \theta} \right) \end{aligned} \right\} \quad (1.21)$$

where the Fresnel coefficient f , as in equation (1.9), has the value

$$1 + f = \frac{2k_2^2 \cos \theta}{k_2^2 \cos \theta + k_1 \sqrt{k_2^2 - k_1^2 \sin^2 \theta}} \quad (1.22)$$

In deriving expression (1.21) it must be taken into account that $1 + f = -2ik_1 k_2^2 \cos \theta / N$. In the non-relativistic approximation (1.17) is equal to,

$$A = \frac{iv}{\omega} \frac{k_2^2 - k_1^2}{k_2^2} (1 + f) \quad (1.23)$$

If the observation is carried out in the wave zone for not too large angles θ then expression (1.21), for the purposes of determining $\mathbf{E}(\omega)$ and $\mathbf{H}(\omega)$, is equivalent to Hertz's vector $\mathbf{\Pi}'(\omega)$ for a dipole with an angular factor $A(\theta, \omega)$

$$\mathbf{\Pi}'(\omega) = \frac{ie}{2\pi\omega} A(\theta, \omega) \frac{e^{-ik_1 R_0}}{R_0} \quad (1.24)$$

This expression coincides with equation (1.11). When determining $\mathbf{E}(\omega)$ and $\mathbf{H}(\omega)$ the angle θ must be regarded as constant. As a result, making use of

expression (1.4), and considering only terms decreasing as $1/R_0$ gives (on the assumption that $\varepsilon'_1 = \varepsilon_1$, i.e. that in medium 1 no absorption takes place)

$$\left. \begin{aligned} E_{\omega,\theta} &= \frac{\omega^2}{c^2} \mathbf{\Pi}'(\omega) \sin \theta \\ H_{\omega,\phi} &= -\sqrt{\varepsilon} \frac{\omega^2}{c^2} \mathbf{\Pi}'(\omega) \sin \theta \\ k_1 &= \sqrt{\varepsilon_1} \frac{\omega}{c} \end{aligned} \right\} \quad (1.25)$$

The Poynting vector $S = \frac{c}{4\pi} [\mathbf{E}\mathbf{H}]$ in the wave zone is directed along R and is equal to $S_R = -\frac{c}{4\pi} E_\theta H_\phi$. The energy flow radiated by the electron within the solid angle $d\Omega = \sin \theta d\theta d\phi$ is equal to

$$\int_0^\infty W(\omega, \theta) d\Omega d\omega = R_0^2 \sin \theta d\theta d\phi \int_{-\infty}^{+\infty} S_R dt \quad (1.26)$$

Substituting into equation (1.26) from the values of (1.24), (1.25), and taking into account equation (1.3) and making use of

$$\int_{-\infty}^{+\infty} e^{i(\omega+\omega')t} dt = 2\pi \delta(\omega + \omega')$$

the following expression for $W(\omega, \theta)$ is obtained

$$W(\omega, \theta) = \frac{e^2 \sqrt{\varepsilon_1} \omega^2 |A(\theta, \omega)|^2 \sin^2 \theta}{4\pi^2 c^3} \quad (1.27)$$

Using the non-relativistic approximation (1.23)

$$W(\omega, \theta) = \frac{e^2 v^2}{4\pi^2 c^3} \left| \frac{\varepsilon'_2 - 1}{\varepsilon'_2} \right|^2 |1 + f|^2 \sin^2 \theta \quad (1.28)$$

where, for the present case, $\varepsilon_1 = 1$ has been set i.e. the first medium is treated as a vacuum. For a perfect conductor ($\varepsilon'_2 \rightarrow \infty$) $f = 1$ and

$$W(\omega, \theta) = \frac{e^2 v^2 \sin^2 \theta}{\pi^2 c^3}$$

the total energy radiated per unit frequency is

$$\int_0^2 \pi d\phi \int_0^{\pi/2} W(\omega, \theta) \sin \theta d\theta = \frac{4e^2 v^2}{3\pi c^3} \quad (1.29)$$

which is equal to the original expression (1.1).

For a relativistic electron in the same case of transition from a vacuum into a perfect conductor $\mathbf{\Pi}(\omega)$ is determined by equations (1.10) via the substitution of $\varepsilon_1 = 1$ and $f = 1$, or by equations (1.21) and (1.22) under the same conditions and with $\varepsilon_2 = \infty$). This gives

$$A = -\frac{2iv}{\omega(1 - \beta^2 \cos^2 \theta)}$$

where $\beta = \frac{v}{c}$.

Substituting this value of A into (1.27) with $\varepsilon_1 = 1$, it is found that the energy radiated per unit solid angle is

$$W(\omega, \theta) = \frac{e^2 v^2}{\pi^2 c^3} \frac{\sin^2 \theta}{(1 - \beta^2 \cos^2 \theta)^2}$$

Hence the total energy radiated per unit frequency is equal to

$$W(\omega) = \frac{4e^2 v^2}{3\pi c^3} \left\{ \frac{3}{8} \frac{\beta^2 + 1}{\beta^2} \ln \frac{1 + \beta}{1 - \beta} - \frac{3}{4\beta^2} \right\} \quad (1.30)$$

where $\beta = \frac{v}{c}$.

For β lying close to unity the quantity in the curly braces $\{\}$ fully determines the dependence of the energy radiated upon the energy of the electron.

Taking equation (1.28) for the non-relativistic case and replacing the term $1 + f$ with expression (1.22) and substituting the values of k_1 and k_2 with the values $k_1 = \omega/c$ and $k_2 = \varepsilon\omega^2/c^2$, i.e. for vacuum and a dielectric of permittivity ε' , gives

$$W(\omega, \theta) = \frac{e^2 v^2}{\pi^2 c^3} \left| \frac{\varepsilon' - 1}{\varepsilon' \cos \theta + \sqrt{\varepsilon' - \sin^2 \theta}} \right|^2 \sin^2 \theta \cos^2 \theta \quad (1.31)$$

Here $W(\omega, \theta)$ is the energy radiated at an angle θ per unit solid angle, per unit frequency range by a uniformly moving electron (with $\beta \ll 1$), passing from vacuum into a medium with a complex dielectric constant ε' . Whilst in (1.31) there appears to be no dependence on ω it should be remembered that in this

case only the non-relativistic approximation has been considered and this for frequencies within the optical range where $\varepsilon' = \varepsilon'_2(\omega)$ may be considered to be constant.

1.2 Wave Theory of Transition Radiation

1.2.1 General Case

Garibian's considerations are now presented for the radiation fields produced in the general case where the two media differ in both their dielectric and magnetic properties (Garibian 1958).

The field associated with a particle is considered for a particle which has velocity v and moves from one medium into another with different dielectric properties, as shown in Fig. 1.2. As above the first medium is characterised by the macroscopic constants ε_1 and μ_1 , the dielectric constant and magnetic permeability respectively. The second medium is characterised by the ε_2 and μ_2 . Through out this analysis the energy lost by the particle per unit path length may be considered as negligibly small compared with its kinetic energy. Under these conditions the field associated with the particle is given by Maxwell's equations

$$\begin{aligned}\nabla \times \mathbf{E} &= -\frac{1}{c} \frac{\partial \mathbf{B}}{\partial t} \\ \nabla \times \mathbf{H} &= \frac{1}{c} \frac{\partial \mathbf{D}}{\partial t} + \frac{4\pi}{c} \mathbf{v} e \delta(\mathbf{r} - \mathbf{v}t) \\ \nabla \cdot \mathbf{D} &= 4\pi e \delta(\mathbf{r} - \mathbf{v}t) \\ \nabla \cdot \mathbf{B} &= 0\end{aligned}$$

Here it will be assumed that the particle moves along the z -axis from $-\infty$ to $+\infty$ and that the interface between the two media is the plane $z = 0$ through which the particle moves at $t = 0$. The field and current are resolved in triple

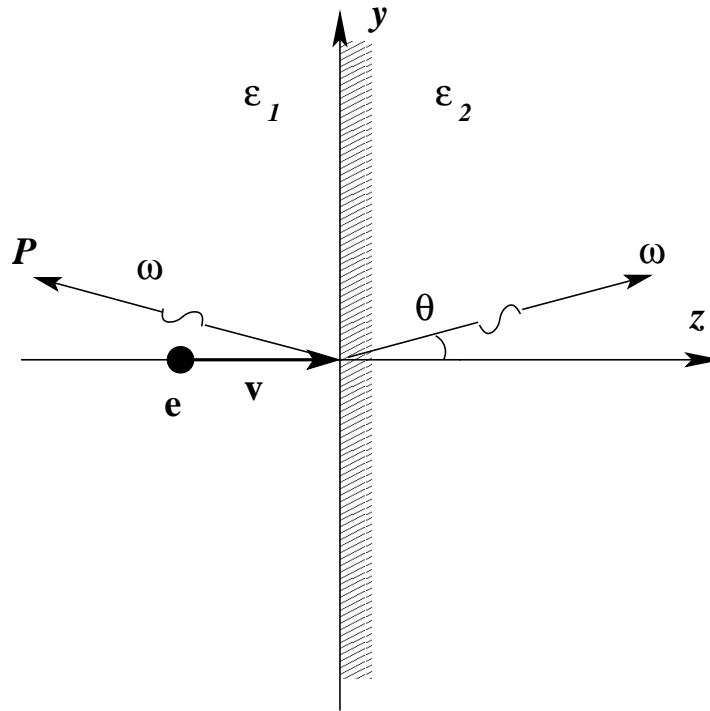


Fig. 1.2: A schematic illustration of transition radiation emission from a charge e moving with velocity v along the z axis, normally incident upon the boundary between media with dielectric constants ϵ_1 and ϵ_2 , which lies along the y axis. P denotes the point of observation and θ the angle at which the transition radiation is emitted at a frequency of ω .

Fourier integrals

$$\mathbf{E}(\mathbf{r}, \mathbf{t}) = \int \mathbf{E}(\mathbf{k}) e^{i(\mathbf{k}\mathbf{r} - \omega\mathbf{t})} d\mathbf{k} \quad \text{etc.} \quad (1.32)$$

where

$$\omega = \mathbf{k}\mathbf{v} = k_z v, \quad \mathbf{D}_{1,2}(\mathbf{k}) = \varepsilon_{1,2}(\omega) \mathbf{E}_{1,2}(\mathbf{k}), \quad \mathbf{B}_{1,2}(\mathbf{k}) = \mu_{1,2}(\omega) \mathbf{H}_{1,2}(\mathbf{k})$$

as above quantities which refer to both media will be denoted by the subscripts [1,2].

The Fourier components of the field have the following form (Garibian 1958)

$$\begin{aligned} \mathbf{E}(\mathbf{k}) &= \frac{ei}{2\pi^2} \frac{1}{\varepsilon_{1,2}} \frac{\frac{\omega}{c^2} \chi_{1,2} \mathbf{v} - \mathbf{k}}{k^2 - \frac{\omega}{c^2} \chi_{1,2}} \\ \mathbf{H}(\mathbf{k}) &= \frac{\varepsilon_{1,2}}{c} [\mathbf{v} \times \mathbf{E}_{1,2}(\mathbf{k})] \end{aligned} \quad (1.33)$$

where $\chi_{1,2} = \varepsilon_{1,2} \mu_{1,2}$.

The fields in (1.32) with Fourier components (1.33) do not satisfy the continuity conditions on the tangential components of \mathbf{E} and \mathbf{H} and on the normal components of \mathbf{D} and \mathbf{B} at $z = 0$. In order to satisfy these requirements it is necessary to add to the solution of the inhomogeneous Maxwell's equations given above the solutions of the homogeneous equations with arbitrary Fourier components and then determine these from the continuity requirements on the fields at the interface between the two media. In the following the symbols ρ and κ will be used to denote the components of the vectors \mathbf{r} and \mathbf{k} which lie in the xy -plane. The solutions of the homogeneous Maxwell equations are written in the form

$$\mathbf{E}'_{1,2}(r, t) = \int \mathbf{E}'_{1,2}(k) e^{i(\kappa\rho + \lambda_{1,2}z - \omega t)} d\mathbf{k} \quad (1.34)$$

and similarly for $\mathbf{H}'_{1,2}(r, t)$. In order for the expression given in (1.34) to be a solution of the homogeneous Maxwell equations, it is required that

$$\lambda_{1,2}^2 = \frac{\omega^2}{c^2} \chi_{1,2} - \kappa^2$$

The symbol λ' is used to denote the real part of λ and λ'' to denote the imaginary part of λ . The first medium is located in the region $z < 0$. Hence, to prevent the field given in (1.34) from diverging at $z \rightarrow -\infty$ it is required that $\lambda_1'' < 0$. It is also obvious that the radiation field in the first medium can propagate only in the negative z -direction (reflected waves) from which it follows that $\lambda_1' < 0$. From similar consideration it is found that $\lambda_2' > 0$ and $\lambda_2'' > 0$. The sign for λ_1' and λ_2' which have been indicated refer to positive ω . For negative values of ω these signs must be reversed.

It also follows from the equations for the radiation fields that

$$\mathbf{H}'_{1,2}(\mathbf{k}) = \frac{c}{\omega\mu_{1,2}}(\kappa + \mathbf{n}\lambda_{1,2})E'_{1,2}(\mathbf{k}),$$

$$(\kappa + \mathbf{n}\lambda_{1,2}) \times \mathbf{E}'_{1,2}(\mathbf{k}) = 0$$

the unit vector \mathbf{n} is taken in the direction of the positive z -axis. The last condition can be written in another form, resolving $\mathbf{E}'_{1,2}(\mathbf{k})$ into tangential and normal components:

$$\kappa\mathbf{E}'_{1,2t}(\mathbf{k}) + \lambda_{1,2}E'_{1,2n}(\mathbf{k}) = 0$$

Equating the field components at $z = 0$, gives four conditions for determining the Fourier components of the radiation field. It can be shown from these conditions that the $\mathbf{E}'_{1,2t}$ vectors are in the same direction as the vector κ . Assuming this to be the case, it turns out that only two of the four conditions are independent; from which the following two are taken

$$-\frac{ei}{2\pi^2} \frac{1}{\varepsilon_1} \frac{\kappa}{k^2 - \frac{\omega^2}{c^2}\chi_1} + E'_{1t}(\mathbf{k}) = -\frac{ei}{2\pi^2} \frac{\kappa}{k^2 - \frac{\omega^2}{c^2}\chi_2} + E'_{2t}(\mathbf{k}),$$

$$\frac{ei}{2\pi^2} \frac{\frac{\omega^2}{c^2}\chi_1 v - k_z}{k^2 - \frac{\omega^2}{c^2}\chi_1} + \varepsilon_1 E'_{1n}(\mathbf{k}) = \frac{ei}{2\pi^2} \frac{\frac{\omega^2}{c^2}\chi_2 v - k_z}{k^2 - \frac{\omega^2}{c^2}\chi_2} + \varepsilon_2 E'_{2n}(\mathbf{k})$$
(1.35)

From (1.35) it is possible to obtain the following expressions for the Fourier

components of the radiation fields:

$$\left. \begin{aligned} \mathbf{E}'_{1t}(\mathbf{k}) &= \frac{ei}{2\pi^2} \frac{\kappa\lambda_1}{\zeta} \eta \\ E'_{1n} &= -\frac{ei}{2\pi^2} \frac{\kappa^2}{\zeta} \eta \\ \mathbf{H}'_1(\mathbf{k}) &= \frac{ei}{2\pi^2 c} \frac{k_z \varepsilon_1 [\kappa \mathbf{v}]}{\zeta} \eta \end{aligned} \right\} \quad (1.36)$$

The following notation has been introduced

$$\eta = \frac{\frac{\varepsilon_2}{\varepsilon_1} - \frac{v}{\omega} \lambda_2}{k^2 - \frac{\omega^2}{c^2} \chi_1} + \frac{-1 + \frac{v}{\omega} \lambda_2}{k^2 - \frac{\omega^2}{c^2} \chi_2}, \quad \zeta = \varepsilon_2 \lambda_1 - \varepsilon_1 \lambda_2 \quad (1.37)$$

The radiation fields in the second medium can be obtained from (1.36) and (1.37) if the subscripts 1 and 2 are interchanged. If in (1.36) it is taken that $\mu_1 = \mu_2$ and $\varepsilon_1 = \varepsilon_2$, all the Fourier components of the radiation field vanish as is to be expected

1.2.2 Vacuum to Medium Case

A case of practical interest is now considered, i.e. the case in which the particle moves from vacuum into a medium. Under which conditions $\varepsilon_1 = \mu_1 = 1$, $\mu_2 = 1$ and $\varepsilon_2 = \varepsilon = \varepsilon' + \varepsilon''$. The field of interest will be that produced in the vacuum, i.e. the radiation field E'_1 and H'_1 .

The vacuum fields are obtained from (1.36) and (1.37), the expression for E'_1 is

$$E'_{1\rho} = \frac{ei}{2\pi^2} \int \frac{\kappa\lambda_1 \cos \Phi}{\varepsilon\lambda_1 - \lambda_2} \eta_1 e^{i(\kappa\rho \cos \Phi + \lambda_1 z - \omega t)} \kappa d\kappa d\Phi \frac{d\omega}{v}$$

where Φ is the angle between κ and ρ , while

$$\begin{aligned} \eta_1 &= \frac{\varepsilon - \frac{v}{\omega} \lambda_2}{\kappa^2 + \frac{\omega^2}{v^2} - \frac{\omega^2}{c^2}} + \frac{-1 + \frac{v}{\omega} \lambda_2}{\kappa^2 + \frac{\omega^2}{v^2} - \frac{\omega^2}{c^2} \varepsilon} \\ \lambda_1^2 &= \left(\frac{\omega}{c}\right)^2 - \kappa^2 \\ \lambda_2^2 &= \left(\frac{\omega}{c}\right)^2 \varepsilon - \kappa^2 \end{aligned}$$

The integration over Φ extends from 0 to 2π , that over κ from 0 to ∞ , and that over ω from $-\infty$ to $+\infty$. The integral over ϕ may be computed in terms of Bessel functions.

At this point R is introduced which signifies the distance from the point at which the particle enters the medium to the field point being investigated, and the angle θ defined by the expression $\rho = R \sin \theta$ and $z = -R \cos \theta$; it is assumed that R is large. If very small values of θ are not considered the asymptotic expressions for the Bessel functions can be used.

$$J_p(\kappa R \sin \theta) = \sqrt{\frac{2}{\pi \kappa R \sin \theta}} \cos \left(\kappa R \sin \theta - \frac{p\pi}{2} - \frac{\pi}{4} \right)$$

Thus giving

$$E'_{1\rho} = -\frac{e}{\pi v \sqrt{2\pi R \sin \theta}} \int \frac{\kappa \lambda_1}{\varepsilon \lambda_1 - \lambda_2} \eta_1 \left(e^{f(\kappa)R - \frac{3}{4}\pi i} + e^{\phi(\kappa)R + \frac{3}{4}\pi i} \right) e^{-i\omega t} \sqrt{\kappa} d\kappa d\omega$$

$$f(\kappa) = i\kappa \sin \theta - i\lambda_1 \cos \theta$$

$$\phi(\kappa) = -i\kappa \sin \theta - i\lambda_1 \cos \theta$$

For very large values of R , an integral of this type may be computed by the method of steepest descent. As a result it is found that

$$E'_{1\rho} = \frac{e\beta^2}{\pi v R} \int_{-\infty}^{+\infty} \sin \theta \cos^2 \theta \xi e^{i\omega[\frac{R}{c}-t]} d\omega$$

where

$$\xi = \frac{\frac{\varepsilon - \beta \sqrt{\varepsilon - \sin^2 \theta}}{1 - \beta^2 \cos^2 \theta} - \frac{-1}{1 + \beta \sqrt{\varepsilon - \sin^2 \theta}}}{\varepsilon \cos \theta + \sqrt{\varepsilon - \sin^2 \theta}}$$

Similar calculations lead to the following expression for the normal component of the radiation field:

$$E'_{1n} = \frac{e\beta^2}{\pi v R} \int_{-\infty}^{+\infty} \sin^2 \theta \cos \theta \xi e^{i\omega[\frac{R}{c}-t]} d\omega$$

The electric vector of the radiation field E'_1 lies in the plane which passes through the line to the point of observation and the trajectory of the particle and is perpendicular to the line of observation, i.e. the direction of R. In such case

$$E'_1 = E'_{1\rho} \cos \theta + E'_{1n} \sin \theta = \frac{e\beta^2}{\pi v R} \int_{-\infty}^{+\infty} \sin \theta \cos \theta \xi e^{i\omega[\frac{R}{c}-t]} d\omega$$

Finally it is possible to obtain an expression for the magnetic field H'_1 which, as is to be expected, is the same as the expression for E'_1 . Thus, at large distances, a spherically diverging wave is described with a Poynting vector parallel to R. The Poynting vector flux in the solid angle $d\Omega = \sin \theta d\theta d\phi$ during the time of flight of the particle is

$$\frac{dW_{trans}}{d\Omega} = \frac{ce^2 \sin^2 \theta \cos^2 \theta}{\pi^2 v^2} \frac{\beta^4}{(1 - \beta^2 \cos^2 \theta)^2} \int_0^\infty \left[\frac{(\varepsilon - 1)(1 - \beta^2 + \beta \sqrt{\varepsilon - \sin^2 \theta})}{(\varepsilon \cos \theta + \sqrt{\varepsilon - \sin^2 \theta})(1 + \beta \sqrt{\varepsilon - \sin^2 \theta})} \right]^2 d\omega \quad (1.38)$$

Under the non-relativistic conditions, i.e. where $\beta \ll 1$ and ε is taken as constant, equation (1.38) reduces to the corresponding formula (1.31) given by Frank & Ginzburg (1945) which was obtained via a more approximate manner.

1.2.3 Medium to Vacuum Case

Considering now the case in which the particle moves from medium into vacuum i.e., $\varepsilon_2 = \mu_2 = 1$, $\mu_1 = 1$ and $\varepsilon_1 = \varepsilon' + i\varepsilon''$. In this case it is important to note that the radiation field in the vacuum will consist of both the field due to transition radiation as well as that due to Cherenkov radiation which is generated in the medium and then propagates into the vacuum. This condition means that for this case an expression for the transition radiation cannot simply be obtained by reversing the particle velocity. This is evident from the fact that the term $1 - \beta \sqrt{\varepsilon - \sin^2 \theta}$ is present in the denominator of equation (1.38), which vanishes at certain frequencies for transparent media.

Thus, as in the case for vacuum to media an expression for $E'_{2\rho}$ found, followed by the integration over angle Φ and values at large distances $R(\rho = R \sin \theta, z = R \cos \theta)$ are taken:

$$E'_{2\rho} = -\frac{e}{\pi v \sqrt{2\pi R \sin \theta}} \int \frac{\kappa \lambda_2}{\varepsilon \lambda_2 - \lambda_1} \eta_2 \left(e^{f_1(\kappa)R - \frac{3}{4}\pi i} + e^{\phi_1(\kappa)R + \frac{3}{4}\pi i} \right) e^{-i\omega t} \sqrt{\kappa} d\kappa d\omega$$

where

$$f_1(\kappa) = i\kappa \sin \theta + i\lambda_2 \cos \theta$$

$$\phi_1(\kappa) = -i\kappa \sin \theta + i\lambda_2 \cos \theta$$

and

$$\begin{aligned} \eta_2 &= \frac{1 - \frac{v}{\omega} \lambda_1}{\kappa^2 + \frac{\omega^2}{v^2} - \frac{\omega^2}{c^2} \varepsilon} + \frac{-\varepsilon + \frac{v}{\omega} \lambda_1}{\kappa^2 + \frac{\omega^2}{v^2} - \frac{\omega^2}{c^2}} \\ \lambda_1^2 &= \left(\frac{\omega^2 \varepsilon}{c^2} \right) - \kappa^2 \\ \lambda_2^2 &= \left(\frac{\omega^2}{c^2} \right) - \kappa^2 \end{aligned}$$

As in the previous case, for very large values of R , the integral is computed by the method of steepest decent, taking care to treat the contribution of Cherenkov radiation correctly. This gives the following result

$$\begin{aligned} E'_{2\rho} &= -\frac{e\beta^2}{\pi v R} \int_{-\infty}^{+\infty} \frac{\sin \theta \cos \theta}{\varepsilon \cos \theta + \sqrt{\varepsilon - \sin^2 \theta}} \\ &\times \left\{ \frac{\varepsilon + \beta \sqrt{\varepsilon - \sin^2 \theta}}{1 - \beta^2 \cos^2 \theta} - \frac{1}{1 - \beta \sqrt{\varepsilon - \sin^2 \theta}} \right\} e^{i\omega(R/c-t)} d\omega \\ &+ \frac{2e}{v \sqrt{2\pi R \sin \theta v}} \int_{-\infty}^{+\infty} \frac{\sqrt{1 + \beta^2(1 - \varepsilon')}}{1 + \varepsilon' \sqrt{1 + \beta^2(1 - \varepsilon')}} (\beta^2 \varepsilon' - 1)^{1/4} \\ &\times \sqrt{-i\omega} \exp \left\{ i \left(-\omega t + \frac{\omega}{v} \sqrt{\beta^2 \varepsilon' - 1} R \sin \theta \right. \right. \\ &\left. \left. + \frac{\omega}{v} \sqrt{1 + \beta^2(1 - \varepsilon')} R \cos \theta \right) \right\} \end{aligned} \quad (1.39)$$

The first term in this expression is associated with the production of transition

radiation since the second term appears only if the condition for Cherenkov radiation is satisfied i.e.:

$$0 \leq \beta^2 \epsilon' - 1 \leq \beta^2 \sin^2 \theta \quad (1.40)$$

The exponential term in the integrand of equation (1.39) shows that the Cherenkov field of frequency ω propagates at an angle $\vartheta(\omega)$ to the direction of motion where $\vartheta(\omega)$ is defined by

$$\sin \vartheta(\omega) = \frac{\sqrt{\beta^2 \epsilon'(\omega) - 1}}{\beta}$$

This result can be understood on the basis of the following observations. Cherenkov radiation of frequency ω moves at an angle given by $\cos \theta' = 1/\beta\sqrt{\epsilon'(\omega)}$ in the first medium. If the law of refraction is then applied, the angle $\vartheta(\omega)$ is given by the above expression. The left hand part of the double inequality in 1.40 is the condition for the production of Cherenkov radiation in the first medium. The right hand part, which may now be written in the form $\vartheta(\omega) \leq \theta$, indicates that the field at frequency ω moving at an angle $\vartheta(\omega)$ can be seen at angles larger than or equal to $\vartheta(\omega)$.

Using similar arguments, it is possible to obtain expressions for E'_{2n} and $H'_{2\phi}$. From equation (1.39) it is obvious that transition radiation and Cherenkov radiation do not interfere. The total amount of transition radiation emitted during the time of flight of the particle, in the solid angle $d\Omega = \sin \theta d\theta d\phi$ is

$$\frac{dW_{trans}}{d\Omega} = \frac{ce^2 \sin^2 \theta \cos^2 \theta}{\pi^2 v^2} \frac{\beta^4}{(1 - \beta^2 \cos^2 \theta)^2} \int_0^\infty \left[\frac{(\epsilon - 1)(1 - \beta^2 - \beta\sqrt{\epsilon - \sin^2 \theta})}{(\epsilon \cos \theta + \sqrt{\epsilon - \sin^2 \theta})(1 - \beta\sqrt{\epsilon - \sin^2 \theta})} \right]^2 d\omega \quad (1.41)$$

It has been shown in the above that transition radiation may be emitted by a charged particle crossing the boundary between media with different dielectric properties. The original work of Frank & Ginzburg (1945) dealt however with the a charge incident upon a metal and predicted that transition radiation, mainly in

the optical range, will be emitted in the backward direction i.e. observed in the vacuum. The more practical case for HEP is the case of highly relativistic particles which are able to pass through a medium and escape into vacuum, first treated by Garibian (1958). In this case the radiation emitted forwards, particularly when the charge moves from a medium into a vacuum, has a high frequency spectrum, lying in the X-ray frequency range. When integrated over angle and frequency the radiation intensity increases accordingly, and in the simplest case is proportional to γ , it is this which is the most significant characteristic for application in HEP.

Chapter 2

Mathematical Modelling of Transition Radiation

2.1 Practical Theory of Transition Radiation.

This chapter will discuss the development of a detailed mathematical model to simulate transition radiation for highly relativistic conditions, and a tool to simulate the generation of transition radiation applicable to experimental high energy physics. This will then be developed for the case of periodic structures of media with different dielectric properties, which introduces the need to simulate processes of interference and the propagation of transition radiation through media. Following on from this the study will be further developed to include the processes of detection used for transition radiation and the treatment of the main background processes. Alongside detailed results will be shown which were obtained from the mathematical simulation these illustrate the main characteristics of transition radiation and show how these can be accurately modelled.

The implementation of the full simulation programme within the GEANT detector description and simulation tool will be described which demonstrates the application of the simulation programme within the wider context of high

energy physics simulation. Finally a study to verify the simulation programme is presented based on experimental data obtained from test beam results of a prototype TRD.

An equation for the transition radiation emitted forward when a charged particle crosses the boundary between two media of different dielectric properties is given by Garibian (1961) as

$$\frac{d^2W}{d\omega d\Omega} = \frac{e^2 \beta^2 \mu_2 \sqrt{\varepsilon_2 \mu_2} |\varepsilon_2 - \varepsilon_1|^2 \sin^2 \theta \cos^2 \theta}{\pi^2 c |\varepsilon_1 \cos \theta + \sqrt{\varepsilon_2 / \mu_2} \sqrt{\varepsilon_1 \mu_1 - \varepsilon_2 \mu_2 \sin^2 \theta}|^2} \times \left| \frac{(1 - \beta \sqrt{\varepsilon_1 \mu_1 - \varepsilon_2 \mu_2 \sin^2 \theta} - \beta^2 \frac{\varepsilon_2 \mu_2 - \varepsilon_1 \mu_1}{\varepsilon_2 - \varepsilon_1} \varepsilon_2)}{(1 - \beta^2 \varepsilon_2 \mu_2 \cos^2 \theta)(1 - \beta \sqrt{\varepsilon_1 \mu_1 - \varepsilon_2 \mu_2 \sin^2 \theta})} \right|^2 \quad (2.1)$$

where as above $\varepsilon_{1,2}$ represents the electric permittivity, $\mu_{1,2}$ represents the magnetic permeability, and θ is the angle between the direction of radiation emission and the velocity of the incident particle.

For the case of a charged particle normally incident on the boundary between a medium of dielectric constant ε and vacuum i.e. $\varepsilon_1 = \varepsilon$, $\varepsilon_2 = 1$, $\mu_1 = \mu_2 = 1$ equation (2.1) is equivalent to equation (1.41) from Chapter 1.

For the case of high energy physics experiments, equation (2.1) must be transformed to highly relativistic conditions.

Under relativistic conditions, and $\mu_1 = \mu_2 = 1$, i.e. non magnetic materials $\varepsilon(\omega)$ can be represented by the asymptotic expression (Jackson 1998)

$$\varepsilon_{1,2}(\omega) = 1 - \frac{\omega_{1,2}^2}{\omega^2}$$

where $\omega_{1,2}$ represents the plasma frequency of the materials 1 and 2 such that

$$\omega_{1,2} = \frac{4\pi N_e e^2}{m_e}$$

where N_e is the electron density in the material, m_e is the electron mass and e is the electron charge.

Taking each of the terms in equation (2.1) in turn the simplification is made by substituting in values for $\varepsilon_{1,2}$ and remembering that $\beta^2 = (1 - \gamma^{-2})$ as well as that, from the Taylor expansion for the trigonometric functions, for very small θ $\sin \theta \sim \theta$ and $\cos \theta \sim 1 - \frac{1}{2}\theta^2$. Finally each term is expanded and negligibly small values are dropped.

$$\begin{aligned} (1 - \beta^2 \varepsilon_2 \cos^2 \theta) &\approx 1 - (1 - \gamma^{-2}) \left(1 - \frac{\omega_2^2}{\omega^2}\right) (1 - \theta^2) \\ &\approx \gamma^{-2} + \theta^2 + \frac{\omega_2^2}{\omega^2} \end{aligned}$$

$$\begin{aligned} (1 - \beta \sqrt{\varepsilon_1 - \varepsilon_2 \sin^2 \theta}) &\approx 1 - (1 - \frac{1}{2}\gamma^{-2}) \left[\left(1 - \frac{\omega_1^2}{\omega^2}\right) - \left(1 - \frac{\omega_2^2}{\omega^2}\right) \theta^2 \right]^{\frac{1}{2}} \\ &\approx \frac{1}{2} (\gamma^{-2} + \theta^2 + \frac{\omega_1^2}{\omega^2}) \approx \gamma^{-2} \end{aligned}$$

$$\begin{aligned} (\varepsilon_1 \cos \theta + \sqrt{\varepsilon_2} \sqrt{\varepsilon_1 - \varepsilon_2 \sin^2 \theta})^2 &\approx \left[\left(1 - \frac{\omega_1^2}{\omega^2}\right) \left(1 - \frac{1}{2}\theta^2\right) + \left(1 - \frac{1}{2}\frac{\omega_2^2}{\omega^2}\right) \times \right. \\ &\quad \left. \times \left(\left(1 - \frac{\omega_1^2}{\omega^2}\right) - \left(1 - \frac{\omega_2^2}{\omega^2}\right) \theta^2 \right)^{\frac{1}{2}} \right]^2 \approx 4 \end{aligned}$$

$$\left[1 - \beta \sqrt{\varepsilon_1 - \varepsilon_2 \sin^2 \theta} - \beta^2 \varepsilon_2 \right]^2 \approx \left[\gamma^{-2} - (1 - \gamma^{-2}) \left(1 - \frac{\omega_2^2}{\omega^2}\right) \right]^2 \approx 1$$

$$\beta^2 \sqrt{\varepsilon_2} \sin^2 \theta \cos^2 \theta \approx \left(1 - \frac{1}{2}\frac{\omega_1^2}{\omega^2}\right) (1 - \gamma^{-2}) \theta^2 (1 - \theta^2) \approx \theta^2$$

$$|\varepsilon_2 - \varepsilon_1| = \left| \frac{\omega_1^2}{\omega^2} - \frac{\omega_2^2}{\omega^2} \right|$$

recombining the simplified terms of equation (2.1) the equation for transition radiation for the relativistic case may be written as

$$\frac{d^2 W}{d\omega d\Omega} = \frac{e^2}{\pi^2 c} \theta^2 \left[\frac{1}{(\gamma^{-2} + \theta^2 + \frac{\omega_2^2}{\omega^2})} - \frac{1}{(\gamma^{-2} + \theta^2 + \frac{\omega_1^2}{\omega^2})} \right]^2 \quad (2.2)$$

Analysis of equation (2.2) shows that the concept of a time or length of formation can be introduced as a natural extension of the theoretical model. The

“formation zones” are defined by Frank (1970) as

$$Z_{1,2} = \frac{4\pi c}{\omega} \left(\frac{1}{\gamma^2} + \omega^2 + \frac{\omega_{1,2}^2}{\omega^2} \right)^{-1} \quad (2.3)$$

If it is assumed that $\theta \sim 1/\gamma$, then for $\omega \ll \omega_{1,2}\gamma$ the formation zone increases with increasing frequency as $Z_{1,2} = 4\pi c\omega/\omega_{1,2}$ and at frequencies of the order of $\omega_{1,2}\gamma$, it reaches a maximum

$$Z_{1,2,max} = \frac{2\pi c}{\omega_{1,2}}\gamma$$

Physically the formation zone is the distance along the particle trajectory in a given medium, after which the separation between the particle and generated photon is of the order of the photon wavelength, or the length needed for the electromagnetic field to reach its new state of equilibrium. The consequence of this is that an appreciable intensity is obtainable only when a charged particle is able to traverse a distance of the order of the formation zone in a medium. Whilst this is of no consequence in the case of a single interface, for the case of a single slab, and especially in the case of a thin slab, the effect can be quite appreciable and has the effect of suppressing the higher energy side of the spectrum for

$$\frac{4\pi c}{\omega} \left(\frac{1}{\gamma^2} + \omega^2 + \frac{\omega_{1,2}^2}{\omega^2} \right)^{-1} > l_{1,2}$$

where $l_{1,2}$ indicates the thickness of the media.

Finally to obtain an equation of transition radiation that may be used for practical study and application, taking $d\Omega = \sin\theta d\theta d\varphi$, the double differential spectrum can be given as follows

$$\frac{d^2W}{d\omega d\theta} = \frac{2\alpha\hbar}{\pi} \theta^3 \left[\frac{1}{(\gamma^{-2} + \theta^2 + \frac{\omega_2^2}{\omega^2})} - \frac{1}{(\gamma^{-2} + \theta^2 + \frac{\omega_1^2}{\omega^2})} \right]^2 \quad (2.4)$$

Integration of (2.4) over angle θ gives the differential frequency spectrum as:

$$\frac{dW}{d\omega} = \frac{\alpha\hbar}{\pi} \left[\left(\frac{\omega_2^2 + \omega_1^2 + 2\omega^2/\gamma^2}{\omega_2^2 - \omega_1^2} \right) \times \ln \left(\frac{1/\gamma^2 + \omega_2^2/\omega^2}{1/\gamma^2 + \omega_1^2/\omega^2} \right) - 2 \right] \quad (2.5)$$

Integrating (2.5) over frequency gives the total intensity of radiation emitted at a single interface:

$$W = \int \int \frac{d^2W}{d\omega d\theta} d\omega d\theta = \frac{\alpha\hbar(\omega_2 - \omega_1)^2}{\pi(\omega_2 + \omega_1)}\gamma \quad (2.6)$$

where $\gamma = E/m_0c^2$, $\alpha = e^2/\hbar c$ and $\hbar = h/2\pi$ where h is Planck's constant.

2.1.1 Analysis of Transition Radiation from a single interface

As a first step towards simulating transition radiation a computer programme was written to perform the numerical calculation of the double differential equation (2.4) over ω and θ . This was done over the photon energy interval $1\text{keV} < \hbar\omega < 500\text{keV}$ (using the relation $E = \hbar\omega$) and angle interval $0 < \theta < 180$. Analysis of the data obtained from the calculations allow the main features of the emitted transition radiation to be shown.

Analysis of equation (2.5) shows that the differential frequency spectrum is only dependent on γ and ω . If it is assumed that $\omega_2 > \omega_1$ e.g. in the case of a dense material and a gas, then equation (2.5) describing the differential frequency spectrum can be broken up into essentially three distinct regions having respectively, constant, logarithmic and power law dependence on γ and ω . These are

$$\frac{dW}{d\omega} = \begin{cases} \frac{2\alpha\hbar}{\pi} \left(\ln \frac{\omega_2}{\omega_1} - 1 \right), & \omega < \gamma\omega_1 \\ \frac{2\alpha\hbar}{\pi} \ln \frac{\gamma\omega_2}{\omega}, & \gamma\omega_1 < \omega < \gamma\omega_2 \\ \frac{\alpha\hbar}{6\pi} \left(\frac{\gamma\omega_2}{\omega} \right)^4, & \gamma\omega_2 < \omega \end{cases}$$

Due to the large power law dependence on γ and ω above frequency $\omega = \gamma\omega_2$ the radiation intensity drops off rapidly to small values.

This is illustrated in Fig. 2.1 which displays the distribution of $dW/d(\hbar\omega)$, the computed differential yield (keV/keV), as a function of photon energy calculated

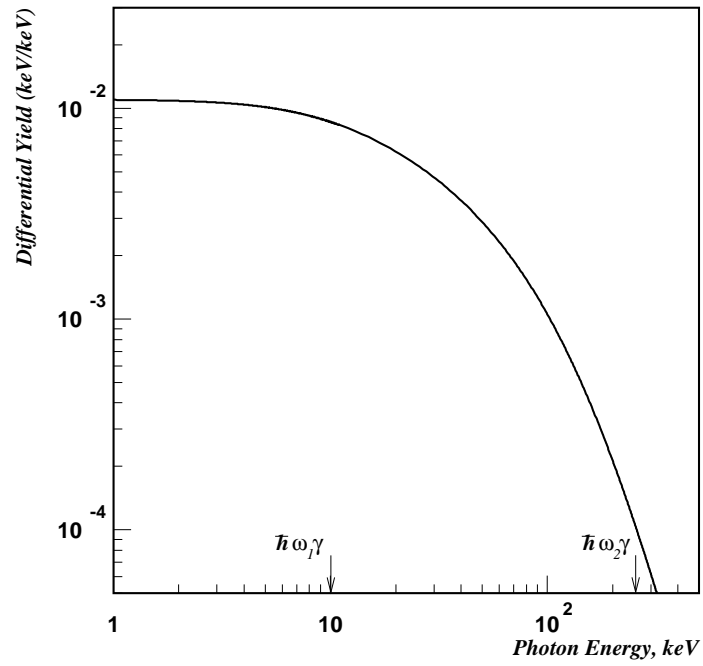


Fig. 2.1: The computed differential yield (keV/keV) as a function of $\hbar\omega$, the transition radiation photon energy, for a charged relativistic particle with a Lorentz factor $\gamma = 10000$ traversing a single mylar-air interface. $\hbar\omega_1\gamma = 10$ keV and $\hbar\omega_2\gamma = 250$ keV.

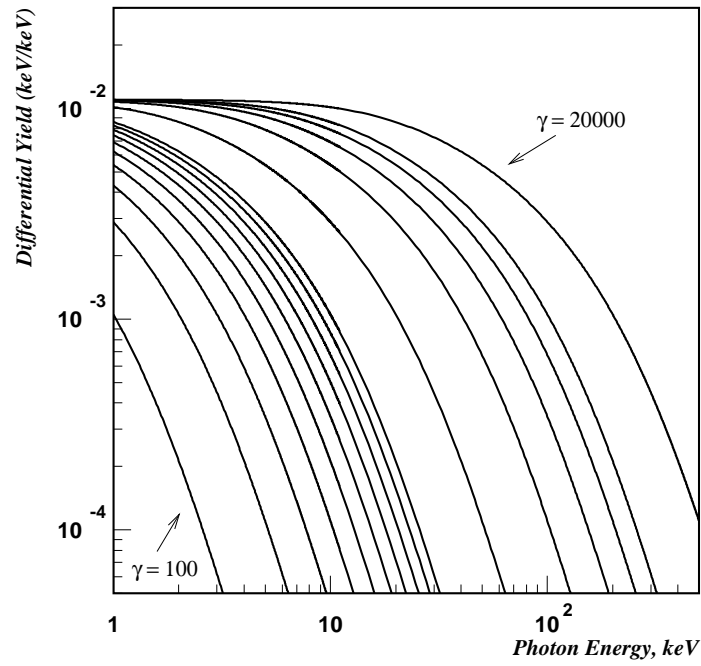


Fig. 2.2: The computed differential yield (keV/keV) as a function of $\hbar\omega$, the transition radiation photon energy, for a charged relativistic particle traversing a single mylar-air interface, for different Lorentz factor, over the range $\gamma = 100 - 20,000$ (increasing left to right).

by the computer programme for a charged relativistic particle with a Lorentz factor $\gamma = 10000$ crossing a single mylar-air interface. The values of $\hbar\omega_2$ and $\hbar\omega_1$ for mylar and air are 25×10^{-3} keV and 1×10^{-3} keV respectively. For this case, the three distinct regions where the frequency spectrum has constant, logarithmic and power law dependence, are clearly visible. The computed differential yield, as a function of photon energy calculated by the computer programme is also shown in Fig. 2.2 for the same case with different γ , over the range 100-20,000.

As can be seen in equation (2.6) the total radiation intensity increases linearly with γ essentially due to the fact that the photon energy spectrum becomes harder with increasing γ . It should be noted that measurements which are only sensitive in a limited energy interval would not follow a linear dependence but develop into a logarithmic behaviour and eventually reach saturation when $\gamma > \omega/\omega_2$. The logarithmic dependence would persist only for large values of γ if one of the two media were vacuum, $\omega_2 = 0$.

The angular distribution is obtained by integration of equation (2.4) over frequency. The distribution of the radiation as a function of θ is given by

$$\frac{d^2W}{d\omega d\theta} = 2\pi\theta \frac{d^2W}{d\omega d\Omega}, \theta \ll 1$$

This function vanishes as θ^3 for $\theta \rightarrow 0$ and has a sharp maximum for $\theta \sim 1/\gamma$.

The transition radiation emitted by an ultra-relativistic charged particle normally incident on an interface between two dielectrics is azimuthally symmetric about the trajectory of the particle and is confined to a narrow forward cone. This is illustrated in the two plots Fig. 2.3 and Fig. 2.4.

Fig. 2.3 shows a cylindrical plot of the transition radiation intensity, in arbitrary units, against the angle, in mrad, between the emission of transition radiation photons and the direction of motion of the incident charged particle which is denoted by the arrowed marked e ($\gamma = 1800$). Fig. 2.4 shows the projection of Fig. 2.3 - giving the angular distribution of transition radiation intensity for

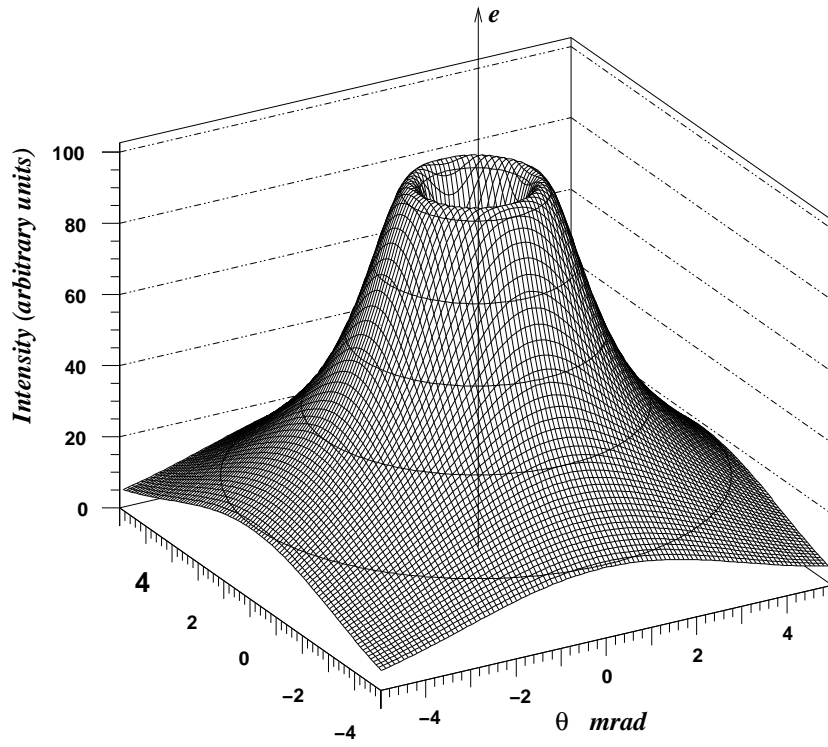


Fig. 2.3: Cylindrical plot showing the angular distribution of transition radiation intensity from a relativistic charged particle ($\gamma = 1800$) normally incident on an interface between two dielectrics, whose direction is denoted by the arrow marked e . It can be seen that the emission of transition radiation photons is azimuthally symmetric about the trajectory of the particle and is confined to a narrow forward cone.

different values of γ .

At frequencies high enough that $\omega_1/\omega \ll \gamma^{-1}$, the angular distribution of the radiation is essentially independent of ω , $\frac{d^2W}{d\omega d\theta}$ falls as θ^{-5} for large angles, relative to γ^{-1} and the radiation is confined to angles $\theta \leq \gamma^{-1}$ (Durand 1975). However as has already been discussed the differential intensity of the radiation $\frac{dW}{d\omega}$ is quite small in this limit. A more interesting case is that in which $1 \gg \omega_1/\omega \gg \gamma^{-1}$. In this case $\frac{d^2W}{d\omega d\theta}$ decreases as θ^{-1} for $\gamma^{-1} \leq \theta \leq \omega_1/\omega$ and is cut off as θ^{-5} only for $\theta \gg \omega_1/\omega$. The angular distribution of the radiation is consequently much broader than in the previous case but the radiation is still confined to a narrow cone if $\omega_1/\omega \ll 1$, for the relativistic case this leads to the emitted radiation being extremely peaked in the forward direction at an angle $\theta \sim \gamma^{-1}$ visible in Fig. 2.4.

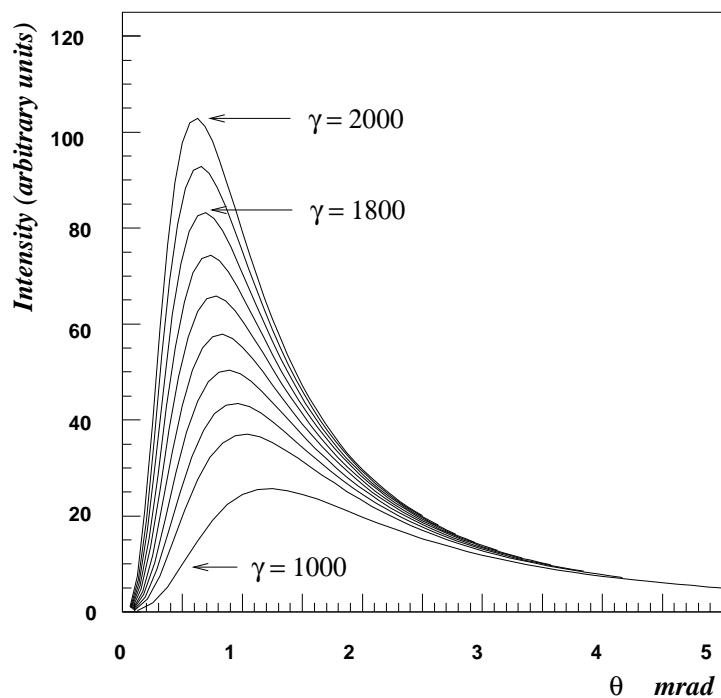


Fig. 2.4: Angular distribution of transition radiation intensity from a relativistic charged particle for the range $\gamma = 1000 - 2000$. The distribution for $\gamma = 1800$ is the projection of the cylindrical plot from Fig. 2.3. It can be seen that the emitted radiation is peaked in the forward direction at an angle $\theta \sim \gamma^{-1}$.

2.2 Theory of Transition Radiation for Periodic Structures

2.2.1 Generation of Transition Radiation in a Periodic Structure

In practice, the incident charge traverses at least two interfaces, for example a single slab. Also due to the low yield per interface of transition radiation, $W_0 \propto \alpha$, the fine structure constant, the effect must be enhanced for practical purposes. To achieve this enhancement a periodic structure consisting of a set of thin slabs equally spaced, may be used, this is known as a periodic radiator.

At this point it is convenient to draw an analogy between double slit interference and the formation of transition radiation and associated wave effect phenomena. This is shown simplistically in Fig. 2.5. The incident particle may be seen as a plane wave moving along the axis of the slits which are turned through 90 degrees. This leads to a phase shift $(\phi_2 - \phi_1)$ at P from both spatial separation, responsible for the interference effects of the classical double slit experiment, and temporal separation resulting from the difference in time at which the charged particle crosses the interfaces of the slab. This effect should be taken into account when considering the formation of transition radiation .

For a detailed analysis of the transition radiation created by a charged particle traversing a periodic structure consider a configuration of N parallel slabs with dielectric constant ε_1 and uniform thickness l_1 , spaced at regular distances l_2 in a medium of dielectric constant ε_2 , where $\omega_1 > \omega_2$, see Fig. 2.6.

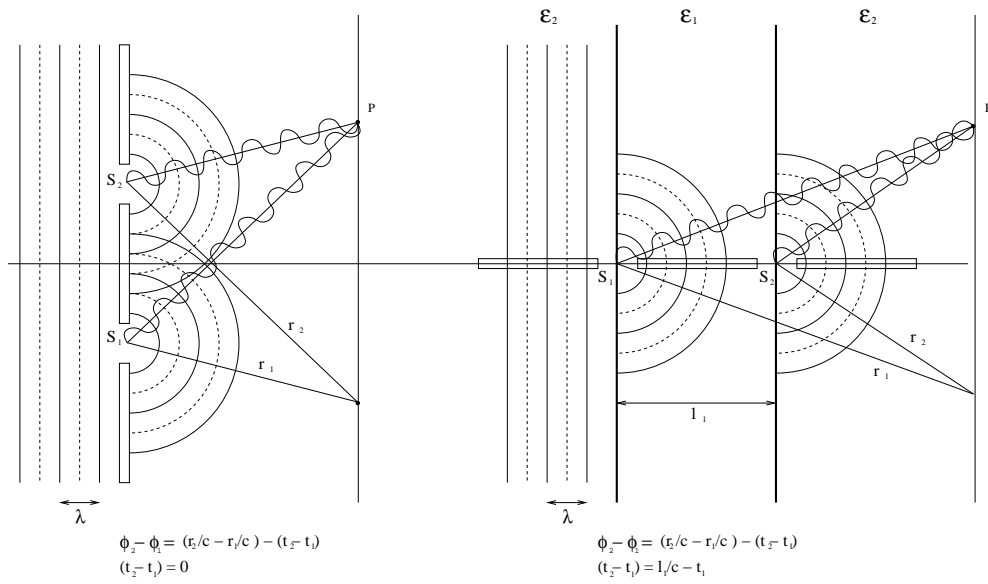


Fig. 2.5: Analogy of interference effects from two interfaces producing transition radiation and double slit interference

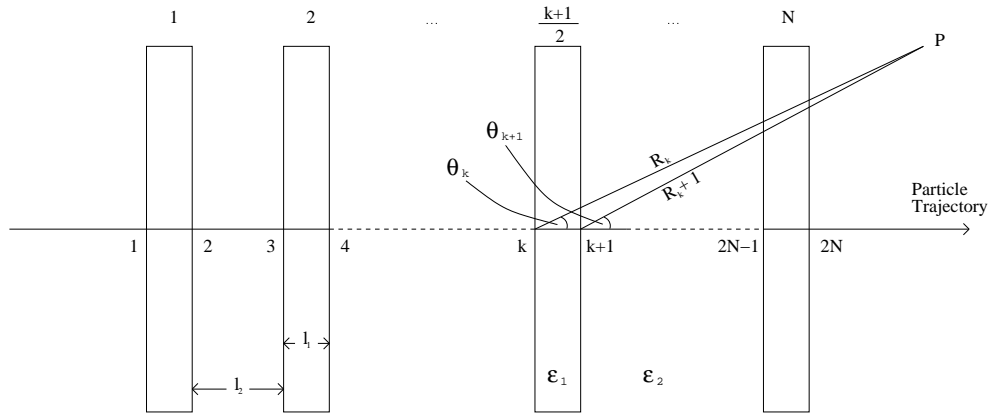


Fig. 2.6: Schematic diagram of a charged particle traversing a periodic structure of slabs with thickness l_1 consisting of a medium with dielectric constant ϵ_1 spaced at a distance of l_2 within a medium with dielectric constant ϵ_2 . l_1 and l_2 remain constant throughout the periodic structure. R_k (R_{k+1}) represents the distance from point at which the particle traverses foil k ($k + 1$) to the point of observation P . θ_k (θ_{k+1}) represents the angle between R_k (R_{k+1}) and the particle trajectory.

In order to calculate the intensity of transition radiation generated when a highly relativistic charge traverses the stack of slabs perpendicular to their surface, it is necessary to consider the field amplitudes at some observation point P . At point P the field amplitudes E and H should be the coherent sum of the radiation amplitudes from $2N$ interfaces taking into account the correct phase factor, bearing in mind that the particle traverses different interfaces at different times. The radiation intensity for a single interface is given in Eq. (2.4), the corresponding electric field amplitude in the wave zone for a charge traversing from medium 1 into medium 2 is

$$E_{12} = \frac{A(\theta)}{R} e^{i\phi}$$

Where

$$A(\theta) = e\beta\xi \sin\theta \cos\theta / \pi cR, r$$

$$\phi = \omega\left(\frac{R}{c} - t\right),$$

$$\xi = 2(\varepsilon_2 - \varepsilon_1) / \left[\left(\frac{1}{\gamma^2} + \theta^2 + \frac{\omega_1^2}{\omega^2} \right) \left(\frac{1}{\gamma^2} + \theta^2 + \frac{\omega_2^2}{\omega^2} \right) \right],$$

R = distance to P

t = time.

Conversely for a charge traversing from medium 2 into medium 1

$$E_{21} = -E_{12} = -\frac{A(\theta)}{R} e^{i\phi}$$

The field may then be expressed as a coherent addition of the amplitudes for successive interfaces alternate in sign:

$$E(P) = \sum_{k=1}^{2N} \frac{(-1)^k A(\theta_k) e^{i\phi_k}}{R_k} \quad (2.7)$$

where ϕ_k is the phase factor for radiation from the k th interface, R_k is the distance to P from the interface and θ_k is the angle between the charge trajectory and the direction of P

If P is sufficiently large, a few orders of magnitude greater than the wavelength of the radiation, then the far zone approximation may be used. In this case it may be taken that

$$R_k \approx R, \quad \theta_k \approx \theta \quad (2.8)$$

for all k .

Continuing and taking account of (2.8) equation (2.7) may then be rewritten as

$$\begin{aligned} E(\theta, R) &= \frac{A(\theta)}{R} \sum_{k=1}^{2N} (-1)^k e^{i\phi_k} \\ &= \frac{A(\theta)}{R} \left[e^{i\phi_1} \sum_{k=0}^{N-1} e^{i(\phi_{2k+1} - \phi_1)} - e^{i\phi_2} \sum_{k=1}^N e^{i(\phi_{2k} - \phi_2)} \right] \end{aligned} \quad (2.9)$$

looking at Fig. 2.6 it can be seen from the geometry that as slab thickness, l_1 , and the gap between slabs, l_2 , are constant the phase difference, $\Delta\phi = \phi_{k-2} - \phi_k$, between any two successive even numbered or successive odd numbered interfaces is a constant independent of k , and therefore

$$\phi_{2k} - \phi_2 = \phi_{2k-1} - \phi_1 = (k-1)\Delta\phi \quad (2.10)$$

in terms of the relevant parameters, taking spatial and temporal separation into account,

$$\Delta\phi = \frac{\omega}{c} \left[(l_1\sqrt{\varepsilon_1} + l_2\sqrt{\varepsilon_2}) \cos\theta - \frac{l_1 + l_2}{\beta} \right] \quad (2.11)$$

Substituting equation (2.10) into equation (2.9) gives

$$E(\theta, R) = \frac{A(\theta)}{R} (e^{i\phi_1} - e^{i\phi_2}) \sum_{n=0}^{N-1} e^{in\Delta\phi} \quad (2.12)$$

where

$$\sum_{n=0}^{N-1} e^{in\Delta\phi} = \frac{e^{iN\Delta\phi} - 1}{e^{i\Delta\phi} - 1} = e^{i(N-1)\Delta\phi/2} \frac{\sin(N\Delta\phi/2)}{\sin(\Delta\phi/2)}$$

with further manipulations, equation (2.12) may be written as

$$E(\theta, R) = \frac{A(\theta)}{R} e^{i(\phi_1 + \phi_2 + \pi)/2} e^{i(N-1)\Delta\phi/2} \times \\ \times 2 \sin\left(\frac{\phi_1 - \phi_2}{2}\right) \frac{\sin(N\Delta\phi/2)}{\sin(\Delta\phi/2)}$$

The magnetic field amplitude H may be found in a similar fashion.

Once E and H are known the differential radiation intensity at point P may be found by calculating the Pointing vector. This leads to

$$\frac{d^2W_N}{d\theta d\omega} = \frac{c}{4\pi} \int_{-\infty}^{\infty} \int_0^{2\pi} EHR^2 \sin\theta d\phi dt \\ = \frac{d^2W_0}{d\theta d\omega} 4 \sin^2\left(\frac{\phi_1 - \phi_2}{2}\right) \frac{\sin^2(N\Delta\phi/2)}{\sin^2(\Delta\phi/2)} \quad (2.13)$$

Finally it remains to express ϕ and $(\phi_1 - \phi_2)/2$ explicitly in terms of the relevant parameters l_1 , l_2 , ω_1 , ω_2 , and γ . Using equation (2.11) and the approximations $\beta = 1 - 1/2\gamma^2$, $\cos\theta = 1 - \theta^2/2$, and $\sqrt{\varepsilon_{1,2}} = 1 - (\omega_{1,2}^2/2\omega^2)$ it is found that

$$|\Delta\phi| = \frac{\omega}{2c} \left[l_1 \left(\frac{1}{\gamma^2} + \theta^2 + \frac{\omega_1^2}{\omega^2} \right) + l_2 \left(\frac{1}{\gamma^2} + \theta^2 + \frac{\omega_2^2}{\omega^2} \right) \right] \\ = 2 \left(\frac{l_1}{Z_1} + \frac{l_2}{Z_2} \right) \quad (2.14)$$

where Z_1 and Z_2 are the ‘‘formation zones’’ given in equation (2.3). Similarly

$$\frac{|\phi_1 - \phi_2|}{2} = \frac{l_1}{Z_1} \quad (2.15)$$

substituting equation (2.14) and equation (2.15) into equation (2.13) gives the differential spectrum of X-ray radiation for a periodic radiator of N slabs with thickness l_1 and separation l_2

$$\frac{d^2W_N}{d\theta d\omega} = \frac{d^2W_0}{d\theta d\omega} 4 \sin^2\left(\frac{l_1}{Z_1}\right) \frac{\sin^2[N(l_1/Z_1 + l_2/Z_2)]}{\sin^2[(l_1/Z_1 + l_2/Z_2)]} \quad (2.16)$$

For the case $N = 1$, a single slab, the radiation yield of a single slab of material reduces to

$$\frac{d^2W_N}{d\theta d\omega} = \frac{d^2W_0}{d\theta d\omega} 4 \sin^2\left(\frac{l_1}{Z_1}\right) \quad (2.17)$$

from inspection of the equation (2.17) it can be seen that if the slab thickness exceeds the formation zone of the slab material,

$$l_1 \gg Z_1(\theta, \omega)$$

then the term $4 \sin^2 \left(\frac{l_1}{Z_1} \right)$ oscillates rapidly as compared to the range in which $d^2W/d\theta d\omega$ varies considerably. This leads to modulation of the differential energy spectrum.

Returning to the general form of the periodic radiator for the case where the spacing of the slabs is greater than the formation zone of the gap material,

$$l_2 \gg Z_2(\theta, \omega)$$

in this case the period of the last term of equation (2.16) is very small in comparison with the range in which $d^2W/d\theta d\omega$ varies, therefore it is possible to write

$$\frac{\sin^2[N(l_1/Z_1 + l_2/Z_2)]}{\sin^2[(l_1/Z_1 + l_2/Z_2)]} \approx N$$

Thus the observed yield from a periodic radiator is well approximated by N times the yield of a single slab.

2.2.2 Analysis of Transition Radiation in Periodic Structures

The integration of equation (2.16) with respect to θ was performed by Ter-Mikaelian and Garibian (Cherry, Hartmann, Mueller & Prince 1974) giving :

$$\begin{aligned} \frac{dW_N}{d\omega} = & 2\alpha\hbar c N (\omega_1^2 - \omega_2^2)^2 \frac{(l_1 + l_2)^2}{\omega^2} \\ & \times \sum_{r=r_{min}}^{r_{max}} \left\{ \sin^2 \left[\frac{l_2}{l_1 - l_2} \left(\frac{l_1}{4\omega c} (\omega_1^2 - \omega_2^2) - \pi r \right) \right] \right. \\ & \left. \times \frac{2\pi c r - \frac{(l_1+l_2)\omega}{2\gamma^2} - \frac{l_1\omega_1^2 + l_2\omega_2^2}{2\omega}}{\left[\frac{l_1(\omega_1^2 - \omega_2^2)}{2\omega} - 2\pi c r \right]^2 \left[\frac{l_2(\omega_1^2 - \omega_2^2)}{2\omega} - 2\pi c r \right]^2} \right\} \end{aligned} \quad (2.18)$$

the summation is performed over all numbers r within the limits $r_{min} \leq r \leq r_{max}$, where

$$r_{min} = \frac{l_1 + l_2}{2\pi\gamma c} \left(\frac{l_1\omega_1^2 + l_2\omega_2^2}{l_1 + l_2} \right)^{1/2}$$

$$r_{max} = \gamma r_{min}$$

for each value of r , Eq.(2.18) must be evaluated only in a specified frequency region:

$$\omega = \begin{cases} \geq \gamma^2 \left\{ \frac{2\pi cr}{l_1+l_2} + \left[\left(\frac{2\pi cr}{l_1+l_2} \right)^2 - \frac{l_1\omega_1^2 + l_2\omega_2^2}{\gamma^2(l_1+l_2)} \right]^{1/2} \right\} \\ \leq \gamma^2 \left\{ \frac{2\pi cr}{l_1+l_2} - \left[\left(\frac{2\pi cr}{l_1+l_2} \right)^2 - \frac{l_1\omega_1^2 + l_2\omega_2^2}{\gamma^2(l_1+l_2)} \right]^{1/2} \right\} \end{cases}$$

In order to move from a single interface to the simulation of a periodic radiator a further computer programme was written to perform the numerical calculation of equation (2.18). Once again this was done over the the photon energy interval $1\text{keV} < \hbar\omega < 500\text{keV}$ and $0 < \theta < 180$.

Fig. 2.7 presents the computed differential yield (keV/keV) normalised to the number of interfaces as a function of photon energy calculated by the computer programme for a charged relativistic particle traversing a periodic structure of mylar-air interfaces for different Lorentz factor, over the range $\gamma = 100 - 20,000$. The effect of the term $4 \sin^2 \frac{l_1}{Z_1}$ is clearly visible in the spectrum producing the predicted modulation. This effect is more prominent for higher γ especially at high ω . For highly relativistic particles it can be seen that the main part of the spectrum lies in the soft X-ray region from 3 keV to 50 keV. As in the case of the single interface the spectrum is limited at the frequency $\gamma\omega_1$. For transition radiation close to saturation, the main part of the spectrum is contained in the high frequency peak at $\omega = l_1\omega_1^2/2\pi c$.

Through the variation of l_1, l_2 in equation (2.18) it was possible to analyse the dependence of transition radiation on l_1, l_2 , which is necessary to start radiator optimisation studies. These are shown in the following distributions.

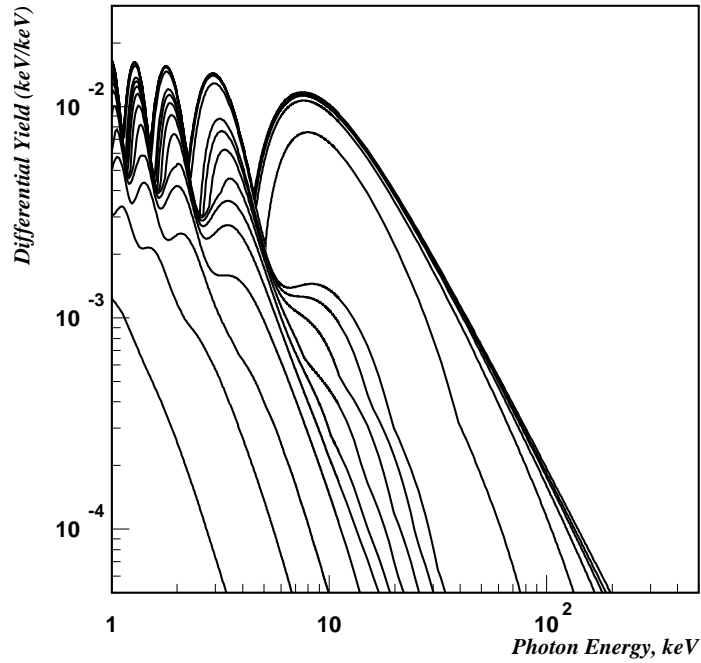


Fig. 2.7: The computed differential yield (keV/keV) normalised to the number of interfaces as a function of $\hbar\omega$, the transition radiation photon energy, for a charged relativistic particle traversing a periodic structure of mylar-air interfaces, for different Lorentz factor, over the range $\gamma = 100 - 20,000$ (increasing left to right as in Fig. 2.1). Modulation of the spectrum due interference is clearly visible.

Fig. 2.8 presents the computed differential yield (keV/keV) normalised to the number of interfaces as a function of $\hbar\omega$, the transition radiation photon energy, for a charged relativistic particle traversing a periodic structure of mylar-air interfaces, for different l_1 . Analysis of the dependency of the transition radiation spectrum on l_1 shows both the increasing frequency of oscillation of the modulation, and the shift of the last maximum towards high frequencies with increasing l_1 . This possibility to shift the last maximum to higher frequencies, especially those in the X-ray region, is an important feature of transition radiation for the purposes of real application.

Fig. 2.9 presents the computed differential yield (keV/keV) normalised to the number of interfaces as a function of $\hbar\omega$, the transition radiation photon energy, for a charged relativistic particle traversing a periodic structure of mylar-air interfaces, for different l_2 . Whilst the increase in l_2 only weakly effects the position of the last maximum it leads to an increase in the amplitude of modulation, although in any case the value of l_2 should not be less than the formation zone of its medium, as doing so would cause a reduction of the yield until it reached that of a single slab ($l_2 = 0$).

The results obtained from analysis of the distribution for different l_1 and l_2 are shown as surface plots in Fig. 2.10 and Fig. 2.11 for electrons of momentum 20 GeV/c and 50 GeV/c respectively. These plots give the possibility to optimise the structure of a transition radiator through the adjustment of the parameters l_1 and l_2 .

From this analysis of transition radiation in a periodic structure, it is possible to summarise the main features of transition radiation which are important for practical application.

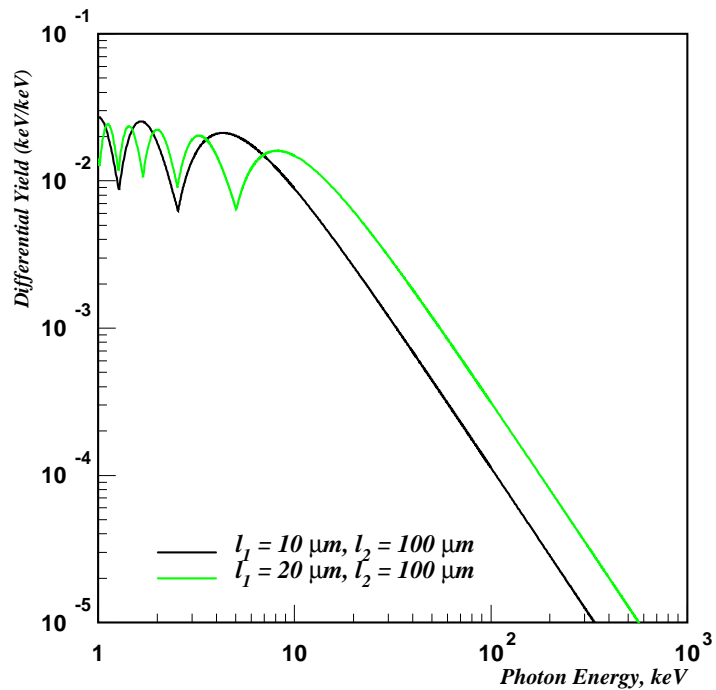


Fig. 2.8: The computed differential yield (keV/keV) normalised to the number of interfaces as a function of $\hbar\omega$, the transition radiation photon energy, for a charged relativistic particle traversing a periodic structure of mylar-air interfaces, for different l_1 .

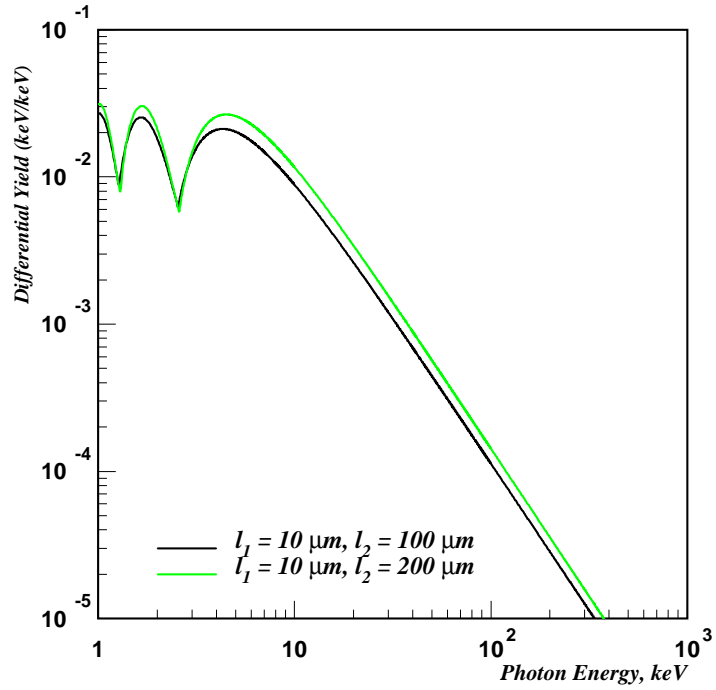


Fig. 2.9: The computed differential yield (keV/keV) normalised to the number of interfaces as a function of $\hbar\omega$, the transition radiation photon energy, for a charged relativistic particle traversing a periodic structure of mylar-air interfaces, for different l_2 .

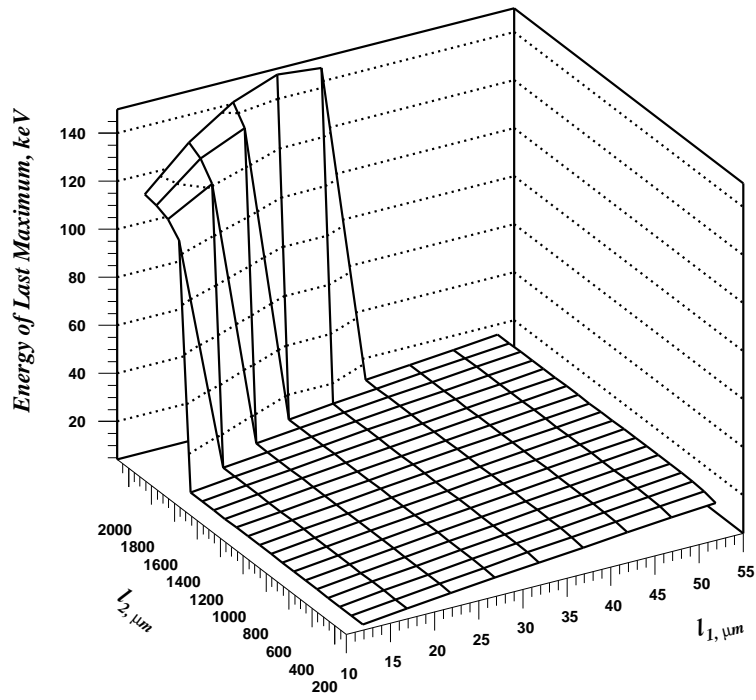


Fig. 2.10: Surface plot showing the energy of the last maximum as a function of l_1 and l_2 for 20 GeV electrons.

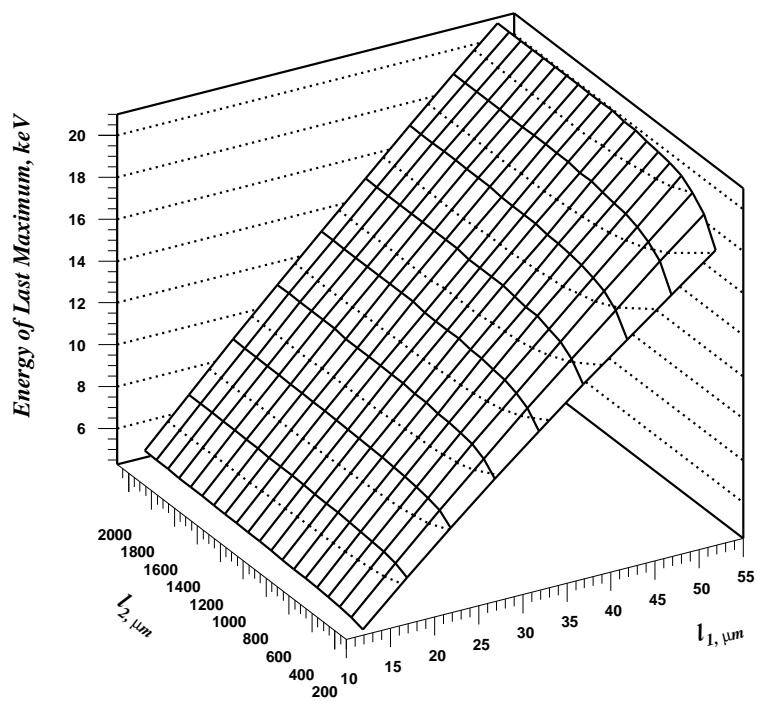


Fig. 2.11: Surface plot showing the energy of the last maximum as a function of l_1 and l_2 for 50 GeV electrons.

Features of transition radiation for the relativistic case:

- The total energy lost via transition radiation increases proportionally with the Lorentz factor of the particle (see equation (2.6)), essentially due to the fact that the radiation spectrum becomes harder with increasing γ . It shows that the linear dependence on γ can be used to discriminate between single charged particles with similar momentum but different mass;
- Most of the emission takes place within a cone of half angle $1/\gamma$. The effect is strongly peaked in the forward direction and is symmetric, concerning the crossing medium.
- The electrodynamic nature of the transition radiation indicates that at an interface the probability of creating a photon is of the order of the fine structure constant, $\alpha = 1/137$.
- A stack of N slabs may be used to enhance the total radiation yield which is needed for experimental purposes by factor $\sim N$.

2.3 Propagation of Transition Radiation in Periodic Structures

2.3.1 Main Processes

A periodic radiator in the form of a stack of slabs with a finite thickness also leads to another problem, namely the reabsorption of the radiation emitted by the slab material itself.

Due to the photon's lack of electrical charge it is not open to the many elastic collisions with atomic electrons so characteristic of charged particles. Instead the main interactions of photons in matter are:

- Photoelectric Absorption
- Incoherent (Compton) Scattering, Coherent (Thomson and Rayleigh) Scattering
- Pair Production

Also possible, but much less common are nuclear dissociation reactions, for example (γ, n) , which due to their extremely low cross section will not be considered here.

At low energy it is photoelectric absorption which dominates, at energies approaching the order of 10 keV this is replaced as the dominant process by incoherent scattering. Finally once the threshold for pair production is reached, twice the rest mass of an electron (1.022MeV), this process rapidly becomes the most dominant.

The attenuation of a narrow beam of mono-energetic photons with an incident intensity I_0 , traversing a medium of thickness l and density ρ , may be given by the exponential attenuation law

$$I/I_0 = e^{-(\mu/\rho)x}$$

where x is the mass thickness given by $x = \rho l$. This may be measured experimentally although present tabulations of μ/ρ rely heavily on theoretical values for the total cross section per atom, σ_{tot} , which is related to μ/ρ via

$$\mu/\rho = \sigma_{tot}/uA$$

where u is the atomic mass unit and A is the relative atomic mass of the target element.

For the purposes of transition radiation the energy range of interest is that of soft X-rays, one to a few tens of keV, where the photoelectric effect and incoherent scattering are most prevalent, this is shown for Xenon in Fig. 2.12. As the energy threshold for pair production is well above that of soft X-rays it will not be discussed further. Therefore, in this case, the total cross section can be written as

$$\sigma_{tot} = \sigma_{pe} + \sigma_{coh} + \sigma_{incoh}$$

where σ_{pe} is the atomic photoelectric cross section, σ_{coh} and σ_{incoh} are the coherent and incoherent scattering cross sections.

Photoelectric Absorption

Photoelectric absorption is a quantum process involving the absorption of a photon by an atomic electron with the subsequent ejection of the electron from the atom. The energy of the outgoing electron is then

$$E = \hbar\omega - B.E.$$

where $B.E.$ is the binding energy of the atomic electron. Since a free electron cannot absorb a photon and also conserve momentum, the photoelectric effect always occurs on bound electrons where the nucleus absorbs the recoil momentum. The absorption cross section as a function of energy of the photoelectric effect is

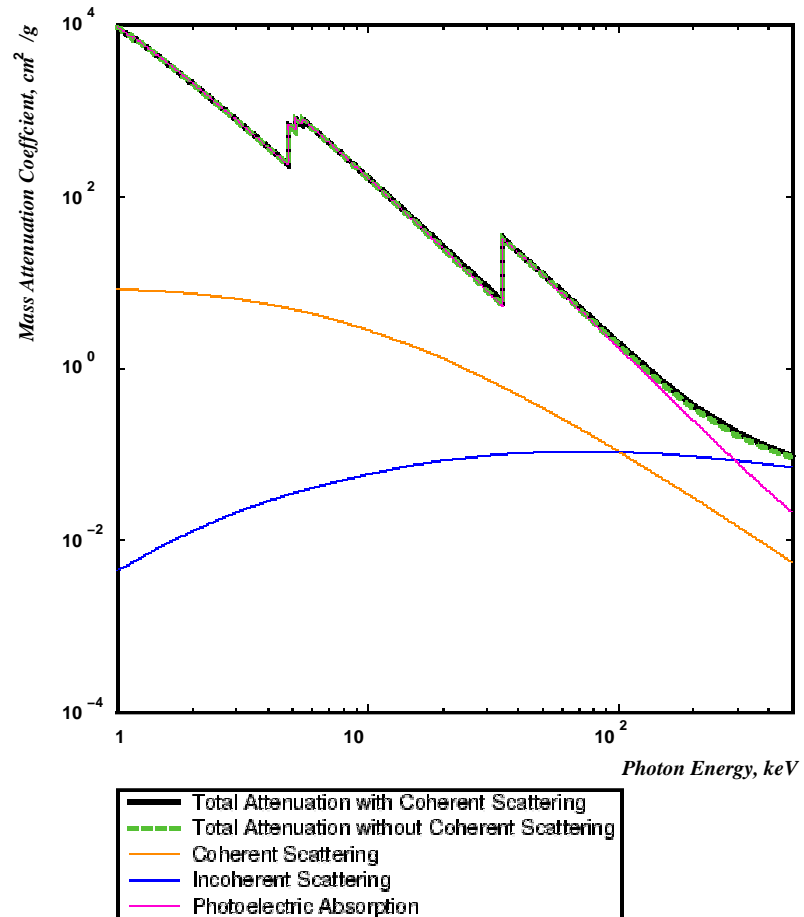


Fig. 2.12: Mass attenuation coefficient of Photons in Xe, over the energy range 1-500 keV (Berger et al. 1999).

characterised by discontinuities, the so called absorption edges, these are due to the discrete binding energies of the atomic electrons (see Fig. 2.12). At energies above the highest electron binding energy of the atom, the K-shell, the cross section is relatively small but increases rapidly as the K-shell energy is approached. Immediately after this point, the cross section drops drastically since the K-shell electrons are no longer available. Below this energy the cross section rises once again and falls as the L, M, etc. edges are passed.

Theoretically the photoelectric effect is difficult to treat rigorously because of the complexity of the Dirac wave-functions for the atomic electrons. For photon energies above that of the K-shell, however it is almost always the K electrons which are involved. This is the case for all light elements except the heavier noble gases. If this is assumed and the energy is non-relativistic i.e. $\hbar\omega \ll m_e c^2$ the cross section can then be calculated using a Born approximation. In such case the following expression is obtained

$$\sigma_{pe} = 4\alpha^4 \sqrt{2Z^5 \sigma_{thom} (m_e c^2 / \hbar\omega)^{7/2}}, \quad \text{per atom} \quad (2.19)$$

where $\sigma_{thom} = 8\pi r_e^2 / 3 = 6.651 \times 10^{-25} \text{cm}^2$ known as the Thomson cross section which was derived for the scattering of photons by atoms, r_e is the classical electron radius and Z is the atomic number of the atom. For energies closer to the K-edge (2.19) must be modified to give

$$\sigma_{pe} = \phi_0 \frac{2^7 \pi (137)^3}{Z^2} \left[\frac{\omega_k}{\omega} \right] \frac{\exp(-4\xi \cot^{-1} \xi)}{1 - \exp(-2\pi\xi)}, \quad \text{per atom} \quad (2.20)$$

where $\hbar\omega_k = (Z - 0.02)^2 m_e c^2 \alpha^2 / 2$ and $\xi = \sqrt{\omega_k / (\omega - \omega_k)}$. For ω very close to ω_k , $\xi^{-1} \gg 1$, so that (2.20) can be simplified to

$$\sigma_{pe} = \frac{6.3 \times 10^{-18}}{Z^2} \left(\frac{\omega_k}{\omega} \right)^{\frac{8}{3}}$$

Formulas for the L and M shells have also been calculated, but these are more complex than those above and are beyond the scope of this thesis, for a more complete discussion see (Scofield 1973).

Incoherent Scattering (Compton Scattering)

Incoherent scattering is the scattering of photons on free electrons. Although the electrons in matter are bound, if the photon energy is high with respect to the binding energy, the latter may be neglected and the electron considered essentially free.

The cross section for incoherent scattering is derived from quantum electrodynamics and is known as the Klein-Nishina formula (Klein & Nishina 1929):

$$\frac{d\sigma_{incoh}}{d\Omega} = \frac{r_e^2}{2} \frac{1}{[1 + \gamma_c(1 - \cos \theta)]^2} \left(1 + \cos \theta + \frac{\gamma_c^2(1 - \cos \theta)^2}{1 + \gamma_c(1 - \cos \theta)} \right)$$

where θ is angle of scattering and $\gamma_c = \hbar\omega/m_e c^2$, integration of this formula over $d\Omega$ gives the scattering cross section per electron for incoherent scattering,

$$\sigma_{incoh} = 2\pi r_e^2 \left\{ \frac{1 + \gamma_c}{\gamma_c^2} \left[\frac{2(1 + \gamma_c)}{1 + 2\gamma_c} - \frac{1}{\gamma_c \ln(1 + 2\gamma_c)} \right] + \frac{1}{2\gamma_c} \ln(1 + 2\gamma_c) - \frac{1 + 3\gamma_c}{(1 + 2\gamma_c)^2} \right\}$$

Coherent scattering (Thompson and Rayleigh scattering)

Coherent scattering (Thompson and Rayleigh scattering) is the scattering of photons by atoms as a whole. In both processes the scattering is characterised by the fact that no energy is transferred to the medium. The atoms are neither excited nor ionised only the direction of the photon is changed. As in the applicable energy range the atomic cross section σ_{coh} is dominated by σ_{pe} , coherent scattering will no longer be considered.

2.3.2 Analysis of Transition Radiation Spectrum Including Absorption Processes within a Periodic Structure

In order to properly describe the transition radiation spectrum escaping from the radiator, the absorption of the transition radiation X-rays within the radiator was included in the simulation programme.

Due to the effect of photoelectric absorption and incoherent scattering within the radiator, equation (2.16) must be modified:

$$\frac{d^2W_N}{d\theta d\omega} = \frac{d^2W}{d\theta d\omega} 4 \sin^2 \left(\frac{l_1}{Z_1} \right) \frac{\sin^2[N(l_1/Z_1 + l_2/Z_2)]}{\sin^2(l_1/Z_1 + l_2/Z_2)} \left| \frac{1 - C^N}{1 - C} \right|^2 \quad (2.21)$$

where

$$C = \exp(il_1/z_1 + il_2/z_2 - l_1\sigma_1 - l_2\sigma_2)$$

and σ_1 and σ_2 describe the atomic cross section for materials 1 and 2 respectively.

Data on the scattering and absorption of photons are required for many scientific, engineering and medical applications. The values needed are traditionally given in table form (Hubbell 1969) and exist for most but not all elements, some tables (Henke, Lee, Tanaka, Shimabukuro & Fujikawa 1982) also contain data for a limited number of compounds and mixtures.

Photon cross sections for compounds can be obtained as weighted sums of the cross sections for the atomic constituents. However this is complicated by the fact that photon-absorption cross sections and mass attenuation coefficient are discontinuous at absorption edges. The presence of these discontinuities makes it desirable that cross section tables for compounds include photon energies immediately above and below all absorption edges for all the atomic constituents.

An alternative approach is to generate the cross sections and mass attenuation coefficients for compounds and mixtures as needed, for such purpose a web programme called XCOM (Berger et al. 1999) exists which is able to carry out this task for most elements, and many compounds or mixtures at energies between 1 keV and 100 GeV.

Using the XCOM programme it is possible to generate cross sections on a standard energy grid (spaced approximately logarithmically), or on a grid selected if supplied. Cross sections at energies immediately above and below all absorption edges are automatically included. XCOM is able to provide two forms of output:

(a) table format traditionally used in the literature; (b) graphical display of the tabular data.

XCOM produces the tables using a comprehensive database of all elements constructed through the combination of photoelectric absorption from Scofield (1973), and incoherent scattering from Hubbell, Veigele, Briggs, Brown, Cromer & Howerton (1975). The photoelectric absorption cross sections were obtained by Scofield (1973) by a phase-shift calculation for a central potential and a Hartree-Slater atomic model up to an energy of 1.5 MeV, well above the energy range for the current study. The incoherent scattering cross sections in (Hubbell et al. 1975) were obtained from a combination of the Klein-Nishina formula and non-relativistic Hartree-Fock incoherent scattering functions.

Making use of XCOM it was possible to obtain total cross sections and mass attenuation coefficients as well as partial cross sections in table form. This was done for both photoelectric absorption and incoherent scattering.

Some limitations should be noted. The cross sections for elements in the XCOM database are for isolated neutral atoms and do not take into account molecular and solid-state effects which modify the cross sections, especially in the vicinity of absorption edges.

An algorithm for interpolation was introduced to allow the tables to be used in the programme. The result from the calculation of the absorption coefficient in the appropriate energy region for transition radiation photons is shown in Fig. 2.13. Analysis of Fig. 2.13, clearly shows a 10^3 reduction in the total attenuation over the photon energy interval 1 – 10 keV, as can be seen photoelectric absorption is almost entirely responsible for the absorption of photons within the medium in this energy interval.

This data is applied to the spectrum of transition radiation emitted by a periodic structure shown in Fig. 2.7, the results are presented in Fig. 2.14 which

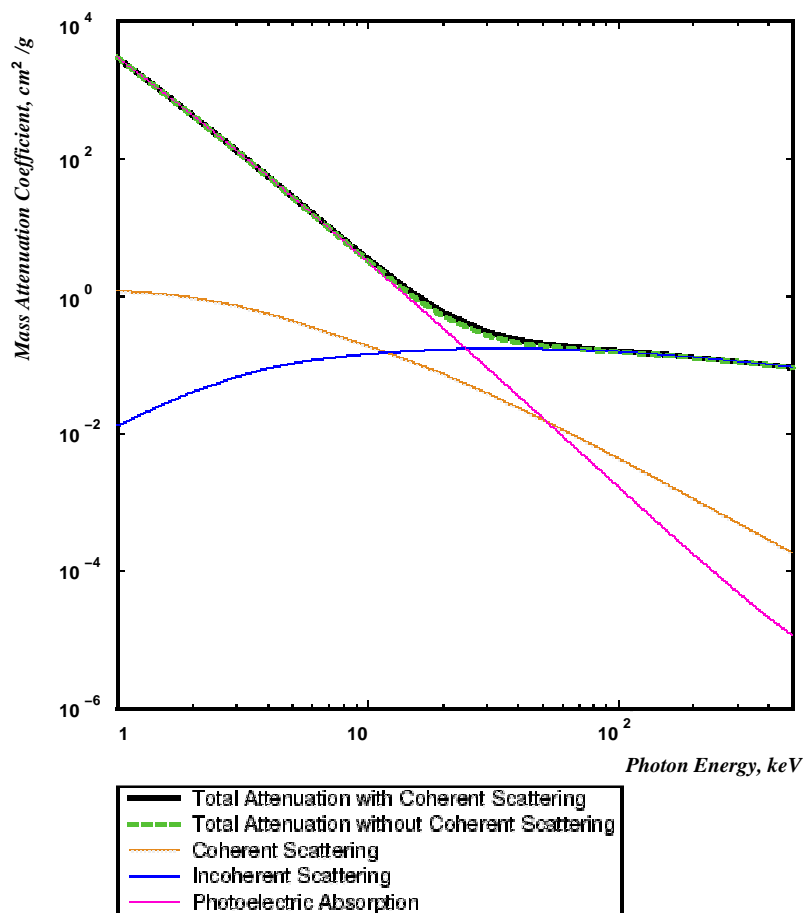


Fig. 2.13: Mass attenuation coefficient of Photons in Mylar over the energy range 1-500 keV (Berger et al. 1999).

shows distributions of transition radiation intensity as a function of photon energy normalised to the number of slabs for a typical slab material i.e. Mylar (polyethylene terephthalate) over the transition radiation photon energy range 1 – 500 keV. In comparison with Fig. 2.7, the distribution to the left of ~ 10 keV is heavily suppressed. As a result the effective number of slabs is limited by saturation that occurs when increases in emission and reabsorption of X-rays (as a function of the number of slabs) reach equilibrium, and therefore must be optimised for practical application.

2.4 Detection of Transition Radiation

2.4.1 Detection of X-ray Transition Radiation

The simplest structure for a transition radiation detector consists of a periodic structure (radiator) placed directly in front of an X-ray detector. The above analysis has shown that to efficiently detect transition radiation from a periodic structure an X-ray detector must be sensitive to X-rays within the energy range 3 keV to 30 keV.

In such structures, due to the angular distribution of the transition radiation emitted, the X-rays emitted from a radiator cannot be separated from the particle in time and space (unless a strong bending magnetic field is used to deflect the charged particle). Any X-ray detector will therefore see the signal from transition radiation on top of a large signal due to ionisation losses of the associated particle in the detector. Such limitations lend themselves to a detector design which consists of thin layers of high Z material thick enough to allow for efficient absorption of the X-rays whilst thin enough to limit the ionisation loss signal which constitutes the background signal for transition radiation detection.

The detection efficiency of an X-ray detector depends on both the geometry

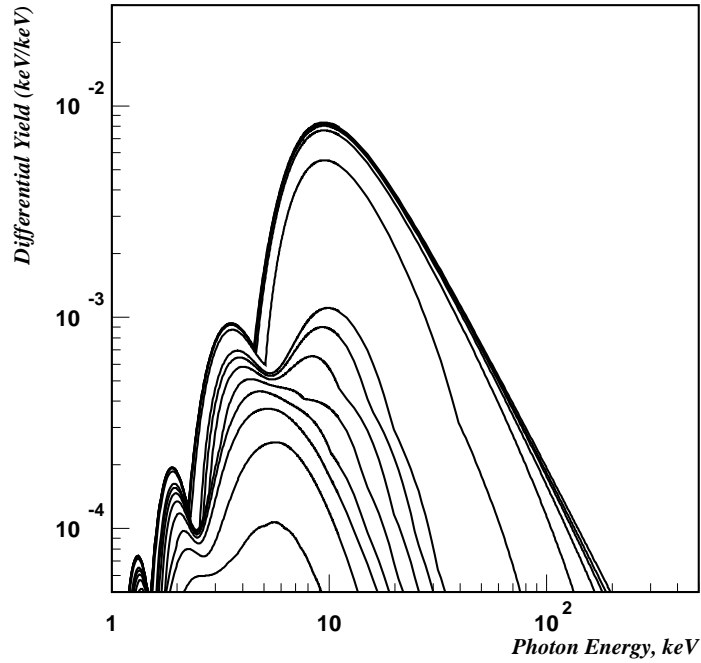


Fig. 2.14: The computed differential yield (keV/keV) normalised to the number of interfaces as a function of $\hbar\omega$, the transition radiation photon energy, for a charged relativistic particle traversing a periodic structure of mylar-air interfaces taking absorption within the radiator into account, for different Lorentz factor, over the range $\gamma = 100 - 20,000$ (increasing left to right as in Fig. 2.1).

and the characteristics of the sensitive volume. The physical process of detection is photoelectric absorption, which has been described above.

The optimum thickness for a detector is approximately one absorption length of X-rays at an energy of approximately 10 keV. Traditionally the detection of X-rays in this energy region is done using gas proportional chambers. The best candidates for use as the detection gas are Krypton and Xenon, their mass attenuation coefficients, which are dominated in this region by photoelectric absorption, are shown together in Fig. 2.15. As can be seen at 10 keV Xenon has a significantly higher mass attenuation coefficient than Krypton, one radiation length at 10 keV corresponds to a thickness of about 10 mm for Xenon and 50mm for Krypton.

Importantly, the background for detection of transition radiation X-rays in a proportional chamber originates mainly from ionisation losses of the charged particle (this will be discussed in detail later). Thus the choice of gas used should yield the best ratio of absorption length to the ionisation loss of the charged particle in the gas. Due to absorption within the radiator material itself the transition radiation X-ray spectrum has a natural threshold at ~ 4 keV; and such it is necessary to consider energy losses of the particle in the gas where the transferred energy exceeds ~ 4 keV. In this case the leading candidate is Xenon which has a good ratio of absorption length to ionisation loss, a factor of ≈ 1.3 .

For the separation of high energy electrons, for whom the dE/dx losses are already in the region of the relativistic Fermi plateau, and relatively slow hadrons, i.e. minimum ionising particles, the considerable contribution to the electron signal is given by the relativistic rise of dE/dx . Again Xenon is the best candidate.

To simulate the absorption of transition radiation photons within the X-ray detector the simulation programme was once again extended to make use of the tables produced by the XCOM programme.

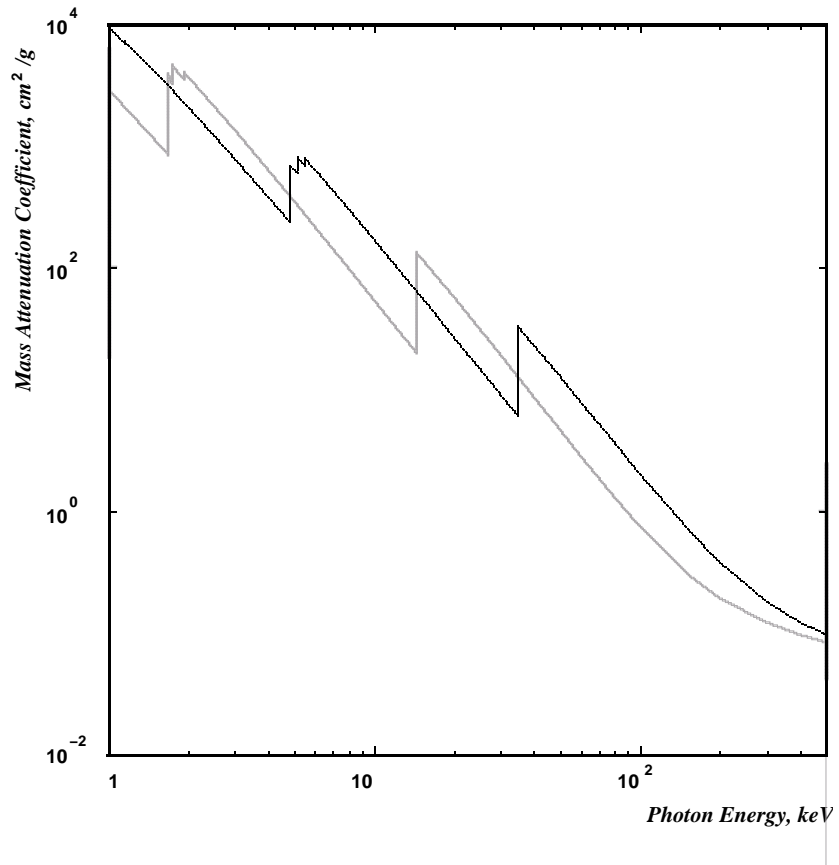


Fig. 2.15: Mass attenuation coefficients as a function of X-ray energy for Xenon (black line) and Krypton (grey line) over the energy range 1-500 keV (Berger et al. 1999).

The results produced by the programme for the differential yield (keV/keV) normalised to the number of interfaces absorbed in Xenon are shown in Fig. 2.16, clearly visible within the transition radiation spectrum are the discontinuities resulting from those present in the absorption coefficient of Xenon. This addition to the programme gives the possibility to simulate and optimise proportional chambers for detecting X-ray transition radiation photons for different gases, thicknesses and geometry.

When optimising the thickness of the Xenon gas layer the following must be considered; a smaller thickness will lead to a deterioration of the identification capability of the TRD due to of less efficient X-ray detection, a thicker layer would increase background from dE/dx losses. These two facts explain the flat optimum of the rejection power as a function of the Xenon gas thickness.

2.4.2 Background Signal

As discussed above the main background signal when detecting transition radiation comes from energy losses of the associated incident charged particle within the sensitive detector volume. This energy loss is primarily the result of inelastic collisions between the incident charged particle and the atomic electrons of the sensitive detector material. In such collisions energy is transferred from the particle to the atom causing ionisation or excitation of the latter. In the case of ionisation resulting from collisions where high energy transfers take place, it is possible for the ejected atomic electrons to produce further ionisation within the sensitive detector material. These ionising atomic electrons are known as δ electrons.

The mean rate of energy loss ($-d\bar{E}/dx$) for moderately relativistic charged particles in matter is well described by the Bethe-Bloch equation (Hagiwara et al.

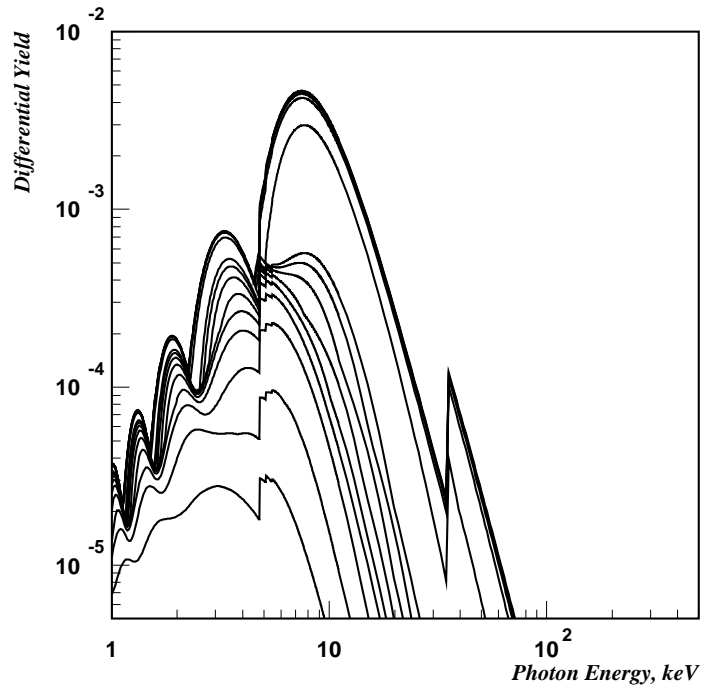


Fig. 2.16: The computed differential yield (keV/keV) normalised to the number of interfaces as a function of $\hbar\omega$, the transition radiation photon energy, for a charged relativistic particle traversing a periodic structure of mylar-air interfaces taking absorption in Xe into account, for different Lorentz factor, over the range $\gamma = 100 - 20,000$ (increasing left to right as in Fig. 2.1). The effect of the characteristic absorption edges of the L and K shells in Xe on the spectrum is clearly visible at 4.8 keV and 35 keV respectively.

2002).

$$-\frac{d\bar{E}}{dx} = Kz^2 \frac{Z}{A} \frac{1}{\beta^2} \left[\frac{1}{2} \ln \frac{2m_e c^2 \beta^2 \gamma^2 T_{max}}{I^2} - \beta^2 - \frac{\delta}{2} \right]$$

Here T_{max} is the maximum kinetic energy which can be imparted to a free electron in a single collision. With K defined as $4\pi N_A r_e^2 m_e c^2$, where N_A is Avogadro's number, r_e is the Classical electron radius, m_e is electron mass. I represents the mean excitation energy, Z and A represent the atomic number and atomic mass of the absorber respectively, z^2 is the charge of the incident particle and δ is the density effect correction.

In this form the Bethe-Bloch equation describes the energy loss of pions in a material such as copper very well for energies between about 6 MeV and 6 GeV. At lower energies various corrections must be made to account for atomic bindings and the asymmetry between positive and negative particles. At higher energies radiative effects cease to be negligible and must be included. These limits of validity depend both on the effective atomic number of the absorber and the mass of the slowing particle.

The Bethe-Bloch equation has been modified to cover the energy range 0.01 – 100 GeV and provides accurate estimates of the mean energy loss of charge particle as a function of x .

However due to the stochastic nature of the interaction process of a charged particle with matter both the number of collisions and the energy transferred in the individual collisions exhibit fluctuations and consequently so do the ionisation energy losses occurring in a sample of matter of thickness, x . This is especially significant in sufficiently thin samples of matter in which the energy loss is significantly lower than the particle energy, $\overline{\Delta E} \ll E$, and fluctuations in energy losses during individual collisions becomes important.

For relatively thick absorbers where the number of collisions is large, the energy loss distribution may be easily shown to be Gaussian in form. This follows

directly from the Central Limit Theorem of statistics which states that the sum of N random variables, all following the same statistical distribution, approaches that of a Gaussian-distributed variable in the limit $N \rightarrow \infty$.

In contrast to the case of a thick absorber the distribution for thin absorbers or gases, where the number of collisions N is too small for the Central Limit Theory to hold, is more complicated.

The probability $p(x, N)$ that a particle will undergo N collisions in a sample of matter of thickness, x , is determined taking account of the above considerations by the Poisson distribution, with an average value, $\bar{N} = x d\bar{N}/dx$

$$p(x, N) = \left(\frac{\bar{N}^N}{N!} \right) e^{(-\bar{N})} \quad (2.22)$$

To calculate the probability of energy loss, $f(x, \Delta)$, it is necessary to take into account that the probability, W_1 , of an energy loss ϵ occurring in a single collision is

$$W_1(\epsilon) = \frac{d^2 \bar{N}}{dx d\epsilon} \bigg/ \frac{d\bar{N}}{dx} = \frac{1}{\sigma} \frac{d\sigma}{d\epsilon}$$

where

$$\int_0^\infty W_1(\epsilon) d\epsilon = 1 \quad \text{and} \quad W_1(\epsilon) = 0 \quad \text{at} \quad \epsilon < 0$$

Consequently in the case of N collisions

$$W_N(\epsilon) = W_1(\epsilon) * W_1(\epsilon) * \dots * W_1(\epsilon) \quad N \text{ times,}$$

where the symbol $*$ indicates convolution over the variable ϵ :

$$W_1(\epsilon) * W_1(\epsilon) = \int_0^\epsilon W_1(\epsilon') W_1(\epsilon - \epsilon') d\epsilon'$$

Taking into account that $W_0(\epsilon) = \delta(\epsilon)$, and using equation(2.22), gives

$$\begin{aligned}
f(x, \Delta) &= \sum_{N=0}^{\infty} e^{(-\bar{N})} \frac{\bar{N}^N}{N!} W_N(\Delta) \\
&= e^{(-\bar{N})} \left\{ \delta(\Delta) + x \frac{d^2 \bar{N}}{dx d\Delta} \right. \\
&\quad \left. + \frac{x^2}{2} \int_0^{\Delta} \frac{d^2 \bar{N}(\Delta')}{dx d\Delta} \frac{d^2 \bar{N}(\Delta - \Delta')}{dx d\Delta} d\Delta' + \dots \right\} \quad (2.23)
\end{aligned}$$

In equation (2.23), the first term gives the distribution of energy loss upon passage of a particle through a layer x without collision, the second term gives the distribution in the case that a single collision takes place, and so on.

The convolution method is only applicable for small x , when \bar{N} is not too large. In the case that \bar{N} is too large the calculations become too cumbersome, since convolutions with $N \geq \bar{N}$ have to be determined. At the same time, as \bar{N} increases, the details of the behaviour of $W_1(\Delta)$ as a function of Δ become less and less essential, since they are smoothed out statistically in $W_N(\Delta)$. In these conditions the Landau method is more convenient, leading in fact to an approximate calculation of equation(2.23) for $\bar{N} \gg 1$ (Landau 1944).

The Bohr, Landau, Vavliov and Blunk-Leisegang approximations

The Landau approach is based on a solution of the kinetic equation for $f(x, \Delta)$

$$\frac{\partial f(x, \Delta)}{\partial x} = \int_0^{T_0} w(\epsilon) [f(x, \Delta - \epsilon) - f(x, \Delta)] d\epsilon \quad (2.24)$$

with the initial condition $f(0, \Delta) = \delta(\Delta)$

Here

$$w(\epsilon) = \bar{N} W_1(\epsilon) = x \frac{d^2 \bar{N}}{dx d\epsilon} = x N_a \frac{d\sigma}{d\epsilon}$$

where T_0 represents the maximum energy of δ electrons which do not escape registration. The solution of equation (2.24) is found with the aid of the Laplace

transformation,

$$\hat{L}f(x, \Delta) \equiv \int_0^\infty f(x, \Delta) e^{-p\Delta} d\Delta = e^{-G(x,p)}$$

where

$$G(x, p) = \int_0^{T_0} w(\epsilon)[1 - e^{-p\epsilon}] d\epsilon \quad (2.25)$$

The inverse Laplace transformation of (2.25) yields the following solution of (2.24)

$$f(x, \Delta) = \frac{1}{2\pi i} \int_{-i\infty}^{i\infty} e^{p\Delta - G(x,p)} dp \quad (2.26)$$

Equation (2.23) can be obtained from (2.26) by expansion in powers of $G(x, p) - \bar{N}$. It must be noted though that it's integration with a reasonable spectrum of the number of collisions, $w(\epsilon)$, can be accomplished only in certain special cases. The main difficulty consists in that the integrals of rapidly oscillating functions in (2.25) and (2.26) converge weakly. In order to compute them several methods have been proposed.

In (2.26) the value of the variable $p \sim 1/\Delta_{\text{eff}}$ is essential where Δ_{eff} represents the effective energy loss for which $f(x, \Delta)$ noticeably differs from zero. If $\Delta_{\text{eff}} \gg T_0$, i.e. if the average number of collisions in a sample is very large, such that $\bar{N} \gg \Delta_{\text{eff}} \gg T_0 \gg 1$, then the integrand in (2.25) can be expanded in powers of $p\epsilon \ll T_0/\Delta_{\text{eff}}$. Taking into account only the term which is linear in p yields $f(x, \Delta) \approx \delta(\Delta - \bar{\Delta})$ where $\bar{\Delta} = x(-d\bar{E}/dx) = \int_0^{T_0} w(\epsilon)\epsilon d\epsilon$, i.e. this signifies total neglect of fluctuations. The terms proportional to p and p^2 result in a Gaussian distribution for $f(x, \Delta)$, first obtained by Bohr (Bethe & Ashkin 1953):

$$f(x, \Delta) = \frac{1}{\sqrt{2\pi\overline{\Delta E^2}}} \exp\left[-\frac{(\Delta - \bar{\Delta})^2}{2\overline{\Delta E^2}}\right]$$

where

$$\overline{\Delta E^2} = \int_0^{T_0} w(\epsilon)\epsilon d\epsilon$$

As $x \propto \Delta_{\text{eff}}$ decreases and accordingly, p increases this expansion usually ceases to be valid. However it can be applied for those collisions corresponding to

sufficiently small energy transfers: $\epsilon \lesssim \epsilon_1$ for $\epsilon_1 p \sim \epsilon_1 / \Delta_{\text{eff}} \ll 1$. To this end it is necessary to single out in (2.25) the contributions of “far” ($\epsilon \leq \epsilon_1$) and “close” ($\epsilon \geq \epsilon_1$) collisions for which $\epsilon_1 \gg I$ and therefore possible to make use of the Rutherford collision spectrum for Coulomb scattering of particles on electrons.

$$\sigma_R = 2\pi \int_0^{\varrho_{\text{max}}} \varrho d\varrho = \frac{2\pi z^2 e^4}{m_e v^2} \int_{\epsilon_{\text{min}}}^{\epsilon_{\text{max}}} \frac{d\epsilon}{\epsilon^2} = \frac{8\pi z^2 e^4}{v^2} \int_{q_{\text{min}}}^{q_{\text{max}}} \frac{dq}{q^3}$$

where m_e is the electron mass; $q = \sqrt{2m_e \epsilon}$ is the momentum transferred by the particle to the electron; e is the charge of an electron and Ze is the particle’s charge; ϱ is the impact parameter and ϵ represents the energy transferred to the electron. Such that

$$w(\epsilon) = \xi / \epsilon^2 \tag{2.27}$$

where

$$\xi = x \frac{2\pi N_a Z e^4}{m_e v^2} = x \varrho 0.1536 \frac{Z}{A} \frac{1}{\beta^2}$$

here ξ is expressed in MeV and x in cm. Consequently,

$$G(x, p) = \int_0^{\epsilon_1} w(\epsilon) \left(p\epsilon - \frac{p^2 \epsilon^2}{2} + \frac{p^3 \epsilon^3}{6} - \dots \right) d\epsilon + \xi \int_{\epsilon_1}^{T_0} [1 - \exp(-p\epsilon)] d\epsilon / \epsilon^2 \tag{2.28}$$

for samples of matter which satisfy the conditions

$$I \ll \xi \ll T_0 \tag{2.29}$$

in (2.28) one may possible to consider only the first terms of the sum and set $T_0 \rightarrow \infty$. It is noted that in accordance with the general theory of ionisation loss the average number of collisions $\bar{N} = x d\bar{N}/dx \sim 10\xi/I$. Consequently (2.29) signifies that $\bar{N} \gg 10$, i.e. the samples of matter considered are not too thin; (application of the convolution method for these is quite difficult). Taking into account only the first term in the expansion (2.28) results in the Landau

distribution

$$f(x, \Delta) = \frac{1}{\xi} \phi(\lambda)$$

where $\phi(\lambda)$ is the universal Landau function:

$$\phi(\lambda) = \frac{1}{2\pi i} \int_{-i\infty}^{i\infty} \exp(u\lambda + u \ln u) du$$

$$\lambda = \frac{\Delta - \Delta_0}{\xi} - 0.225$$

The expression for the most probable energy loss Δ_0 taking account of the correction for the density effect, δ_E (Sternheimer & Peierls 1971), and corrections made by (Maccabee & Papworth 1969) has the form

$$\Delta_0 = \xi \left[\ln \frac{2m_e v^2 \xi}{I^2(1 - \beta^2)} - \beta^2 + 0.198 - \delta_E \right]$$

which is similar to the average restricted energy loss for $T_0 = 1.22\xi$. Taking account of the first two terms in the sum (2.28) gives the Blunk-Leisegang distribution (Blunk & Leisegang 1950). Generalisation of the Landau theory to the case of an arbitrary ratio, ξ/T_0 when a precise computation of the second integral in (2.28) is required, was first performed by (Vavilov 1957):

$$f_V(x, \Delta) = \frac{\exp[k(1 + \beta^2 0.577)]}{\pi T_0} \int_0^\infty \exp(k f_1) \cos(y \lambda_1 + k f_2) dy$$

where subscript V indicates Vavilov, and

$$f_1 = \beta^2 [\ln y - Ci(y)] - \cos y - y Si(y);$$

$$f_2 = y [\ln y - Ci(y)] + \sin y - \beta^2 Si(y);$$

$$\lambda_1 = k\lambda + k \ln k;$$

$$k = \xi/T_0$$

Si and Ci are the integral sine and cosine, respectively. When $\xi/T_0 \lesssim 0.01$ then the Vavilov solution transforms into the Landau distribution and when $\xi/T_0 \gg 1$ the

Vavilov solution transforms into a Gaussian distribution. As pointed out above all these solutions describe fluctuations of energy loss in short range collisions ($\epsilon \gg I$) where the analytic expression (2.27) is known for the collision spectrum, $w_R(\epsilon)$. As to the long-range collisions, in the Landau distribution fluctuations of the corresponding energy loss are not taken into account at all, the term in (2.28) is linear in p , while the Blunk-Leisegang correction only takes them into account approximately, in the form of a Gaussian distribution. An analysis of the relative contribution of the terms in the expansion (2.28) reveals that the Landau and Blunk-Leisegang theories are not applicable for $\xi/I \lesssim 10$ and for $\xi/I \lesssim 3$ respectively, due to the terms of expansion (2.28) alternate in sign, the Landau theory lowers, while the Blunk-Leisegang theory enhances the width of the distribution $f(x, \Delta)$. Indeed in the case of very low density samples of matter ($x \sim 1 - 10\text{mg/cm}^2$) the experimental distributions of ionisation energy loss are significantly broader than in the Landau theory and narrower than predicted by the (x, Δ) Blunk-Leisegang theory.

2.4.3 Analysis of Ionisation losses in thin gas proportional chambers

In modern experimental conditions for detection of transition radiation using gas proportional chambers, the thickness of the gas volume is approximately equal to, or less than a few cm, and in many cases of the order of a few mm.

For such conditions the estimation of accuracy of the Landau theory and Blunk & Leisegang (1950), described above, was calculated by Ermilova & Chechin (1976) who showed that the Landau approximation fails for $\xi/I \lesssim 10$ and is only valid when $\xi/I \gtrsim 100$. Although the Blunk-Leisegang correction slightly extends the region of the theory application its accuracy is 30% for $\xi/I \sim 1$ and $\sim 3\%$ only for $\xi/I \gtrsim 10$.

Thus, none of the existing theoretical approaches is able to explain all experimental features of ionisation energy loss distributions for relativistic charged particles in thin gas absorbers.

Ispirian, Margarian & Zverev (1974) were the first to apply Monte Carlo methods to the calculation of energy loss fluctuations of fast charged particles in matter. These authors based their calculations on approximated expressions for energy transfer spectra which were derived from the Sternheimer formula for mean energy loss (Sternheimer & Peierls 1971). A more realistic approach was suggested by Cobb, Allison & Bunch (1976) who were able to calculate both energy loss fluctuations and relativistic rise of the most probable energy loss in Argon by Monte Carlo methods, giving rather good agreement with experimental data. Nevertheless care should be taken concerning these results as the mean excitation potential of Argon was taken as 30% lower than is usually suggested (Sternheimer & Peierls 1971) and (Ermilova, Chechin, Alakoz, Konteko & Merzon 1975).

Ermilova, Konteko & Merzon (1977) used Monte Carlo methods in their calculation of fluctuations and the most probable values of relativistic particle energy loss in thin gas layers. Here they used energy transfer spectra in individual collisions which were calculated for polarised matter with distributed oscillator strengths $f(\omega)$ which they derived from experimental photon-absorption coefficients of matter (Ermilova et al. 1975). The mean excitation potentials obtained according to this method showed excellent agreement with experimental data for rare gases (Ermilova et al. 1975).

The integral presentation of energy transfer spectra, i.e. the number of collisions per unit length which have an energy transfer of more than a given value ϵ

can be written as follows (Ermilova et al. 1977):

$$\begin{aligned} \left(\frac{dN}{dx}\right)_{>\epsilon} &= \frac{A}{\beta^2} \left\{ \int_{\epsilon}^{\epsilon_{max}} \frac{f(\epsilon)}{\epsilon} \times \right. \\ &\quad \times \left[\ln \frac{2m_e c^2 \beta^2}{\epsilon(1-\beta^2) - \beta^2 + 1 - \epsilon/\epsilon_{max}} \right] d\epsilon \\ &\quad \left. + (1/\epsilon - 1/\epsilon_{max}) \int_0^{\epsilon} f(\epsilon) d\epsilon - \Delta(\beta, \epsilon) \right\} \end{aligned} \quad (2.30)$$

Here $\Delta(\beta, \epsilon)$ is the density effect correction which is dependent on β and ϵ given by Ermilova et al. (1977). ϵ_{max} is the energy of a delta electron with a range equal to the typical detector length.

The energy transfer spectrum in the Fermi plateau region can be calculated on the basis of the restricted energy loss as (Ermilova et al. 1975)

$$\left(\frac{-dE}{dx}\right)_{<\epsilon}^{pl} = AF(\epsilon) \ln \frac{2m_e c^2 \epsilon}{\omega_p^2 F(\epsilon)}$$

$F(\epsilon)$ being the total oscillator strength for atomic transitions an energy transfer of less than a given value ϵ

$$F(\epsilon) = \int_0^{\epsilon} f(\epsilon) d\epsilon$$

Using the relations

$$\begin{aligned} \left(\frac{-dE}{dx}\right)_{<\epsilon} &= \int_0^{\epsilon} \left(\frac{d^2 N}{dx d\epsilon}\right) d\epsilon \\ \left(\frac{dN}{dx}\right)_{>\epsilon} &= \int_0^{\epsilon_{max}} \left(\frac{d^2 N}{dx d\epsilon}\right) d\epsilon \end{aligned}$$

it is possible to perform a numerical computation of $(-dE/dx)_{<\epsilon}^{pl}$ in the Fermi plateau region

$$\left(\frac{dN}{dx}\right)_{>\epsilon}^{pl} = \int_0^{\epsilon_{max}} \frac{1}{\epsilon} \left[\frac{d}{d\epsilon} \left(-\frac{dE}{dx}\right)_{<\epsilon}^{pl} \right] d\epsilon \quad (2.31)$$

Using this method to simulate the energy loss by a charged particle traversing the sensitive volume of an X-ray transition radiation detector the simulation programme was developed to utilise the integral spectrums which were calculated

according to equations (2.30) and (2.31). This was done by introducing Monte Carlo simulation according to the following procedure:

- The number of primary collisions of a particle with gas atoms in a layer of path length x fluctuates according to a Poisson distribution with a mean value $\bar{N} = x(dN/dx)_{>0}$. The average number of primary collisions per cm causing ionisation and excitation of gas atoms are calculated using equations (2.30) and (2.31).
- Energy transfers of individual collisions are distributed according to the spectrum $(dN/dx)_{>\epsilon}$ using uniformly distributed pseudo random numbers which are chosen within the interval $((dN/dx)_{>\epsilon_{max}}, (dN/dx)_{>\epsilon_{min}})$, where $\epsilon_{max} = 10^2$ keV, $\epsilon_{min} = 0$ keV, and then the corresponding value of energy transfer ϵ is found.
- The energy loss Δ with the layer of path length x is the sum of N independent energy transfers.

The results of such simulation are shown in Fig. 2.17, which presents a Landau distribution of dE/dx losses together with the corresponding distribution obtained from MC simulation. The MC distribution is clearly wider than the Landau distribution and the influence of the tail in the region 4-6 keV is also more significant for MC. This is important as transition radiation is already detectable in this region. The comparison with experimental data will be presented later in this chapter.

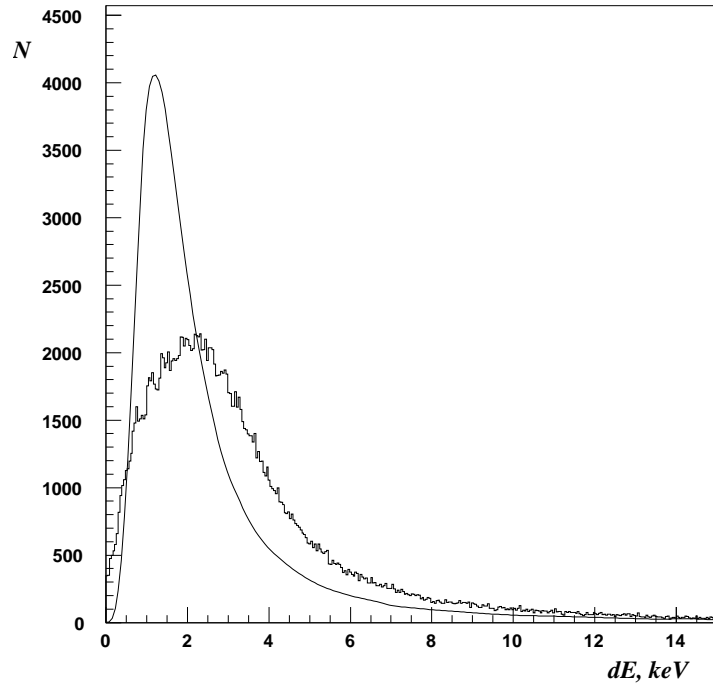


Fig. 2.17: Classical Landau distribution (smooth curve) of dE/dx losses and that obtained from MC simulation (histogram). The MC distribution is clearly wider than the Landau distribution and the influence of the tail in the region 4-6 keV is also more significant for MC

2.5 Monte Carlo Simulation of Transition Radiation for High Energy Physics

2.5.1 Simulation Programme

Based on the analysis of the practical theory of transition radiation a computer programme has been written to simulate transition radiation for relativistic particles moving through a periodic radiator. The programme has been implemented in GEANT, giving the possibility to study TRDs within the full chain of HEP experiments.

As can be seen in Fig.2.18 showing a simplified programme flow chart, there are several areas of user input in GEANT. During initialisation the user must provide a description of the geometrical setup (UGEOM), which describes the material and sensitive detectors of the experiment. The next user input involves specifying the initial kinematics of the event, from this point GEANT is able to track the primary and any secondary particles created, through the described setup (GUTRACK).

In GEANT, tracking a particle through a geometry of objects (GTVOL) requires calculating a set of points in a seven dimensional space $(x, y, z, t, p_x, p_y, p_z)$, for the trajectory of the particle. This is achieved by integrating the equations of motion over successive steps from one trajectory point to the next and applying corrections to account for the presence of matter. The step size is defined by a set of tolerances and cuts, for which GEANT contains default values, but these may also be optimised by the user. These quantities are part of the so called tracking medium parameters. They can either be calculated by GEANT or defined by the user in UGEOM.

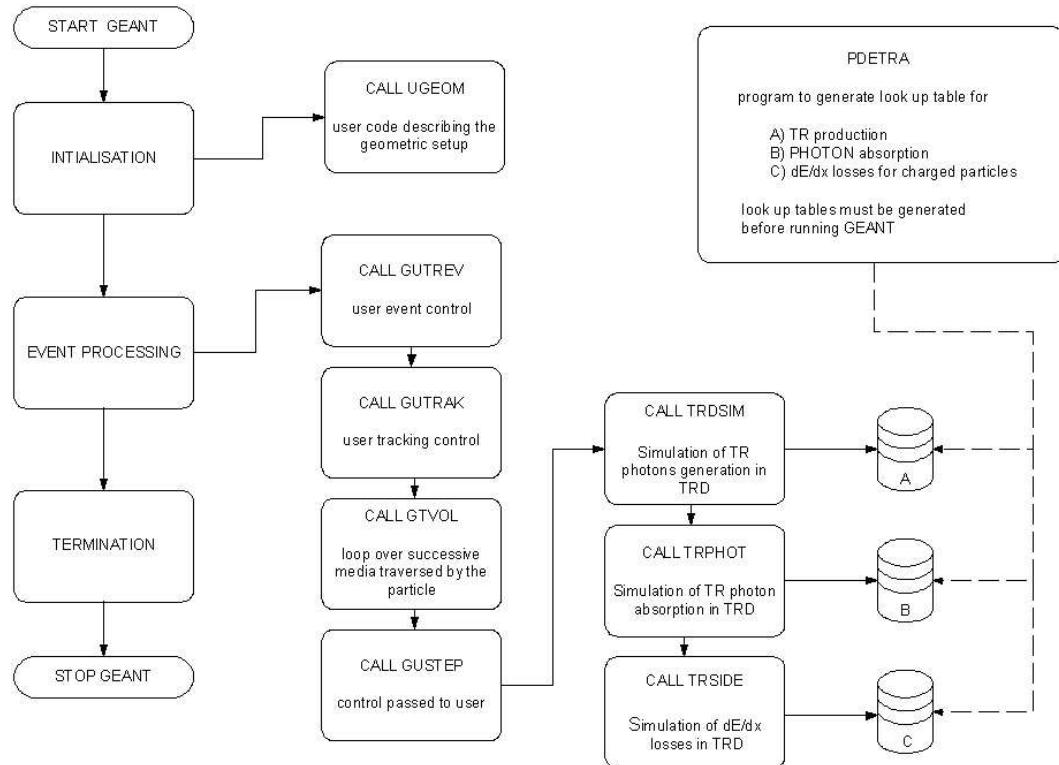


Fig. 2.18: Schematic Flow diagram showing the interaction between the different programmes needed for full simulation of transition radiation

At the end of every step the programme calls the subroutine GUSTEP. In this subroutine the user is handed control of the programme. From this subroutine the user has the possibility to access the data structures which store the current track parameters, perform calculations and call further subroutines, and then, if they so wish, alter the values of the track parameters and write them to the data structures.

It is this feature that is used to introduce a simulation of transition radiation into GEANT. Before being able to make use of this feature the following issue had to be addressed. By default the tracking energy threshold for photons in GEANT is 1 MeV, the energy of transition radiation photons is ~ 10 keV, well below the threshold. Lowering the threshold to ~ 1 keV, although possible, would lead to a detrimental effect on the performance of GEANT due to the need to track the inevitably large number of low energy photons.

To solve this problem the simulation programme uses the “geantino” feature of GEANT. The “geantino particle” is a fictitious particle included in GEANT, which maybe defined by the user. By assigning any transition radiation photons created during simulation as geantinos enables GEANT to treat them separately to other secondary particles during tracking, negating the need to lower the tracking energy threshold.

Due to the limitation of CPU power it is inefficient during the simulation of a full event to calculate “on the fly” the transition radiation emitted by a charged particle according to equation (2.18). To address this a stand alone simulation programme was written, PDETRA. Equation (2.18) is used to generate spectrums for energies across a specified interval. These spectrums are then used to produce look-up tables whose values can be interpolated to calculate the number of transition radiation photons emitted (Poisson) and their associated energy. Additionally PDETRA has been programmed to produce look-up tables

for both the photon absorption and dE/dx losses of charged particles needed for the on-line simulation programme.

The simulation uses the differential energy distribution for transition radiation photon emission from a particle with a Lorentz factor γ interacting with a transition radiation radiator. The transition radiation radiator is defined as a multi-layer stack of radiator slabs with parameters: slab thickness (l_1), slab spacing (l_2), and dielectric constants $\varepsilon_{1,2}$.

During simulation the relative position of each slab and its thickness is taken into account, in order to sum the complex electric field amplitudes correctly and reproduce interference effects.

The simulation of transition radiation radiators is composed of regularly spaced slabs, foam or fibre, this is achieved by parameterising the irregular structure in terms of n layers of average thickness (l_1), separated by an average spacing (l_2). A correction factor is introduced taken from experimental test beam measurements undertaken at DESY.

The values for the look up tables describing photo absorption are calculated using the XCOM: Photon Cross Sections Database from the NIST Standard Reference Database 8 (XGAM) (Berger et al. 1999). For the purposes of interpolation with respect to photon energy the total absorption cross section for all shells is interpolated with the use of log-log cubic spline fits, but only at energies above the K-shell absorption edge. Below this energy, interpolation is applied to the logarithm of the photoelectric absorption cross section for each separate shell, fitted as a function of the logarithm of the photon energy. The separate fitting for each shell is necessary to avoid the error that would be incurred by interpolating across absorption edges.

While the absorption of a transition radiation photon within an X-ray detector gives rise to a very localised charge cloud the ionisation from charged particles

are almost equally distributed over the active depth of the detector. However, the signal from ionisation losses is also composed of the signal from δ -electrons, which themselves create charge clusters proportional to their energy. The large width of the ionisation losses distribution observed in thin gas layers is due to the fluctuation in the number and energy of these δ -electrons. In particular, high energy δ -electrons give rise to a long tail in the ionisation loss distribution which can act as the limiting factor for the X-ray detection.

The on-line algorithm has the following features:

Transition radiation production

- The number of transition radiation photons is extracted for each event according to a Poisson distribution;
- Each photon is assigned energy according to the equation (2.21) given by the look up tables;
- Photo-absorption processes including the absorption of the transition radiation photons both by atoms in transition radiation radiator and in the gas of the detector, in both cases the ejection of electrons from both the K or L shells are described. The remaining energy appears as either Auger electrons or fluorescence photons.

Ionisation losses

- The number of primary collisions of a particle is extracted for each event according to a Poisson distribution,
- Energy transfers in individual primary collisions are distributed according to the spectrum from (Ermilova et al. 1977), given by the look up tables.
- The total energy loss within a gas layer is a sum of the independent energy transfers.

- Any secondary particles generated are placed in the STACK for further tracking by the GEANT routine GUTRACK.

Addition features of the simulation programme

- A detailed electric field map is used in order to calculate drift velocities as a function of the position in the drift chamber including the space charge effect.
- The simulation can also take into account the characteristics of front-end electronic preamplifiers, shaping amplifiers and discriminators. Electronic noise, pedestal fluctuations and digitalisation can also be included in simulation.

It is very important that the detailed simulation of transition radiation was compatible with GEANT, as this gives real estimations of the performance of the TRD in physical environments. The implementation of the simulation programme is described schematically in flow diagrams contained in the Appendix.

2.5.2 Analysis and verification of MC Simulation

In order to verify that the Monte Carlo simulation was correctly describing experimental data a comparison of the results obtained from the Monte Carlo was made with data from prototype studies undertaken by Egorytchev, Saveliev, Sosnonstev & Fourletov (1999).

The prototype studies were performed on a test beam at DESY, with the aim of testing the design aspects of a prototype transition radiation detector for the experiment HERA-B “An Experiment to Study CP Violation in the B System Using an Internal Target at the HERA Proton Ring” (Albrecht et al. 1994). The studies included an investigation into the structure of a TRD and the performance

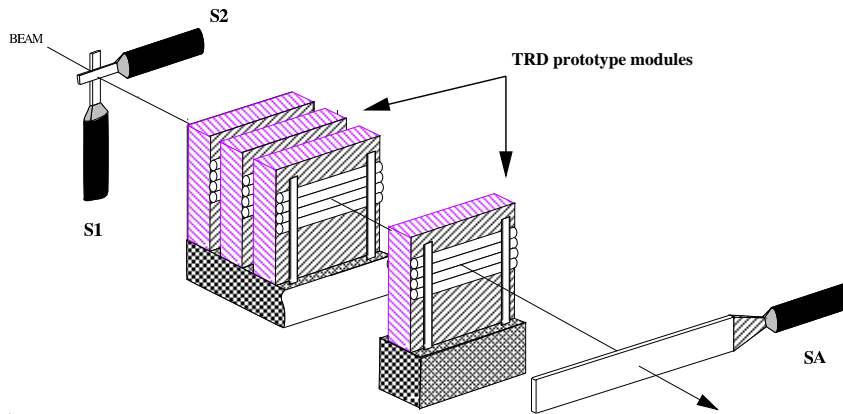
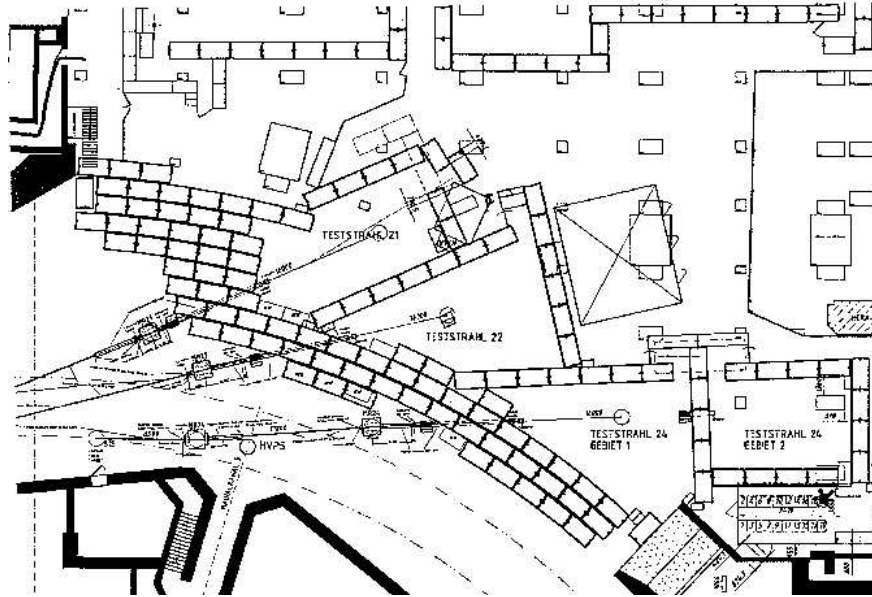


Fig. 2.19: *Experimental test-beam area at DESY (above) and the experimental setup from TRD prototype studies (below). The two overlapping scintillation counters used for coincidence triggering are labelled as **S1** and **S2**, the spectroscopic scintillation counter used for the veto is labelled as **SA**.*

of several different radiator material options using electrons delivered by the test beam at an energy of 4 GeV/c. The experimental setup is shown schematically in Fig. 2.19

The prototype TRD was based on a modern straw design structure. It consisted of 36 layers each comprising of a radiator followed by a row of 4 proportional straws tube detectors which acted as X-ray detectors. The straws were glued together and aligned horizontally and orthogonally with respect to the beam axis.

The straws were manufactured by spiralling Kapton film (25 μm) containing a conductive layer of loaded Kapton (0.2 μm Al + 4 μm C) on one side and a thermoplastic polyurethane layer (3 μm) on the other, resulting in a wall thickness of approximately 60 μm and internal diameter of 5 mm. Each straw was cut to a length of 120 mm.

During operation the straws were filled with a triple gas mixture of Xe (70%) + CF_4 (20%) + CO_2 (10%) which has proved to be stable over a broad range of anode voltages and has demonstrated a linear response to incident photons over a wide range of energies. The gas gain was maintained at 1.5×10^4 .

To enable electronic readout of the TRD the four anodes of each straw proportional straw tube layer were connected to a common preamplifier mounted on the prototype, the output signal from each of the 36 preamplifier was then transmitted via twisted pair cables to 4 channel amplifiers with shaping and discrimination. The analog output from these amplifiers were connected to an ADC for signal processing and storage.

The energy output of each straw proportional tube was calibrated using an ^{55}Fe 5.9 keV X-ray emitting radioactive source. By determining the position and width of the pulse height distributions, obtained from the absorption of 5.9 keV X-rays within the detector, it was possible to ensure that all detector layers operated at the correct gas gain as well as measure the characteristic energy resolution.

The readout trigger was assembled from a simple coincidence of two overlapping scintillation counters (S1 and S2, shown in Fig. 2.19). To prevent events with multiple particles passing through the detector i.e. electron showers, a spectroscopic scintillation counter measuring 100×300 mm (S3, also shown in Fig. 2.19) was placed behind the detector to act as a veto.

Distribution spectrums were obtained both without the presence of a radiator and with the new type of fibre radiator.

Results were obtained for the following radiator materials

- Polypropylene foam, density 70 g/l
- Polypropylene fibre, density 100 g/l

The preliminary analysis of the experimental data from the prototype studies given in (Albrecht et al. 1995), Fig. 2.20 which shows the optimisation function of transition radiation detectors, the number of transition radiation signals (straws with an energy deposit signal above the threshold value) produced by charged particles in the prototype TRD verses threshold for both the polypropylene foam radiator and the polypropylene fibre radiator. For calibration the results obtained without the presence of a radiator are also shown. The error bars shown for the experimental data in this case are due to the digitisation procedure of the threshold setup. Five energy threshold values are shown extending uniformly over the range from 4.6 keV to 8.0 keV.

For comparison Monte Carlo results are placed along side for both dE/dx losses and the transition radiation process for the traditional material used for transition radiation radiators, polypropylene foam, for energy threshold values extending uniformly over the range from 4.0 keV to 8.0 keV. MC results for 10 GeV pions are also shown though corresponding experimental data is not available due the lack of a pion source at the DESY test beam facility.

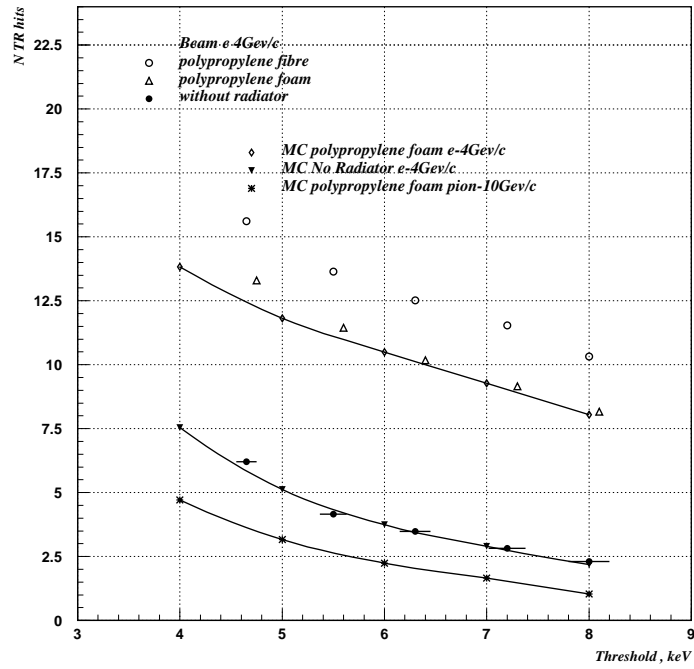


Fig. 2.20: The number of transition radiation hits vs threshold for different transition radiation radiators as measured on a test beam, and comparison with Monte Carlo predictions (solid line) (Egorychev et al. 2000).

A good agreement is observed between the experimental results and the Monte Carlo results of both dE/dx losses and the transition radiation process for the polypropylene foam.

On the other hand the experimental data from the prototype studies shows a significant increase in transition radiation output for the new type of fibre radiator $\sim 15\%$ higher in comparison with previously used radiators. It was therefore necessary to develop a new characteristic description and simulation for the new radiator material, polypropylene fibres.

In order to accurately simulate the experiment the geometry of the prototype TRD was described in the geometry of the programme including the required parameters of all materials used. The kinematics of the electron beam were also described. A MC sample was then produced to be used for comparison with the experimental data. Analysis of this MC data allowed the parameters describing the radiator to be adjusted to give results matching those obtained from the experimental data.

New code introduced to the simulation takes into account the difference between the physical processes associated with photons and charged particles for the deposit of energy in the straw proportional detectors and the performance of the electronics.

Energy spectrum distributions produced without the presence of a radiator, where only ionisation losses of the charged particle are present, were taken from the straw proportional detectors for both the experimental data and Monte Carlo data. These are shown in Fig. 2.21 the experimental data is displayed as points while the MC is displayed as a solid histogram. The MC distribution is normalised to the height of the most probable value of the experimental distribution.

A good agreement can be seen between the MC and experimental data for both the most probable energy loss at 2keV and the width of the energy loss

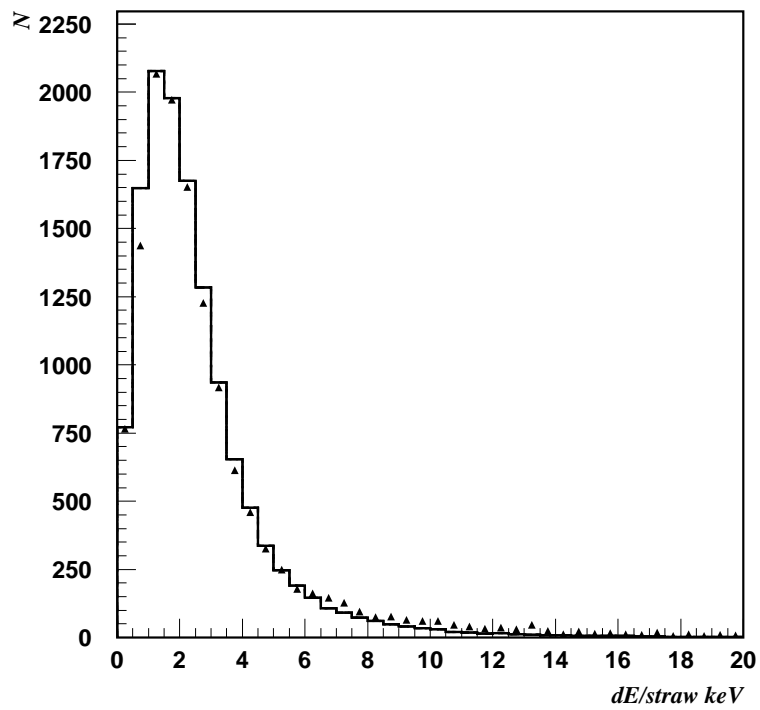


Fig. 2.21: Histograms showing Energy deposit spectrums from prototype studies without radiator. Experimental data is represented by triangular point markers and MC data is represented by the solid line.

distribution. The statistical errors in this case are negligible.

Analysis of spectrums obtained with (Fig. 2.21) and without a radiator (Fig. 2.22), shows that the inclusion of a radiator gives rise to an increase in the right tail of the energy spectrum producing a peak at 8keV, which is directly due to the absorption of transition radiation photons within the sensitive gas volume of the detector.

For a detailed comparison the error normalised difference between the MC and experimental distributions are shown in Fig. 2.23 and Fig. 2.24 over the energy range 1-20 keV. The accuracy of the MC description of the experimental spectra, both for ionisation losses and those including transition radiation is within the level of 10%.

Using the MC description of the new fibre radiator using a foil thickness (l_1) of $18\mu m$ and gap (l_2) of $200\mu m$ within the simulation programme to produce new MC calculations, it was possible to obtain the optimisation function of the transition radiation detector (the number of transition radiation signals above an energy threshold value) for the new fibre radiator over the same range of threshold values given in Fig. 2.20. These new results are shown in Fig. 2.25.

The results show an good agreement with the experimental data. In the region between 8 to 5 keV the slope increases approximately linearly, inspection of Fig. 2.22 shows that this is to be expected as the probability of energy deposit in this region is relatively constant. At threshold values below 5 keV the number of hits above threshold starts to increase more rapidly, this is again confirmed by inspection of Fig. 2.22 which shows that below 5 keV the probability of energy loss below this threshold increase dramatically. Looking back at the differential yield of transition radiation photons within Xenon shown in Fig. 2.16 it can be seen that below 5 keV due to absorption of transition radiation photons within the radiator itself the differential yield for transition radiation falls rapidly, whilst

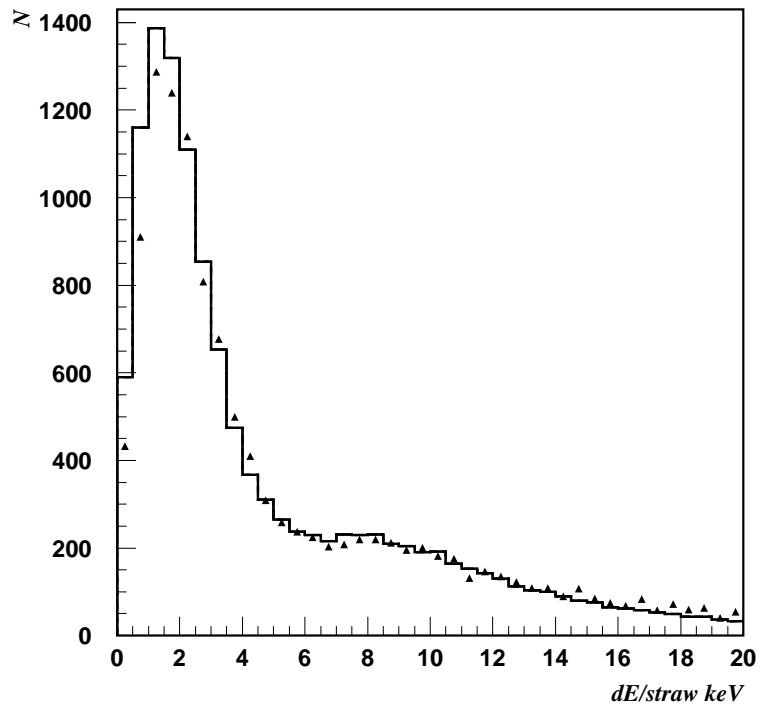


Fig. 2.22: Histograms showing Energy deposit spectrums from prototype studies with radiator. Experimental data is represented by triangular point markers and MC data is represented by the solid line.

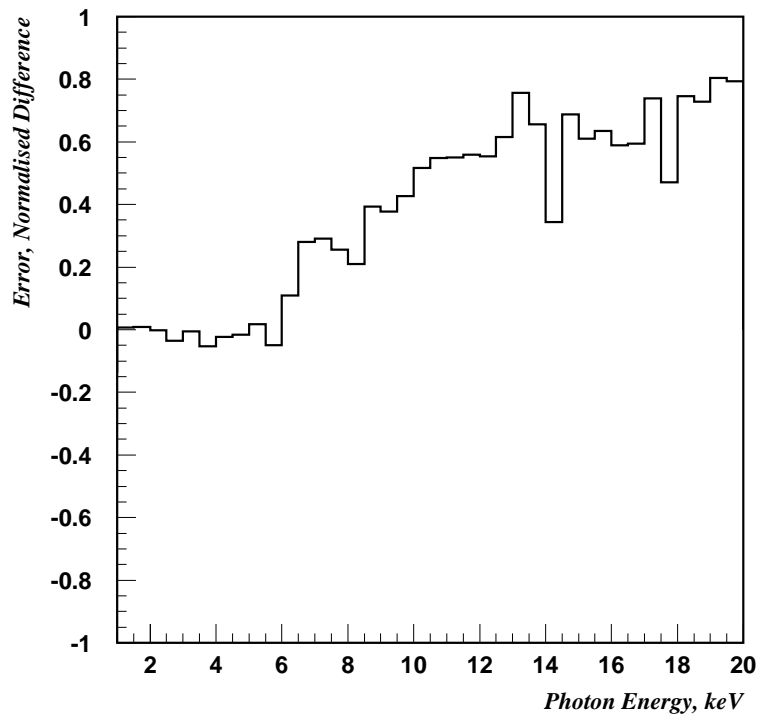


Fig. 2.23: The normalised difference between MC and experimental data for each energy bin between 1-20 keV, without radiator (ionisation losses only).

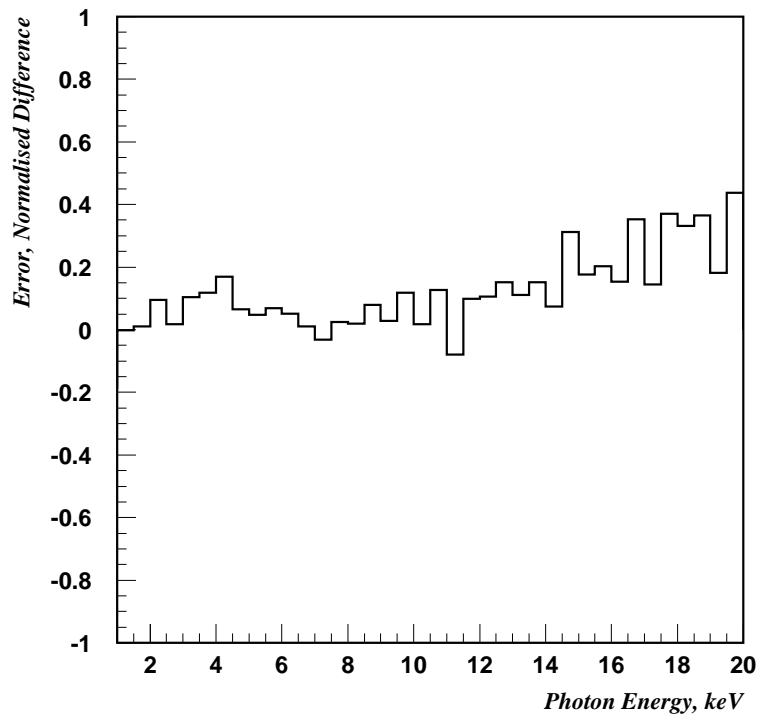


Fig. 2.24: The normalised difference between MC and experimental data for each energy bin between 1-20 keV, with radiator (including transition radiation process).

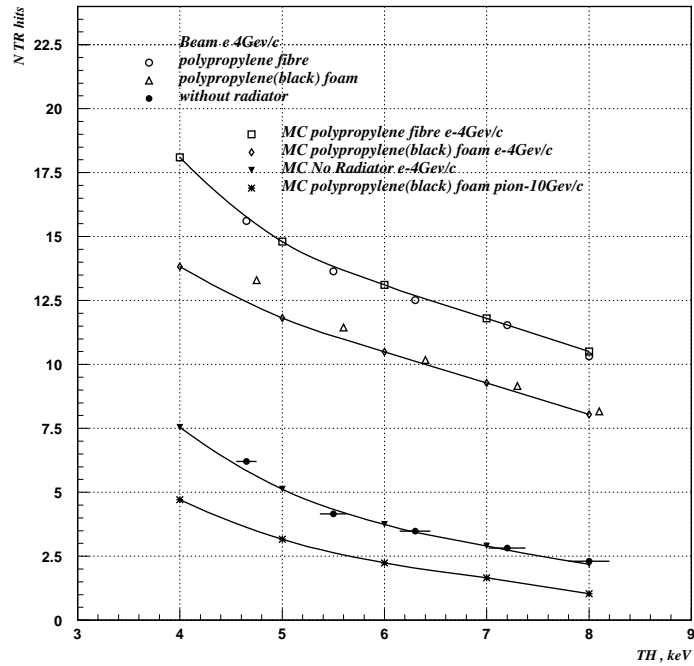


Fig. 2.25: The number of transition radiation hits vs threshold for different transition radiation radiators as measured on a test beam, and comparison with Monte Carlo predictions (solid line) including new Monte Carlo results for the new polypropylene fibre radiator.

inspection of Fig. 2.21 shows that below a threshold value of 5 keV ionisation losses by the incident charge particle will increasingly become almost entirely responsible for hits within the TRD.

The agreement between the MC description of the fibre radiator and the experimental data allows the modified MC to be used confidently for practical purposes i.e. the development and optimisation of transition radiation detectors for use in high energy physics.

Chapter 3

Analysis and Optimisation of the HERA-B TRD

3.1 Introduction

To demonstrate the practical application of the Monte Carlo simulation programme of transition radiation this chapters presents the MC analysis and optimisation of the transition radiation detector for the HERA-B experiment, “An Experiment to Study CP Violation in the B System Using an Internal Target at the HERA Proton Ring” (Abt et al. 2003a) (Abt et al. 2003b) (Abt et al. 2003c) .

The realistic geometry of the transition radiation detector elements and the simulation programme of transition radiation was installed in the common Monte Carlo framework used for simulation in the HERA-B experiment, known as ARTE (Albrecht 1996). This enable a detailed analysis of the TRD using a full and realistic description of the HERA-B experiment including physics processes.

The aim of the HERA-*B* experiment (Albrecht et al. 1994, Albrecht et al. 1995) is to identify *B*–meson decays in a dense hadronic environment, with a large geometric coverage.

The experiment was proposed in 1994 with the primary goal of measuring

CP violation in the decay channel $B^0 \rightarrow J/\psi K_s^0$ and as such the target, spectrometer and Data Acquisition System (DAQ) are optimised for its production, identification and measurement.

3.1.1 HERA Accelerator Facility

The Electron-Proton Storage Ring HERA (Hadron Electron Ring Anlage) located at DESY, was completed in 1992. It consists of two quasi-circular accelerator rings, measuring 6336m in circumference. One accelerates protons up to an energy of 920 GeV, and the other accelerates either electrons or positrons in the opposite direction up an energy of 30 GeV. See Fig. 3.2 (above).

HERA may be operated in two distinct modes; collider, where both the protons and electrons/positrons are brought into head on collision, and fixed target, where either the protons or electrons/positrons are brought into collision with the nucleus of a fixed target material placed in the beam path. In the fixed target mode using protons HERA operates at a Centre of Mass System (CMS) energy of $\sqrt{s} \approx 42$ GeV.

The HERA proton ring contains 220 RF buckets, of which nominally 180 are filled with protons. The pre-accelerators used to fill HERA with protons, PETRA and DESY III have a capacity of 60 and 10 RF buckets respectively, this leads naturally to the bunch structure shown in Fig. 3.2 (below). The last 15 RF buckets are kept empty to enable a safe beam dump. Each proton bunch contains approximately 10^{11} protons spread over a longitudinal distance, with respect to the beam, of 30cm(1 ns), and is separated from the next bunch by a 96ns bunch crossing period.

HERA has four experimental halls, one located on each of its four straight sections. The two collider experiments H1 and ZEUS are located in the north and south halls respectively. These are complimentary experiments to measure

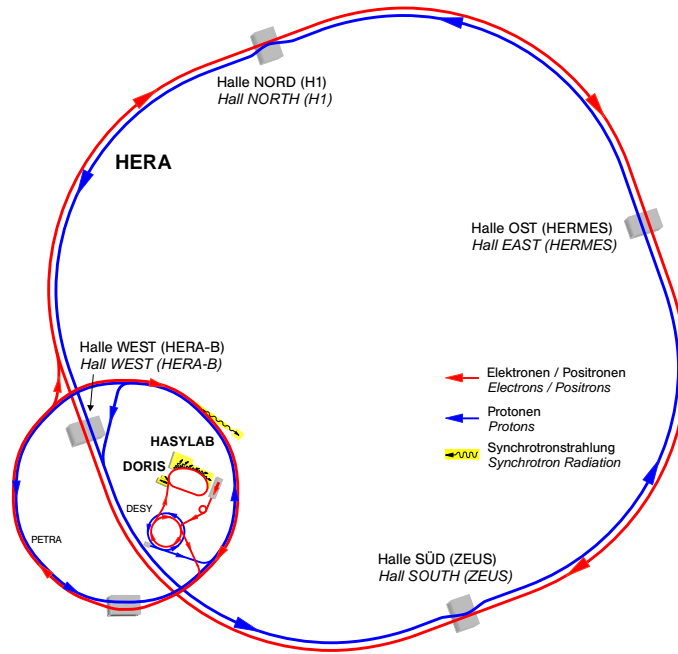


Fig. 3.1: Schematic overview of the HERA storage ring

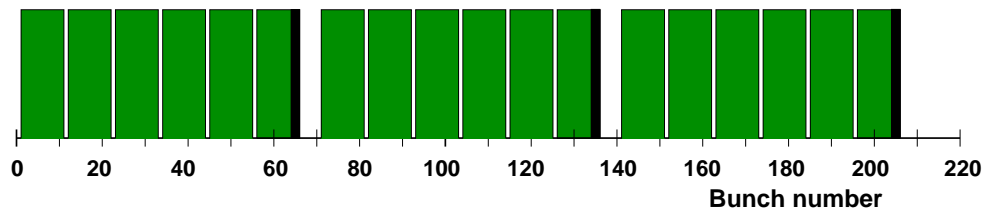


Fig. 3.2: (Schematic overview of the HERA storage ring (above)). Filling scheme of proton bunches in HERA. 180 of the 220 bunches are filled divided into three trains of 60 bunches. The bunches are separated by 96 ns (below).

deep inelastic scattering. HERMES situated in the east hall uses the polarised electron/positron beam impinged on a polarised gas target to measure the spin structure of nucleons. HERA-*B* is located in HERA's west hall.

3.1.2 The HERA-*B* detector

The HERA-*B* detector is a large-aperture high-rate spectrometer with a geometric coverage from 15 mrad to 220 mrad in the bending plane of the magnet and from 15 mrad to 160 mrad in the vertical plane. The full spectrometer measures $\sim 20m$ in length. A schematic overview is shown in Fig. 3.3. The following section will discuss the requirements and design of the different experimental components.

Target System

The desired decay $B^0 \rightarrow J/\psi K_s^0$ has an extremely low signal to background ratio $\sim 10^{-11}$. This presents the need for a high luminosity B source, i.e. a *B*-factory producing at least of the order of 10 *B*'s per second (Ehret 2000). To achieve the required interaction rate of 40 MHz an internal target consisting of eight thin wires operating in the beam halo at typical distances of around five beam standard deviations.

The wires operate in the beam halo so as to take advantage of protons which have left the beam core and would naturally be lost on aperture limitations, such as collimators. This enables HERA-*B* to operate in parallel to the other HERA experiments with a limited impact on the lifetime of the beam. The Target system uses eight wires so that the primary interactions in a single bunch crossing are separated with

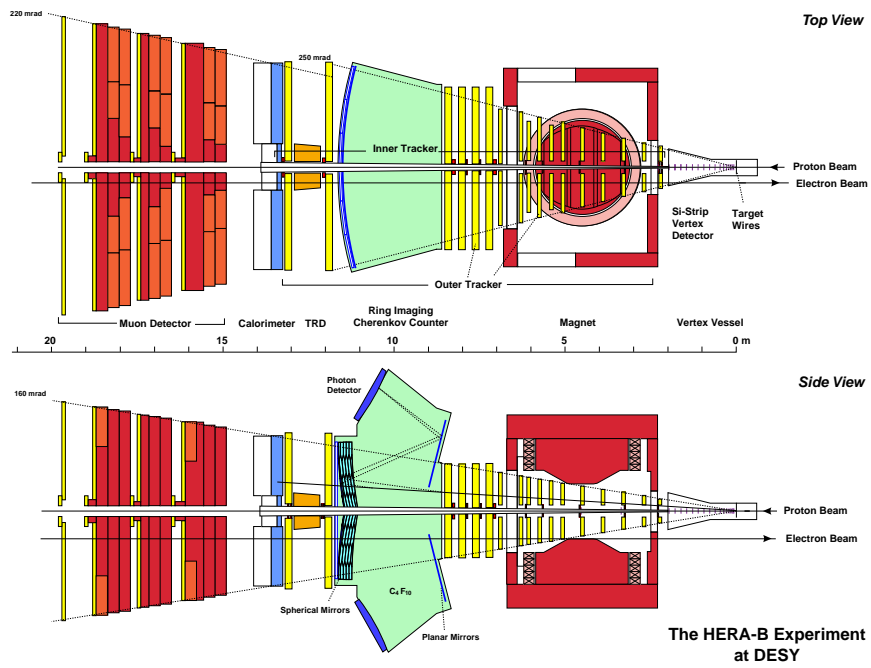


Fig. 3.3: Schematic overview of the HERA-B spectrometer

well localised main vertices on different wires, this is a fundamental requirement to ensure precise reconstruction of multiple interactions.

The eight wires are arranged into two stations of four separated by a relative distance of 4cm in z and positioned around the beam axis as shown in Fig. 3.4. Each wire is independently steered by an integrated servo system. Target steering is based on directly measured rates and a simple algorithm.

At present the Target system includes wires of Aluminium, Carbon, Palladium, Titanium and Tungsten, yielding an atomic mass range of 12 to 184. The choice of the optimum target material is subject to several considerations. Primarily as the production of $b\bar{b}$ events relative to inelastic scattering should be as great as possible, since b production approximately scales with the mass number A , and inelastic interaction with $A^{0.72}$, this favours heavy nuclei, such as Titanium $A = 47.9$. At the same time, however, the mean number of tracks per interaction also increase with $A^{0.2}$, which decreases signal to noise ratio. Also of consideration is that while passing through the target wire the proton is subject to multiple scattering which is the main source of inefficient proton loss and increased background, this of course favours light nuclei, such as Carbon $A = 12$.

The simultaneous use of different target materials gives HERA- B the added opportunity to perform measurements of the A dependence of various cross sections with small systematic uncertainties.

Vertex Detector System

The Vertex Detectors System (VDS) of the HERA- B spectrometer provides the necessary data for precise reconstruction of both, primary vertices produced at the target and secondary decay vertices of particles with lifetimes $\tau > 10^{-12}$ s. The data obtained also contributes to the algorithm of the second level trigger. The VDS covers an acceptance region of 10 - 250 mrad vertically and horizontally.

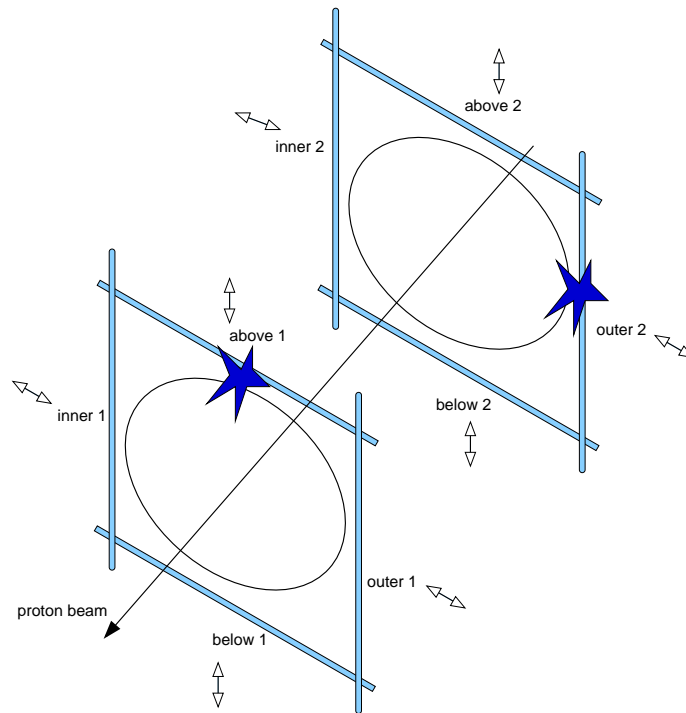


Fig. 3.4: The target system consists of eight wire arranged into two stations. Each wire is independently steered by an integrated servo system. To increase the interaction rate the wires are moved further into the beam halo, to reduce the interaction rate the wire are moved out

It uses double sided silicon strip detectors which are mounted in planes perpendicular to the beam axis. The detectors are arranged in eight super layers of four quadrants. Each quadrant of a super layer contains two silicon micro strip detectors making a total of 64 independent detectors, this can be seen in Fig. 3.5. Each detector has an active area of $50 \times 70\text{mm}^2$, the n-side has the strips aligned at an angle of 92.5° with respect to vertical and the p-side has the strips aligned at 2.5° with respect to vertical, giving a stereo angle of 5° in both the horizontal and vertical planes when two detectors are mounted back to back. This gives equal precision for the track reconstruction in both the vertical and horizontal planes. A read out pitch of $50\mu\text{m}$ ensures that the average hit occupancy remains below 5%.

The impact parameter resolution is $35\mu\text{m}$ for high momentum particles ($p > 50 \text{ GeV}/c$), while the resolution of primary vertices is approximately $500\mu\text{m}$ in z and $40\mu\text{m}$ in x and y .

Main Tracking System

With the large particle densities generated in the experimental environment of HERA-*B* and the large angular acceptance demanded by the physics goals the reconstruction of charged tracks throughout the spectrometer is of vital importance, this is covered by the main tracking system.

The main tracking system is divided into a fine grained Inner Tracker System (ITR) close to the beam $\sim 0.06\text{-}0.30\text{m}$, and a large area Outer Tracker System (OTR) at larger distances from the beam. With the strong increase in particle flux with decreasing distance from the beam this arrangement provides the necessary granularity needed to keep the occupancy level at a manageable level.

The tracking system is divided into three sections. The first section, Magnet Chambers (MC1-8, MS1-7), is made of chambers placed within the magnet of the

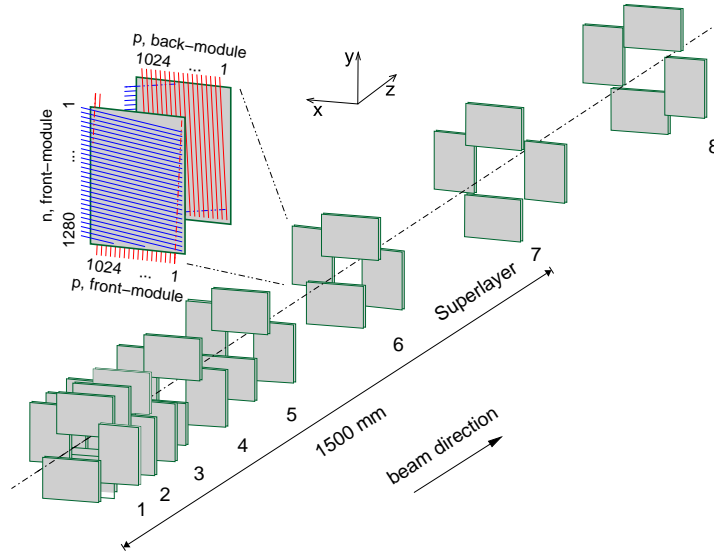


Fig. 3.5: Schematic diagram of the VDS layout. The VDS consists of eight superlayer. Each super layer consists of eight single or double sided silicon micro-strip detectors.

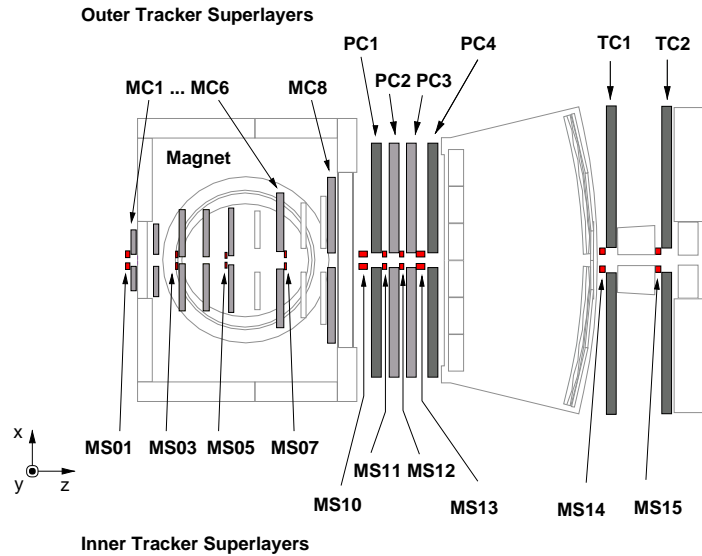


Fig. 3.6: Overview of the main tracking system of the HERA-B spectrometer. The superlayers of both the ITR and OTR are shown in their three distinct groupings. The outermost regions of the angular coverage are covered by the OTR and the innermost regions by the ITR.

spectrometer, these are responsible for providing track space points within the magnetic field to enable efficient reconstruction of K_s^0 decays. In addition these chambers facilitate the extrapolation to the VDS of track segment reconstructed in the PC chambers. The second section, Pattern Recognition Chambers (PC1-4,MS10-13), is situated between the back of the magnet structure and the front of the RICH vessel, due to their large coverage and absence of magnetic field these chambers provide the main area for the search of charged tracks. Finally the third section, Tracking Chambers (TC1-2,MS14-15), is located between the back of the RICH vessel and front of the Electromagnetic Calorimeter, these chambers provide the trigger signal needed for the First Level Trigger track search.

In total the tracking system consists of 13 superlayers as shown in Fig. 3.6. Each superlayer is made up of several layers of ITR and OTR modules, with different anode orientations 0mrad , $+80\text{mrad}$, -80mrad with respect to the y -axis.

The ITR uses micro-strip gas chambers in conjunction with gas electron multipliers. The strip pitch is $300\mu\text{m}$ which provides a spatial resolution of $80\mu\text{m}$.

The OTR is constructed from honeycomb drift chambers with wire pitches of 5mm for the regions closest to the beam, and 10mm for the outer regions. The largest superlayers extend up to 3m from the beam axis.

ECAL

The Electromagnetic Calorimeter (ECAL) performs the task of electron identification within the HERA- B spectrometer over the energy range 5-150 GeV and is able to measure the energy of photons from 5 GeV up to 200 GeV.

The ECAL is situated after the last superlayer of the main tracking system, 13.5m (z -axis) from the target. It is constructed using a “shaslick” design which sandwiches tiles of absorber between active layers of scintillating material. The

electron photon showers created by incoming particles are collected by wavelength shifting fibres and guided to photo-multipliers located behind the wall of active modules.

The front wall of the ECAL measures $6.24 \times 4.69\text{m}^2$ which covers the full acceptance of the spectrometer. It is subdivided into three parts to allow for the radial dependence of the particle flux, see Fig. 3.7. The inner most region is equipped with cells whose front wall measures 0.0224m^2 , for this region tungsten is used as the absorber material. The middle and outer regions have a front wall of 0.056m^2 and 0.112m^2 respectively here, due to the high cost of tungsten, lead is preferred as the absorber material.

RICH

The Ring Imaging Cherenkov (RICH) counter is responsible for particle identification, primarily the separation of kaons and pions. It is located between the PC and TC superlayers of the OTR, in front of the ECAL. Cherenkov light emitted in the 2.5m long C_4F_{10} radiator volume is projected by focal and planar mirrors as a ring image onto the plane of photo multipliers. The projected ring provides information on the velocity of the particle, which can be used in conjunction with information on its momentum to calculate its mass, through which the particle may be identified.

MUON System

The MUON system provides tracking and identification of muons whose momentum is greater than 4.5 GeV. It consists of four superlayers sandwiched between iron loaded concrete absorbers, this is shown in Fig. 3.8. To address the issue of the radially varying occupancy two different technologies are employed.

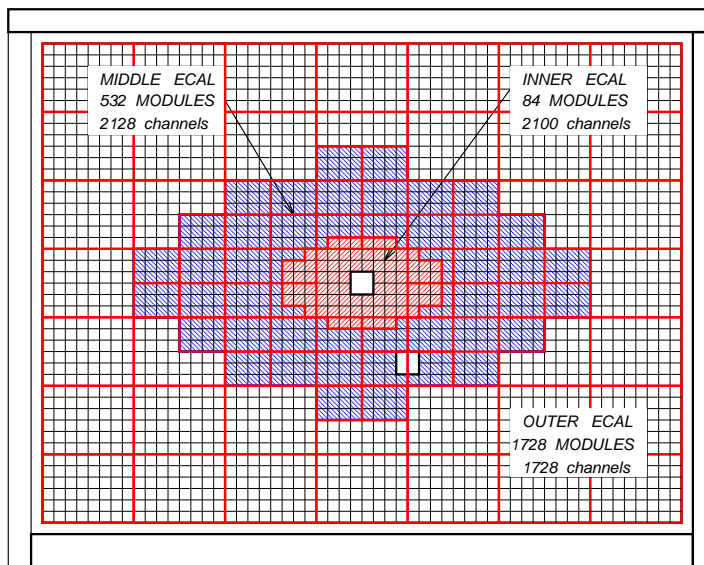


Fig. 3.7: The layout and segmentation of the ECAL. The three regions of different cell size are shown for the Inner, Middle and Outer ECAL

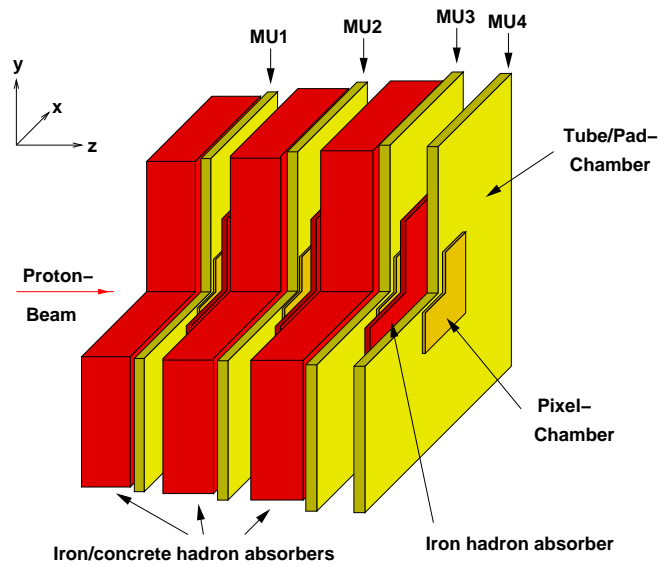


Fig. 3.8: *The MUON system consists of three iron loaded concrete hadron absorber and four superlayers In the region of higher occupancy close to the beam gas pixel chambers are used, while the outer lying region is covered by tube chambers equipped with both wire and pad readout.*

In the region of higher occupancy close to the beam gas pixel chambers are used, while the outer lying region is covered by tube chambers equipped with both wire and pad readout.

Trigger System

The high interaction rate and extreme signal to background ratio of 10^{-11} presents a unique challenge to the HERA-B experiment. To overcome this a multi-level trigger system is employed. The spectrometer has approximately 500k channels which need to be read out for every bunch crossing, at a bunch crossing rate of 10MHz these produce some 5 TBytes of data per second. Due to limitations on the rate at which events can be stored this must be reduce to an event output rate of 50Hz, at which the data can be written to tape.

The trigger system is specifically designed to select events containing a J/ψ decaying to $\mu^+\mu^-$ or e^+e^- . The overwhelming majority of these J/ψ events will not be the result of a B decay. Nevertheless even directly produced J/ψ events are sufficiently rare to bring about the desired rate reduction of $\sim 10^6$. Due to the difficulty of qualifying the events within the 96ns bunch crossing time window, this is achieved using a trigger chain that consists of four levels and a buffer system. Fig. 3.9 shows a schematic diagram of the trigger system levels and there associated rate reduction and decision times.

The First Level Trigger (FLT) consist of custom made hardware processor boards that performs track reconstruction using information from the TC and PC tracking chambers. This track reconstruction is initiated by an energetic cluster in the ECAL or a coincidence of hits in the MUON system, both of which give a first estimate of the track parameters. After determining the momenta of these tracks a mass reconstruction is performed using pairs of tracks. Once the event is accepted all event data is sent to the Second Level Buffer (SLB).

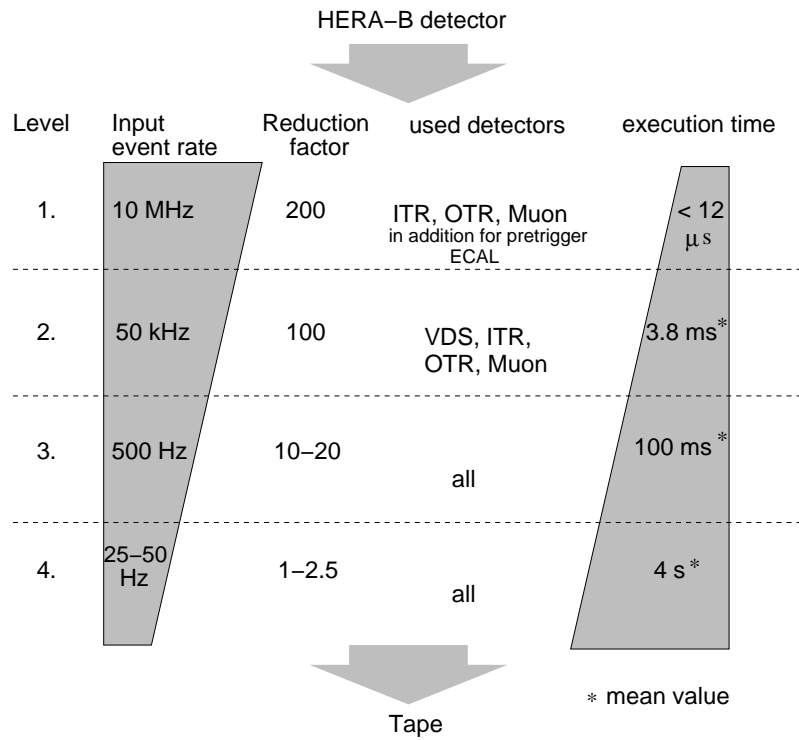


Fig. 3.9: Overview of the different trigger levels and their associated rate reduction and decision times

The Second Level Trigger (SLT) takes tracks which have been accepted and passed to it by the FLT (via SLB). The SLT is made up of a farm of 240 PCs which process events, improving the accuracy of the track fit using the measured drift times from the OTR. The tracks are then traced back through the magnet and the vertex system in order to find if the pairs of tracks originate from a common vertex. If the event satisfies the requirements needed to pass the SLT tests then the PC which has performed the SLT decision will assemble the full event from the SLB and then run the Third Level Trigger (TLT) algorithm performing track and vertex fitting of tracks within the vertex system.

After the SLT/TLT the event rate is sufficiently reduced to allow a full event reconstruction to be performed on a second farm of PCs this known as the Fourth Level Trigger/FARM. The FARM is also used for running online processes during data taking such as alignment, calibration and automated data quality monitoring.

3.2 HERA-B TRD

The HERA-B TRD was proposed as a part of the Electron Identification System to cover the central part of the spectrometer, in front of the Electromagnetic Calorimeter where high occupancies are present, which degrade the performance of the ECAL so that it is unable to guarantee the required π/e misidentification of at most 1% over the full momentum range from about 5 GeV up to 150 GeV. The preliminary design is given in the Technical Design Report of the HERA-B experiment (Albrecht et al. 1995).

The HERA-B TRD is based on a modern straw design sandwich structure (Saveliev 1998). These structures are known as 'fine sampling TRDs' and consist of periodic structures of thin transition radiation radiators and X-ray detector planes, which provide frequent measurement of transition radiation photons and

increases the statistical significance of measurements. This structure already suggests the possibility of continuous tracking where the large number of detection planes is used to provide many precision space points for track reconstruction.

The TRD is positioned in the central part of the HERA-B spectrometer between the two Tracker Planes TC01 and TC01. The inner boundary of the TRD is determined by the size of the beam pipe. The outer dimensions are defined by the inner part of the ECAL which has an acceptance of 45% and the highest occupancy.

The total length which is available for the TRD along the particle beam is ~ 74 cm. The total quantity of material along the trajectory in the TRD must be less than 0.1 of a radiation length.

The role of the X-ray detector is fulfilled by straw proportional tubes, produced from kapton foil, filled with an optimal triple gas mixture of $Xe-70\%$, $CF_4-20\%$, $CO_2-10\%$ which has a gas gain of 2.5×10^4 and total electron drift time of about 20 ns.

3.2.1 Analysis and Optimisation of the HERA-B TRD

To reach a final design for the HERA-B TRD a detailed MC simulation was performed using the simulation programme of transition radiation within the MC framework of the HERA-B experiment (ARTE).

The description of the TRD geometry in ARTE uses a modular scheme. The basic elements are the radiator and the straw proportional chambers. A TRD module, is composed of straw planes within a homogeneous block of radiator material. While the various TRD modules may have different geometric shape and number of straws they all follow this basic structure. The geometry is described in ASCII format and is accessed by ARTE when it invokes HBGEAN.

Using the DTREE facility in HBGEAN it is possible to retrieve the GEANT

structure of the TRD this is shown in Fig. 3.10. In this schematic view TR01 and TR02 denote the two super-layers, TRB the TRD modules, TRTU the straw proportional chambers. Volumes starting with TS denote the support structure needed to hold the TRD in position. Such a structure gives a large number of possible arrangements for systematic optimisation of the elements without the need for dramatic changes in the overall structure. An example of a full MC event within the HERA-B experiment is shown in Fig. 3.11

Fig. 3.12 shows the orientation of both super-layers to one another when placed in situ. Finally Fig. 3.13 shows the TRD in position in front of the Tracker Plane TC02, also visible are the two beam pipes, the larger passing directly through the TRD being the HERA proton beam and the other smaller one is the HERA positron beam. All other Sub systems have been removed to give a clear view. Both figures have been generated using the GEOM and DRAW packages of HBGEAN(GEANT).

It has already been mentioned that for the general case a critical parameter of a TRD is the length along the direction of interaction, for HERA-B this was fixed at a maximum of 74 cm.

In this case the main aspects of the MC simulation and optimisation study were

- Thickness of the transition radiation radiator which defines the overall length of the radiator and hence its efficiency, - 1.0 – 2.5 cm.
- Material used as transition radiation radiator, - polypropylene foam or polypropylene fibres.
- transition radiation detector (straw) diameter, - 4 – 8 mm.
- Threshold value of transition radiation signal, - 4 – 8 keV.
- Overall geometry of the TRD, - for optimum efficiency and rejection factor.

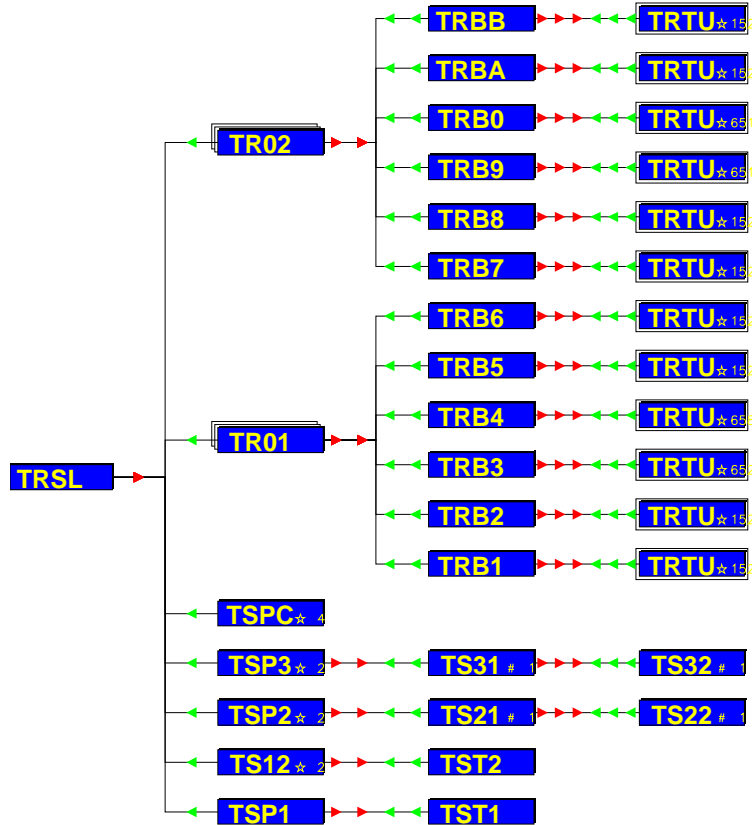


Fig. 3.10: Schematic view of the geometric implementation in GEANT of the HERA-B TRD. KEY: TRSL = overall GEANT Volume, TR01-2 = TRD superlayers, TRB* = TRD module (straws embedded in radiator material), TRTU = straw tube proportional chambers

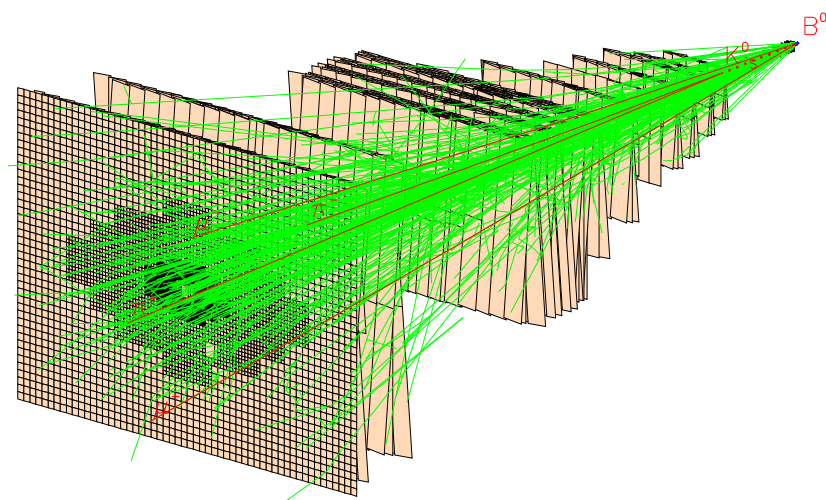


Fig. 3.11: A full MC event in the HERA-B spectrometer

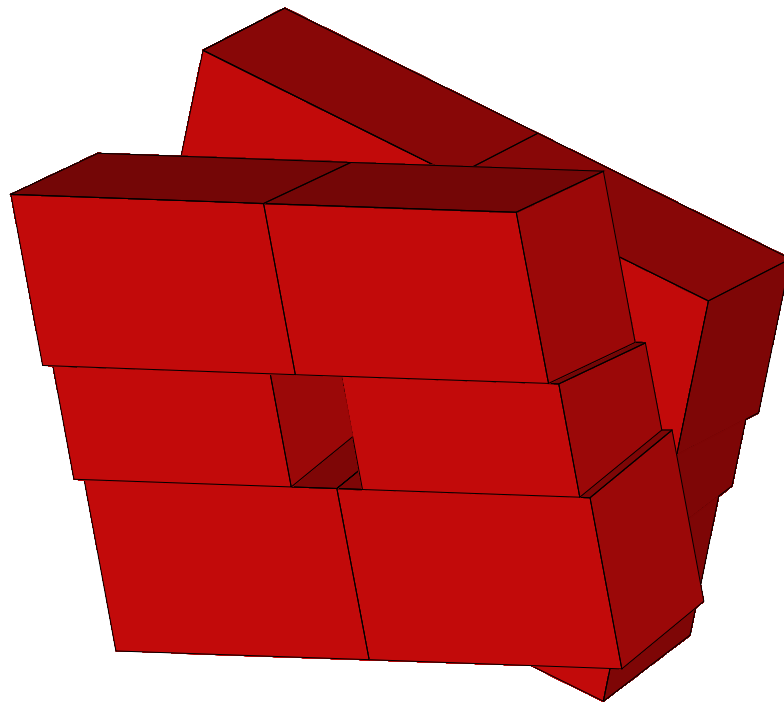


Fig. 3.12: *Shown are both Super-layers TR01 and TR02 and their orientation to one another*

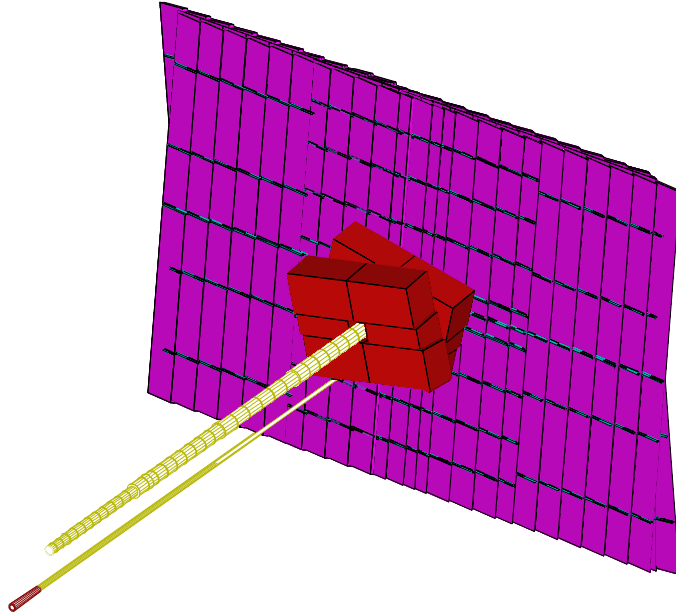


Fig. 3.13: *TRD in front of OTR Super-layer TC02, all other Sub systems have been removed to give a clear view*

The main goal is the optimisation of the rejection factor, which is given as

$$R = \frac{\eta_1}{\eta_2} \quad (3.1)$$

The final results obtained from simulating the performance of the TRD for HERA-B using the full GEANT description of the HERA-B detector are shown in Fig. 3.14 and Fig. 3.15. The distribution of total energy loss in straw proportional tubes for electrons and pions with energy 30 GeV/c is shown. The case where additional energy from transition radiation photons is deposited together with the ionisation losses from the incident particle produces the peak at $\sim 9\text{keV}$ in the energy spectrum for electrons (Fig. 3.14 top right). This excess increases the number of hits above a given threshold and can be seen in Fig. 3.14 bottom right, shows the distributions of the transition radiation photon hits for a threshold value of 5.5 keV. In contrast it can be seen that for pions the distribution of total energy loss is representative of that expected for ionisation losses of the incident particle only.

These studies led to the final design of the HERA-B TRD which consists of two super-layers at a stereo angle of $\pm 30^\circ$, each having a modular structure. The modules have been produced based on a Carbon Composite honeycomb core sandwich Structure (CCS) which provides the necessary mechanical stability. The optimum number of layers was chosen as 32 with a polypropylene fibre radiator of thickness 1.7 cm and a straw diameter of 6 mm. The position of the straws within the modules ensures a uniform distribution of the number of straws traversed by a charged particle. This design gives ~ 10000 electronic readout channels for which the threshold value was set at 5.5 keV. The readout of these electronic channels is provided by the ASDBLR (Amplifier Shaper Discriminator with Base Line Restoration) based front-end electronics.

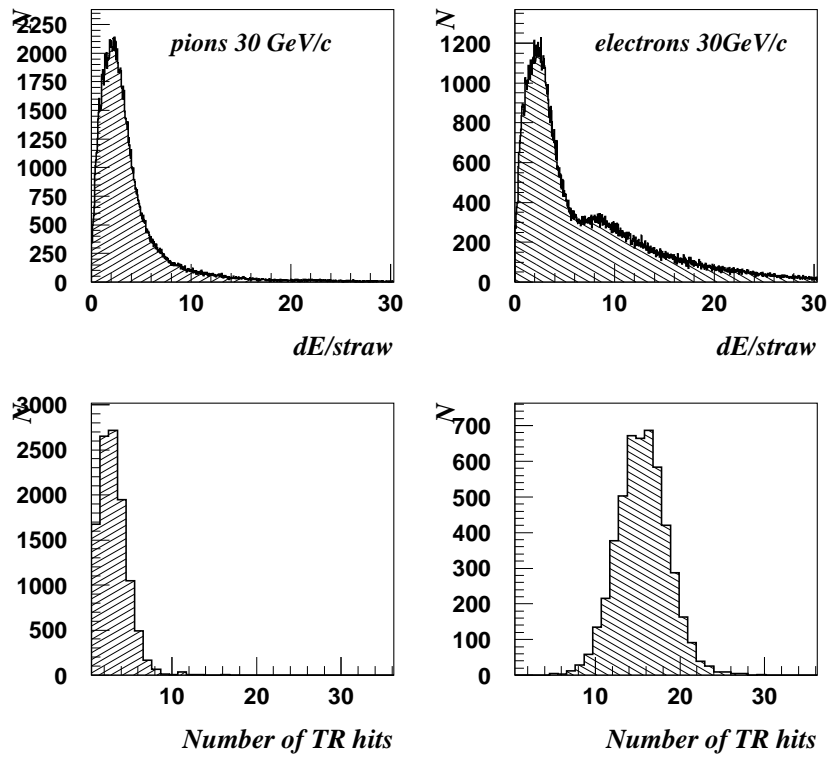


Fig. 3.14: Histograms showing the energy distribution for Straw tubes (top) and transition radiation hits distribution (bottom) for electrons and pions 30 GeV/c.

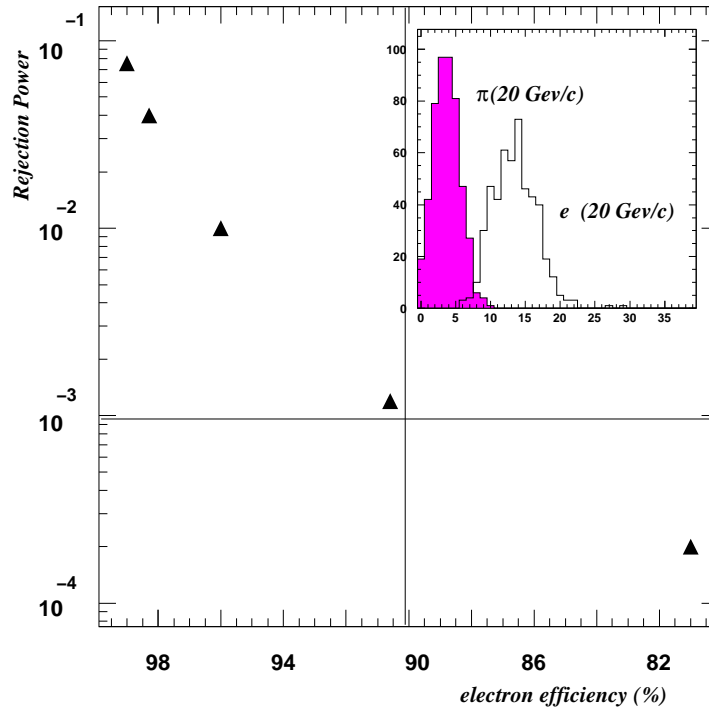


Fig. 3.15: MC calculation of the Rejection Power vs electron efficiency for the HERA-B TRD

The analysis of the full simulation of the physics processes in the ARTE frame work led to the calculation of the rejection power of the HERA-B TRD as a function of the electron efficiency, this is shown in Fig. 3.15, the rejection factor was found to be $\sim 10^2$ for electrons and pions in the momentum range 10 – 50 GeV at an electron efficiency of $\sim 95\%$.

As the HERA-B TRD was not fully commissioned within the HERA-B spectrometer during the experimental running periods from 1999 to 2003 it was not possible to estimate the rejection factor using experimental data, for this reason no comparison is given.

Chapter 4

Proposal of a TRD for TESLA

4.1 Introduction

Another application of the simulation programme for transition radiation is the analysis and optimisation undertaken in the development of a new concept transition radiation detector proposed for the future linear collider experiment at, TESLA “The Superconducting Electron-Positron Linear Collider”. The main aspects of the analysis were presented in (Chamanina, Dolgoshein, Egorytchev, Fourletov, Kaoukher, Saveliev, Aplin & Franklin 2001). In which the proposal was given for the new concept of transition radiation detector based on using a high magnetic field to provide separation between transition radiation photons and the track of the incident charged particles.

Generally particle identification is a crucial aspect of all high energy experiments and its significance increases with the energy of the physical processes of the experiment. An example of this is the detection of electrons in jets, for instance, the tagging of b -jets using relatively soft ($p = 5$ to 40 GeV/ c) electrons.

A considerable amount of “new physics” signals consist of b -jets ($h^0 \rightarrow b\bar{b}$, top decays etc.), therefore their selection is extremely important. The most powerful way to tag b -jets will be to look for displaced vertices. However the tagging of

soft electrons inside the b -jet will provide a valuable complement to this, giving the additional possibility to separate b -jets from u, d, s, c and gluon jets (using electron's transverse momentum relative to the jet axis. In addition the e^+ or e^- tagging of b and c jets allows the measure of vertex charge (b, c separation from \bar{b}, \bar{c})

Soft electron b -jet tagging requires good electron identification inside the hadron jet and will be difficult to achieve using information from the calorimeter alone.

4.2 Physics of the TESLA Project

The Standard Model is the culmination of the progress made in particle physics over the past thirty years. However such a theory of matter particles and force fields suffers from a serious deficiency. The underlying gauge principle requires at first sight all field quanta to be mass-less. This is in striking contrast to the large masses of the W and Z bosons, which are 80-90 times heavier than the proton. At present the only compelling way to give particles a mass while preserving the gauge principle is the so called Higgs mechanism. The basic idea is that the a priori mass-less particles acquire “effective masses” by interaction with a background medium, know as the Higgs field. The idea of mass generation by the Higgs mechanism leads to a Higgs field which spreads out in all space. Although the Higgs mechanism was first put forward over 20 years ago, despite major efforts to verify it experimentally, the Higgs particle has to date escaped observation.

Therefore, one of the most pressing challenges of particle physics is to establish the Higgs mechanism, discover the Higgs particle and to study its properties or to find a valid alternative explanation for the existence of massive particles.

The verification of the Higgs mechanism via the discovery of the Higgs particle, however, is not the only major topic which can be addressed. General arguments

clearly point to the existence of an even more fundamental theory. The theory of Supersymmetry (SUSY) is widely favoured as the idea which could provide an extension of the Standard Model. In supersymmetry theories, for every fundamental particle we know of today, there exists a related and yet undiscovered particle, the lightest of which is thought to be stable. Supersymmetry also predicts several Higgs particles, the lightest of which should have a mass below 200 GeV, or even below 135 GeV in some specific models.

4.3 Linear electron-positron collider at an energy of 500 GeV to 1 TeV

The two large accelerators in operation at present are the electron-proton collider HERA and the proton-antiproton collider Tevatron at Fermilab near Chicago. The next major accelerator project in particle physics is the large proton-proton collider (LHC) being built at CERN which is scheduled for completion in 2006.

However, previous experience shows that a proton collider alone is not sufficient to adequately explore the subatomic world, it is best complemented by a high energy collider for electrons and positrons. An example of this is the heavy Z boson, which was discovered at an proton-antiproton collider, while its detailed properties have only been measured with high precision at electron-positron colliders.

For this and other reasons there is broad agreement in the HEP community that a linear electron-positron collider with an initial centre of mass energy of $E_{cm} = 350 - 500$ GeV and a luminosity above $10^{33}\text{cm}^{-2}\text{s}^{-1}$ is of fundamental importance for the future development of particle physics (*Understanding Matter, Energy, Space and Time: the Case for the Linear Collider* 2003).

Such a proposal has been put forward by the joint DESY ECFA study for

a future linear collider (*Conceptual Design of a 500 GeV e^+e^- Linear Collider with Integrated X-ray Laser Facility* 1997). The proposal describes a tera electron volt superconducting linear accelerator. The baseline design for TESLA is a 500 GeV electron-positron linear collider measuring 33km in length with one or two interaction regions at 16.5km. The electromagnetic radio-frequency resonators (cavities) will use superconducting technology, this has been made possible by the recent reduction in the cost per meter of accelerator for superconducting technology. This will allow for achievement of the high beam power and very small spot size needed to deliver the desired luminosity.

4.3.1 TESLA Spectrometer

A spectrometer for the TESLA linear collider, shown in Fig. 4.1, will be required to cover a large dynamic range in particle energy, complexity of final states and signal to background ratio. The average jet multiplicity in hadronic events doubles from $\sqrt{s} \sim 100$ to 1000 GeV because of the increasing cross section for multiple gauge boson production and harder gluon radiation; $t\bar{t}H$ or charged Higgs boson pair production will result in multi (8 or more) parton final states. The track density in collimated jets will reach the level of as much as one per mm^2 at a radius of 1.5cm, while the accelerator induced backgrounds will produce typical hit densities of the order of 0.03/ mm^2 down to 0.001/ mm^2 per bunch crossing at radii of 1.5cm and 30.0cm respectively. The diversity of physics signatures anticipated at TESLA and the characteristics of the bunch timing suggest a data acquisition scheme with continual read out having no trigger and no dead time for maximum data logging efficiency.

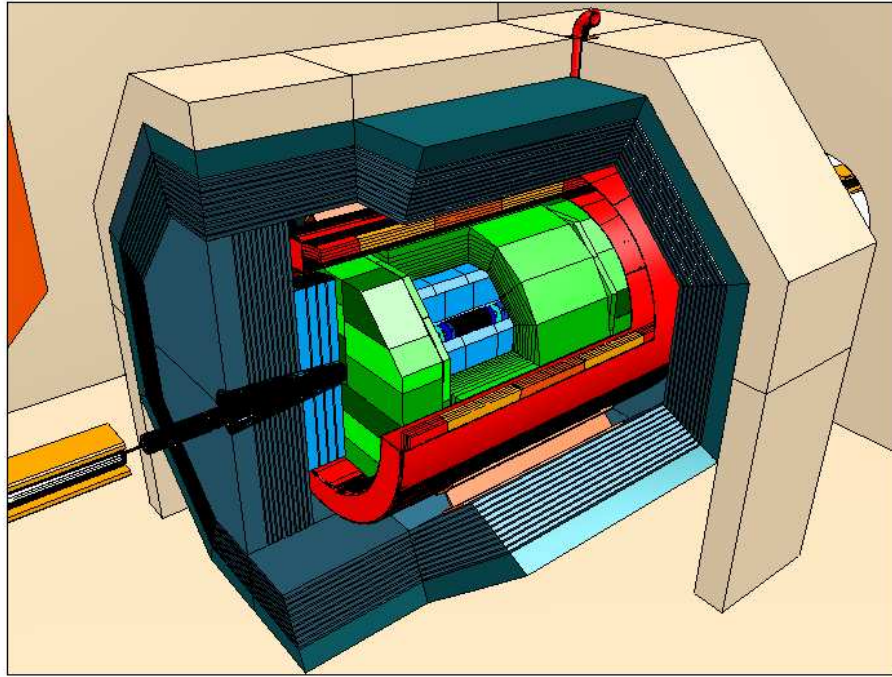


Fig. 4.1: Schematic view of the TESLA spectrometer, the near sides of each detector have been cut away to allow the detectors at different depths to be seen

The four main detector aspects that pose the greatest challenge to the realisation of a competitive detector are; track momentum resolution, jet flavour tagging, energy flow, and hermeticity. These must all reach higher levels of performance better than those already achieved at the Large Electron Positron collider (LEP) or Stanford Linear Collider (SLC).

Track Momentum Resolution

The analysis of the di-lepton mass in the process $HZ \rightarrow Hl^+l^-$ provides a means to analyse the Higgs production independent of its decay properties via the recoil mass to the di-lepton system. Making the requirement that both the measurement error on $M_{l^+l^-}$ and the mass recoiling to the l^+l^- system, be small reduces the combinatorial background significantly. This places a strict requirement on the momentum resolution.

Vertexing

The potential for investigating electroweak symmetry breaking must be met by a detailed study of the decay properties of the Higgs to complement the aforementioned production studies. Distinguishing between a light Higgs boson decaying into $b\bar{b}$, $c\bar{c}$, gg and $\tau\bar{\tau}$ pairs represents a major challenge for the vertex detector system. An extended Higgs sector will most likely manifest itself via the production and the decay of pairs of heavy Higgs particles by processes such as $e^+e^- \rightarrow H^+H^- \rightarrow t\bar{t}b$ or $e^+e^- \rightarrow H^0A^0 \rightarrow b\bar{b}b$ that can be discriminated from the multi-fermion background thanks to their distinctive signatures with multiple b jets. If supersymmetry exist, for example the scalar top will produce complex final states such as $\tilde{t}_l \rightarrow b\tilde{\chi}_l^+ \rightarrow bW^+\tilde{\chi}_l^0$ for which both b and c tagging are important. Standard Model processes such as $t\bar{t} \rightarrow bW^+\bar{b}W^-$ provide equally challenging requirements. As a final example, possible anomalies in the

gauge boson self-couplings will be probed by using high energy WW production in which one W decays leptonically and the other hadronically to cs , an analysis which profit well from a high charm tag efficiency and purity.

Energy Flow

Most signatures of new physics are expected to be found in hadronic final states where intermediate states, such as $t \rightarrow bW$, $W \rightarrow q\bar{q}'$ or $Z \rightarrow q\bar{q}$ must be detected in the cascade to efficiently suppress the expected Standard Model backgrounds. The effect of beamstrahlung and initial state radiation (IRS), the complexity of the signal final states and the presence of missing energy in fusion processes and in reactions involving SUSY particles reduce the applicability of kinematic constraints to enhance the di-jet mass resolution, thus requiring excellent performance in terms of accuracy on the energy and direction of partons. Some SUSY models demand sensitivity to non-pointing tracks and photons, also good τ identification is vital for multi- τ final states in supersymmetric scenarios with large values of $\tan\beta$.

Experience at LEP, SLC and HERA has shown that such multi-parton final states are best analysed using energy flow measurement, where the demand for unprecedented performance is opening new avenues of approach and technical innovations. The energy flow technique combines the information from tracking and calorimetry to obtain an optimal estimate of the flow of particles and of the original parton four momenta. This works best if together with the tracking system both calorimeters are located within the coil. This keeps the amount of inactive material in front of the calorimeters low and allows for the optimisation of calorimetric measurement. The calorimeters must have excellent three dimensional granularity to enable an energy flow algorithm which resolves energy depositions of almost overlapping particles, combines redundant measurements

properly, and performs additional corrections e.g. calorimeter software compensation. Good particle identification and good coverage for long lived particles will add valuable information for each event.

Hermeticity

Hermeticity and particle detection capabilities at small angles are required as missing energy is the main signature expected for the production and decay of supersymmetric particles and for other processes of interest, such as $e^+e^- \rightarrow WW\nu_e\bar{\nu}_e$, which are forward peaked. Excellent missing energy resolution will increase the sensitivity to supersymmetry in those cases with small mass difference $\overline{\Delta}M$ between the lightest and the next lightest SUSY particle. Missing energy is also a signature for many extra-dimension scenarios.

Tracking System

In order to meet the tracking requirements discussed above, a detector has been proposed with the following components

- a large Time Projection Chamber (TPC) of radius 170cm and length 2×273 cm with ~ 200 readout points in the radial direction;
- a multi-layered pixel micro-vertex detector (VTX) between $r = 1.5$ cm and $r = 6.0$ cm;
- an additional silicon tracking detector between the VTX and the TPC consisting of cylinders (SIT) and discs in the forward region (FTD);
- a precise forward chamber located behind the TPC endplate (FCH)

The complete tracking system is immersed in a magnetic field of 4T.

Calorimeter System

As has been discussed above the detector must include both electromagnetic and hadronic calorimeters, which in order to meet the necessary level of performance, must be housed within the magnetic coil (Valkar et al. 2002). To date two proposals have been put forward for each of the calorimeter sub-detectors.

For the electromagnetic calorimeter (ECAL), the two options are;

- a very high granularity 3D calorimeter, using tungsten absorbers and silicon diode pads. The Si-W calorimeter, which is perfectly suited for energy flow measurements, must be supported by an appropriate algorithm to fully profit from its imaging capabilities,
- A Shashlik EM Calorimeter with Longitudinal Segmentation.

For the hadronic calorimeter (HCAL)

- an Fe/scintillating tile calorimeter with high transverse and longitudinal segmentation, in order to allow for software compensation.
- a fully digital calorimeter with imaging capabilities, where the active layers are constructed from gas detectors.

Both the HCAL and ECAL will be complemented by forward calorimeters, a low angle tagger (LAT), and, a luminosity calorimeter (LCAL), which cover polar angles down to 4.6mrad. These calorimeters despite their small size have a large impact on performance since they enhance missing energy resolution, provide electron identification and measure single bunch luminosity.

Muon System

The primary task of the muon detector is to identify muons and provide a hardware and/or software trigger for them. Secondly the muon detector can provide

a mechanism for detecting the tail of hadronic showers. The muon detector is located behind the magnetic coil, the iron of the flux return serves as an absorber, for which purpose it is segmented in slabs. The slab thickness is defined by the required robustness of the μ identification performance and by the calorimetric resolution desired for operating in the tail catching mode. At present two technologies have been put forward to fulfil the role of the active detector, these are, plastic streamer tubes (PST) and resistive plate chambers (RPC).

4.4 Transition Radiation Detector for the TESLA Experiment

The identification of electrons in the TESLA detector can be achieved using both destructive (electron shower in Calorimeter) or non-destructive techniques (dE/dx measurements in the TPC and/or usage of transition radiation).

In the case of calorimetry the information about the spatial shower development, both laterally and longitudinally, must be used. This in turn requires a very fine calorimeter cell granularity to allow a good measurement of the first and second moments of the shower shape. As an example, the H1 liquid-argon calorimeter (Andrieu et al. 1994) has a sampling structure very similar to that proposed for the TESLA detector (shashlik calorimeter option). With an electromagnetic cell size of $\sim 30mm$ gives a pion misidentification at 30 GeV of 2 to $5 \cdot 10^{-3}$ leading to a pion rejection power of 200 to 500, with 95 % of electrons being correctly identified. Further improvement of the calorimeter rejection power, by a factor of 2 to 4, can be achieved using a 1 to 2 X_0 presampler. For lower energies (Andrieu et al. 1994) the π -rejection is considerably worse, by a factor of 5 for 10 GeV.

This calorimeter rejection factor is related to isolated particles (π or e). In

the case of high energy jets the calorimeter particle identification is expected to be considerably worse (*ATLAS inner detector: Technical design report. Vol. 1* 1997) due to overlap of jet particles. For instance some estimates based on the simulation of reaction of $t\bar{t}$ final states at $\sqrt{s}=500$ GeV give the fraction of overlapping hits inside electromagnetic shower envelop (at least 3×3 towers) of about 10%.

Measurements of dE/dx by the TPC is a powerful tool for electron identification but this is only possible at low energies. For example, at least 3σ separation is possible up to 8 GeV but this reduces to only 1.5σ separation at 20 GeV (Buskulic et al. 1995). Note that the separation, in standard deviations, between particle species in hadronic jets is also heavily influenced by track overlap in the TPC (Buskulic et al. 1995).

It is possible to achieve an additional e/π separation (non-destructive), by making use of the transition radiation X-rays produced by electrons. It is proposed that a TRD be positioned in the radial space between the Si-tracker and the TPC.

4.4.1 New Concept of a TRD

In order to estimate the possibility of using transition radiation for particle identification in the TESLA experiment, and to judge the performance of an applicable detector, a Monte Carlo study was performed as part of this study using the GEANT based simulation programme of transition radiation.

Usually transition radiation detectors in high energy physics experiments detect transition radiation photons, together with dE/dx losses of the particle. These losses form the major contribution to the background in transition radiation measurements, and it is this which limits the hadron rejection capability of TRDs. For instance, the achievable hadron rejection level is only about 5 for the

total TRD length, $\sim 18\text{cm}$, available within the TESLA detector (a radial spacing between Si-tracker and TPC). Background due to dE/dx seems unavoidable because the transition radiation angle is very small, $\sim 1/\gamma$.

However in the case of the TESLA detector with its high magnetic field, $B = 3\text{T}$, one can make use of the separation in space of the particle trajectory, which is deflected by the B field, and that of the transition radiation photons.

The deflection distance between the particle track and transition radiation photon detected is given by:

$$\delta \sim \frac{L^2 B}{p}$$

where:

L is the particle path length between transition radiation radiator and detector
 p is the momentum of the particle.

The typical δ -value for the proposed TRD position is about

$$200\mu\text{m} \left(\frac{30\text{GeV}/c}{p\text{GeV}/c} \right)$$

for $\theta = 90^\circ$ (See Fig. 4.4).

So completely separate detection of the transition radiation photons and the associated particle track is possible using a high granularity detector, for example Si-pixel or Si-strip detectors.

In such a case, if the mean number of transition radiation photons is large enough to give a good electron efficiency, the hadron rejection is determined not by background associated with particle dE/dx as usual, but by external backgrounds. This background may consist of γ s from beam-beam effects and synchrotron radiation or coincidental particle hits. In this case the e /hadron separation is expected to be sufficient over a wide range of electron energies from the transition radiation threshold, approximately 2 GeV, and above (see below).

4.4.2 TESLA TRD design and analysis

It is proposed that the TRD be located in the intermediate gap between the Si-tracker and the TPC (radial spacing of 12 to 30 *cm*). The proposed structure is shown in Fig. 4.2.

- The transition radiation radiator consists of 300 polypropylene foils each 20 μm thick. The radial thickness of the radiator is Z dependent and varies from 8 *cm* to 3 *cm*, in order to maintain the same radiator thickness over all values of the TRD polar angle θ . The radiator thickness is about 1% of X_0 (independent of rapidity) and $\Delta Z = \pm 50 cm$.
- The particle and transition radiation X-ray detector will use Si-pixels with a pixel size of 50 $\mu m \times$ few *mm* in Z . The Si-pixel thickness of 400 μm is used in order to obtain a good absorption of transition radiation X-rays, 5 – 30 keV. The pixel pitch of 50 μm , in the B-field bending plane, is needed for separate detection of particle and TR-photons. The pixel length is a compromise between total number of pixels, approximately 10^7 , and the requirement of having a small pixel capacitance, in order to obtain acceptable electronics noise at a level of 200-300 e (Ragusa 2000), (Dabrowski, Bialas, Grybos, Idzik & Kudlaty 2000). Each pixel has a very small acceptance, $\Delta\psi \times \Delta\eta(\theta = 90^\circ) = 1.7 \cdot 10^{-4} \cdot 8 \cdot 10^{-3}$.

The radial thickness of the Si-pixel detector and electronics is about 1% of X_0 , including the mechanical support (*Conceptual Design of a 500 GeV e^+e^- Linear Collider with Integrated X-ray Laser Facility* 1997).

To perform the detailed analysis of the TRD for the TESLA experiment the full MC simulation programme of transition radiation was used to create a new simulation programme which included the simulation of X-ray detection in Si pixel

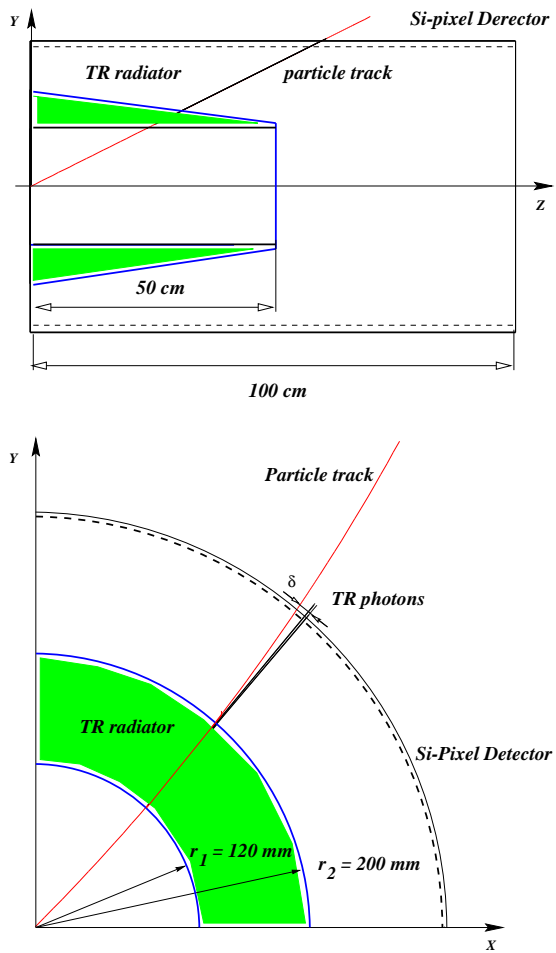


Fig. 4.2: Schematic view of the transition radiation radiator and Si-pixel TRD concept

detectors with high spatial resolution, and the propagation of charged particles within a high magnetic field and their ionisation losses in Si pixel detectors.

The key parameter which defines the TRD performance is the distance between the track and the transition radiation photons (δ). The δ - value is shown in Fig. 4.3 for the TRD geometry described in Fig. 4.2 and for pseudorapidity $\eta = 0$.

Fig. 4.4 shows the two-dimensional plot of $E_{TR_{photon}}$ vs δ for electrons with a momentum of 30 GeV/c. One can see that there is a difference between the values of δ for photons radiated at the beginning of the transition radiation radiator, $\delta_{max} = 500\mu m$, and those which are radiated at the end of the transition radiation radiator, $\delta_{min} = 150\mu m$. The energy spectrum of the transition radiation photons absorbed by a Si detector of thickness $400\mu m$ is shown in Fig. 4.5 while the distribution of the number of detected transition radiation photons is shown in Fig. 4.6. One can see that:

Fig 4.4 - Fig 4.6 are related to $\eta = 0$ ($\theta = 90^\circ$). The same distributions for $\eta = 1.3$ ($\theta = 30^\circ$) are shown in Fig 4.7 - Fig 4.9.

- the mean number of detected transition radiation photons is about 3 per electron. This shows, that the requirement of detecting at least one photon corresponds to an electron efficiency of $\epsilon = 1 - e^{-3} = 0.95$.
- the mean transition radiation detected photon energy is about 11 keV. To keep an electron efficiency of $\geq 90\%$ it is necessary to detect transition radiation photons above a threshold of 5-6 keV.
- There is no significant difference in transition radiation yield for the two different rapidities.
- There is significant narrowing in the range of δ for $\eta = 1.3$ due to smaller radial thickness of the transition radiation radiator (See Fig 4.2).

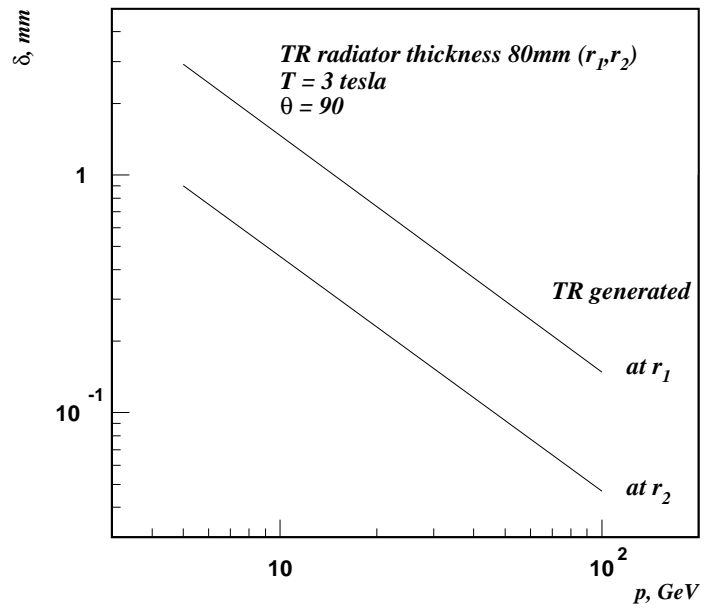


Fig. 4.3: Separation, δ , between particle track and transition radiation photons for proposed Si-pixel TRD geometry. Values of δ - for a radiator thickness of 8 cm at $\theta = 90^\circ$

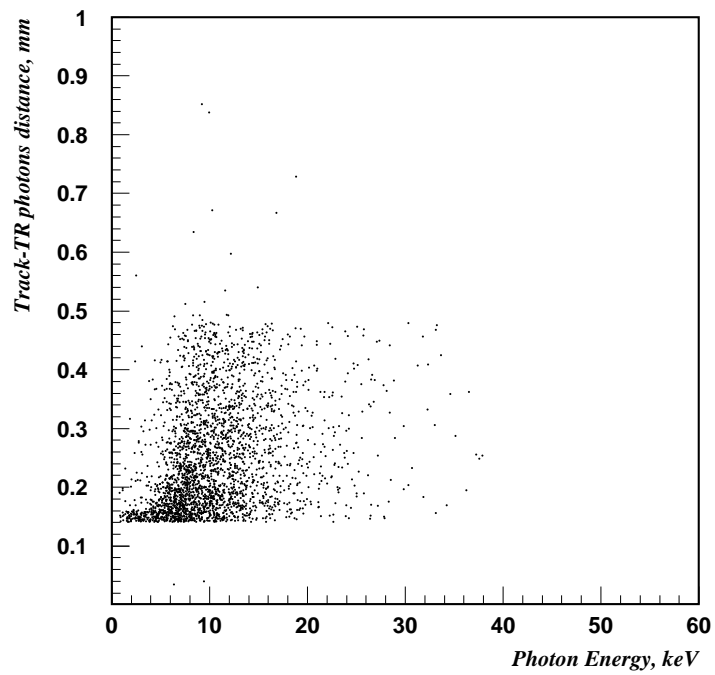


Fig. 4.4: Two dimensional plot of δ vs absorbed transition radiation photons energy ($\theta = 90^\circ$) for electrons with a momentum of $30 \text{ GeV}/c$

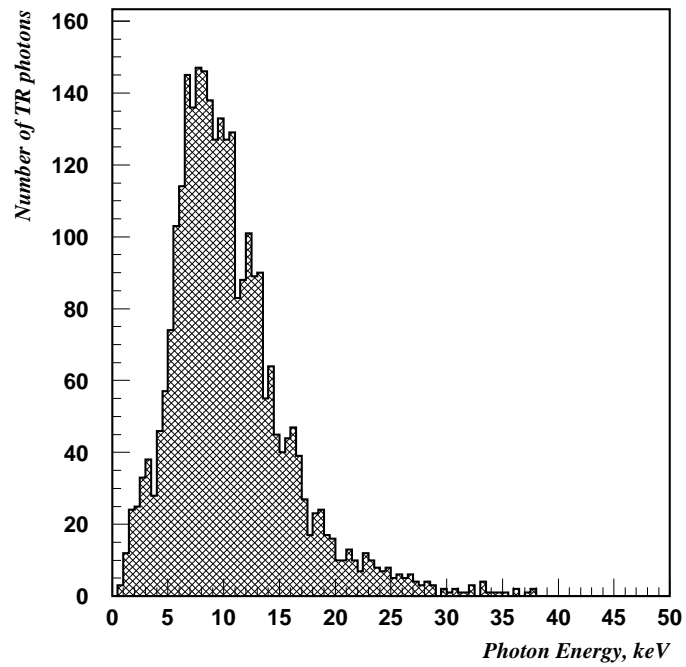


Fig. 4.5: *The energy spectrum of the transition radiation photons absorbed in Si-pixel detector ($p = 30 \text{ GeV}/c$, $\theta = 90^\circ$.)*

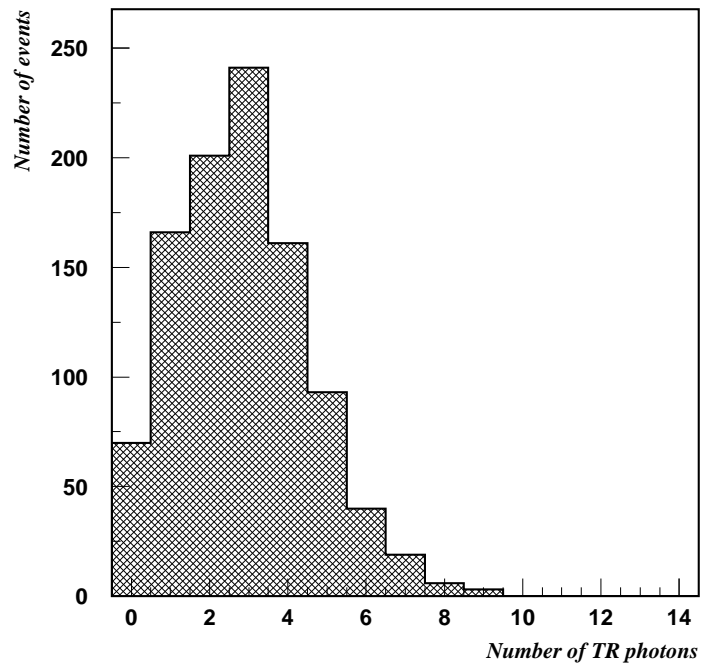


Fig. 4.6: *Distribution of the number of detected transition radiation photons ($p = 30$ GeV/c, $\theta = 90^\circ$.)*

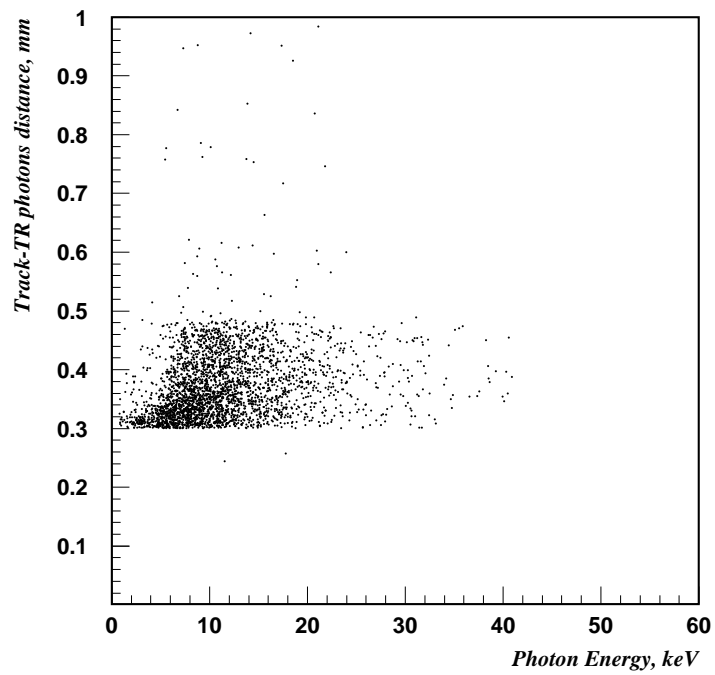


Fig. 4.7: Two dimensional plot of δ vs absorbed transition radiation photons energy ($\theta = 30^\circ$) for electron momentum of $30 \text{ GeV}/c$.

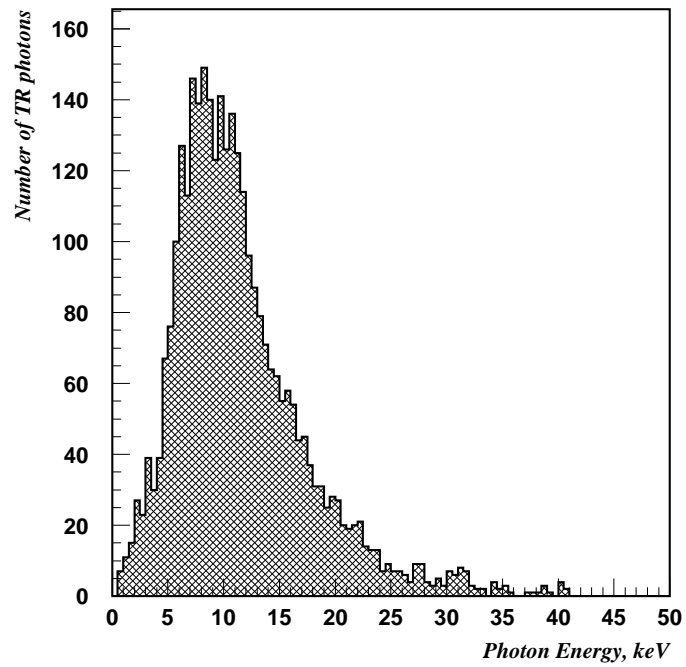


Fig. 4.8: *The energy spectrum of the transition radiation photons absorbed in Si-pixel detector ($p = 30 \text{ GeV}/c$, $\theta = 30^\circ$.)*

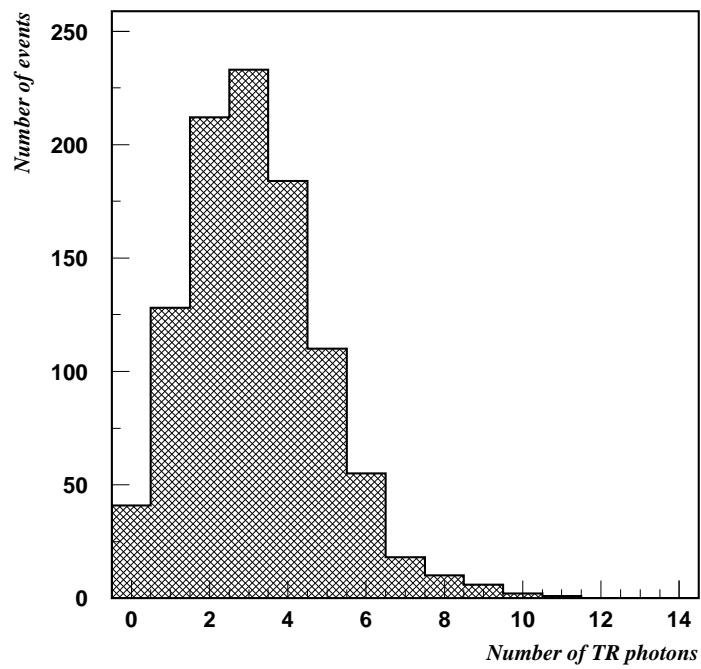


Fig. 4.9: *Distribution of the number of detected transition radiation photons ($p = 30$ GeV/c, $\theta = 30^\circ$.)*

In order to misidentify the hadron as an electron there should be at least one hit in a pixel(s), which is positioned in the region of the track location, known from the Si-tracker and TPC (See Fig 4.4, Fig 4.7). The total area of such a “transition radiation expected” pixel(s) is about 1 - 5 mm^2 (p_{\perp} - dependent).

The probability of the pion misidentification is ε_{π} which is determined by the following:

- Coincidental particle hits in Si-pixels, which are expected to be triggered by transition radiation X-rays. The expected position of such Si-pixels is known from the track position and particle momentum which can be obtained from Si-tracker and TPC. The expected hit density even inside a high energy jet can be estimated at $\sim 10^{-3}hits/mm^2$ for each bunch crossing and $r = 30cm$, where the Si-TRD is located. Moreover, the energy losses of the jet particle will be about 140 keV, compared to 5 - 60 keV for the transition radiation X-ray signal.
- Coincidental γ -ray hits originating from beam-beam effects and beam synchrotron radiation. The estimation from background studies, for the TPC gives an upper limit of about 100 $hits/bunch$ over the whole Si-TRD, which is less than $2 \cdot 10^{-5}hits/mm^2bunch$. There is a possibility that this number may increase due to the formation of tightly spiralling slow electrons in the B-field, although this has yet to be studied.
- Charge sharing due to the Lorentz angle. The Si-pixel TRD will operate in a magnetic field of 3 TESLA, the magnetic field and electric drift field inside the silicon pixel detector therefore will be orthogonal and the drift velocity will assume a component along the direction of $\mathbf{E} \times \mathbf{B}$. The charge carriers will then drift at an angle θ_L with respect to the direction of the electric field, θ_L being the Lorentz angle. Depending on the angle of the

incident particle, the charge collected will spread between pixel cells. The spread being minimum where θ equals θ_L . The Lorentz angle θ_L has been measured (Ragusa 2000) for $B = 1.4T$ and can be predicted for the TESLA detector as $\sim 20^\circ$. In order to avoid this pixel to pixel spread, the Si-pixel detector must be tilted at an angle of θ_L . The pixel to pixel spread due to the magnetic bending angle of the particle in the Si-pixel detector is much smaller than the track - transition radiation photon distance:

$$4\mu m \cdot \left(\frac{30\text{GeV}/c}{p}\right) \quad \text{compared to} \quad 200\mu m \cdot \left(\frac{30\text{GeV}/c}{p}\right)$$

and can be neglected.

For the high momentum region, where the pion Lorentz-factor is quite large, there is a principal limitation of e/π separation as pions will start to radiate transition radiation photons.

The pion transition radiation yield becomes comparable with that of electron transition radiation yield at momenta over $200 - 300 \text{ GeV}/c$.

Finally Fig. 4.10 shows the estimated pion misidentification probability vs momentum; two ε_π values are presented: one is based on double (triple) hit rates in pixels with a pitch of $50\mu m$ (Ragusa 2000) from relativistic particle, the second is determined by the transition radiation yield from pions.

As one can see from Fig. 4.10, the main process which defines the e/π separation for all TRD rapidity coverage is transition radiation emitted by pions. Nevertheless the expected probability for pions to be misidentified as electrons is quite low, $\leq 10^{-2}$, for pions with transverse momentum up to $p_T \simeq 40 \text{ GeV}/c$, and not worse than ~ 6 for momentum up to $p \simeq 90 \text{ GeV}/c$.

Concerning the tracking capability of Si-pixel TRD, the spatial resolution expected is $\sim 15\mu m$ in the $r - \psi$ plane (Ragusa 2000), and $\sim 1mm$ in Z . As the $r - \phi$ and Z resolution of the Si-pixel detector is substantially better than

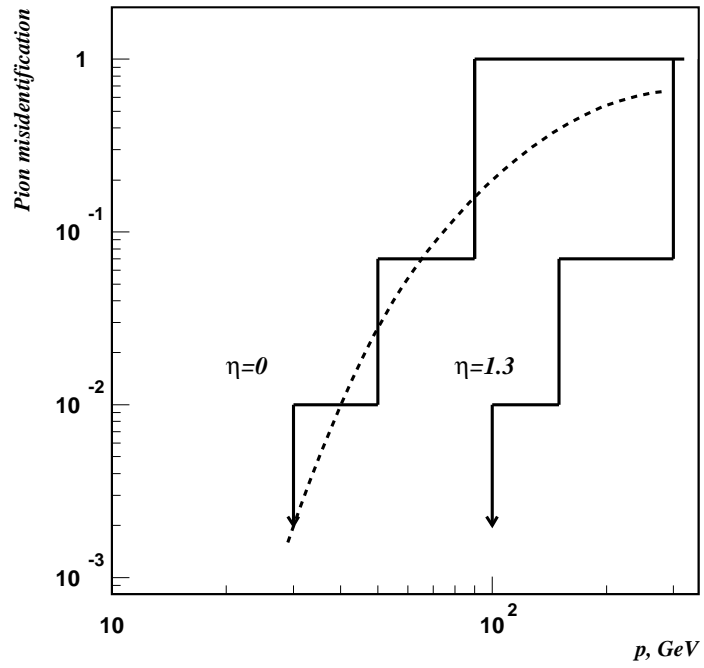


Fig. 4.10: Pion misidentification probability as a function of the momentum for electron efficiency = 90%: solid line - determined by charge sharing between Si-pixels; dashed line - determined by transition radiation radiation from pions(not dependent on η).

the TPC resolution, the additional Si track detector at $r = 30 \text{ cm}$ will be useful (J.Hanschidt 2000) for the improvement of the momentum resolution, and the improvement of the track merging efficiency for a matching procedure between TPC and VTX detector.

Chapter 5

Conclusion

This thesis sets out the analysis and mathematical modelling of transition radiation as a phenomena of classical electromagnetism, and the development of its practical application for use in high energy physics experiments.

The physical phenomena of transition radiation is the radiation which is created when a charged particle crosses the boundary between two media with different dielectric properties. The strong dependence of transition radiation on the Lorentz factor γ of the elementary particles gives the possibility to use transition radiation as a powerful method of non destructive particle identification in experimental high energy physics.

The main outcomes are:

- Analysis of the physical phenomena of transition radiation and mathematical models based on classical electrodynamics, with emphasis on the relativistic case for applications in high energy physics.
- Development of a package of programmes for mathematical simulation of transition including single interface structure, periodic structure of material with different dielectric properties, including processes of interference and absorption of transition radiation within periodic structures and the

detection of transition radiation photons. This tool allows analysis of transition radiation for elementary particles over a wide energy range up to ~ 100 GeV, within an accuracy of $\sim 10\%$.

- Development of an interface to implement the transition radiation simulation into the general mathematical simulation package of experimental high energy physics, GEANT 3 detector simulation and analysis tools. This gives the possibility to study transition radiation and transition radiation detectors in experimental high energy physics.
- Analysis and optimisation of transition radiation detectors for high energy physics experiments. Analysis and optimisation of the transition radiation detector for the HERA-B experiment, where the rejection factor achieved is $\sim 10^2$ for electrons and pions in the momentum range $10 - 50$ GeV.
- The proposal and modelling of a new type of transition radiation detector using a high magnetic field for separation of charged tracks and transition radiation photons, intended for use with the next generation experiments at the future linear collider TESLA. A rejection factor for pions $5 - 10^3$ over a wide range of momentum from $1 - 300$ GeV was demonstrated.

This study formed part of the programme of research for the HERA-B experiment “An experiment to study CP violation in the B system using an internal target at the HERA proton ring” and the programme of research for the ECFA/DESY study for a future linear collider program on TESLA the superconducting electron positron linear collider with integrated X-ray laboratory.

The results have been presented in the following publications:

Egorytchev, V., Saveliev, V. and Aplin, S.J. (2000) "Particle identification via transition radiation and detectors", Nucl. Instr. Meth. **A453**, 346-352.

Egorytchev, V., Saveliev, V. and Aplin, S.J. (2000) "Electromagnetic field of a moving point charge for the relativistic approximation", pp. 32, Proceedings of the International Conference on Mathematical Physics, Mathematical Simulation and Approximate Methods, 2000.

Chamanina, J., Dolgoshein, B., Egorytchev, V., Fourletov, S., Kaoukher, S. Saveliev, V., Aplin, S.J. and Franklin, D. (2000) "Si-pixel transition radiation detector with separation of transition radiation photons and particle track by B-field. (Proposal for TESLA detector)", LC Note LC-DET-2000-038.

Chamanina J., Dolgoshein, B., Egorytchev, V., Fourletov, S., Kaoukher, S. Saveliev, V., S. Aplin, S.J. and Franklin, D. (2001) "Si-pixel transition radiation detector with separation of transition radiation photons and particle track by B-field. (Proposal for TESLA detector)", pp. 1705-1733, Proceedings of the 2nd ECFA/DESY Study 1998-2001.

Aplin, S.J. and Saveliev, V. (2002) "Simulation of transition radiation for periodic and non periodic structures" Nuclear Energy, **1**, 103-114. (In Russian)

Valkar, S. et al. (2002) "A calorimeter for the e+ e- TESLA detector: Proposal for Research and Development", DESY-PRC-RD-01-02.

Abt, I. et al. (2003) HERA-B Collaboration "Inclusive V^0 production cross sections from 920-GeV fixed target proton nucleus collisions", Eur. Phys. J. **C29**,

181-190.

Abt, I. et al. (2003) HERA-B Collaboration “ J/ψ production via χ_c decays in 920-GeV p A interactions”, Phys. Lett. **B561**, 61-72.

Abt, I. et al. (2003) HERA-B Collaboration “Measurement of the $b\bar{b}$ production cross section in 920-GeV fixed-target proton nucleus collisions”, Phys. Lett. **C26**, 345-355.

And at the following conferences

7th International Conference on Instrumentation for Colliding Beam Physics, Saveliev, V., Hamamatsu, November 15-19, 1999.

International Conference on Mathematical Physics, Mathematical Simulation and Approximate Methods, Saveliev, V., Obninsk, 15-19 May 2000.

7th Workshop of the 2nd ECFA/DESY Study of Physics and Detectors for a Linear Electron-Positron Collider, Saveliev, V., DESY Hamburg, September 22-25 2000.

Acknowledgements

Firstly I would like to thank Prof Dr. Albrecht Wagner for inviting me to DESY to undertake the work contained within this thesis. My thanks are also due to the members of the HERA-*B* collaboration for providing support, advice and in many cases friendship over the last seven years during which I have been involved in the collaboration.

I am greatly indebted to Dr. David Franklin who acted as my director of studies, for his continual support and diplomatic guidance through out the duration of what was at times a seemingly never ending task. To Dr. David Timms who having already supervised my first attempt at scientific writing was good enough to go through it all again.

During the last seven years it has been my good fortune to have Prof Dr Valeri Saveliev acting as my mentor, without whose seemingly everlasting patience and good humour all these ideas would have never seen the light of day.

A special thanks is due to my mother-in-law Dora for propping up one side of this thesis by giving me somewhere to stay at a very reasonable rate whilst I finished writing.

Such endeavours are often arduous though they are always made a little easier by a family who are always there even if they're thousands of miles away. My brother Dave who has been catching me up since the day he could crawl has seemingly made light of my head start in life by landing himself a research position without the need for writing any acknowledgements at all. My sister Sarah for reminding me there is a whole world outside this office.

My gratitude is due parents Keith and Eileen who started me on this long road of learning always somehow managing to keep me on it, even when all the wheels seemed to be coming of at once.

Finally words are not enough to describe what I want to express to my wife,

Anja, who often bore the brunt of my frustrations and absence with nothing more than a thoughtful frown. If I'd have left Germany without learning a thing about particles, photons and fields, but still met you, it would have still all been worthwhile.

Bibliography

- Abt, I. et al. (2003a), ‘Inclusive V^0 production cross sections from 920 GeV fixed target proton nucleus collisions’, *Eur. Phys. J.* **C29**, 181–190.
- Abt, I. et al. (2003b), ‘ J/ψ production via χ_c decays in 920 GeV p A interactions’, *Phys. Lett.* **B561**, 61–72.
- Abt, I. et al. (2003c), ‘Measurement of the $b\bar{b}$ production cross section in 920 GeV fixed-target proton nucleus collisions’, *Eur. Phys. J.* **C26**, 345–355.
- Albrecht, H. (1996), *ARTE, The Event Analysis and Reconstruction Tool for HERA-B*. Available:http://www-hera-b.desy.de/subgroup/software/arte/arte_manual.ps.
- Albrecht, H. et al. (1994), ‘An Experiment to Study CP Violation in the B System Using an Internal Target at the HERA Proton Ring’. DESY/PRC/94-02.
- Albrecht, H. et al. (1995), ‘An Experiment to Study CP Violation in the B System Using an Internal Target at the HERA Proton Ring (Design Report)’. DESY/PRC/95-01.
- Andrieu, B. et al. (1994), ‘Electron / pion separation with the H1 LAr calorimeters’, *Nucl. Instrum. Meth.* **A344**, 492–506.

- Apostolakis, J., Giani, S., Maire, M., Bagulya, A. V. & Grichine, V. M. (2000), ‘Parameterization models for x-ray transition radiation in the geant4 package’, *Computer Physics Communications* **132**, 241–250.
- Artru, X., Yodh, G. B. & Mennessier, G. (1975), ‘Practical theory of the multi-layered transition radiation detector’, *Phys. Rev.* **D12**, 1289.
- ATLAS inner detector: Technical design report. Vol. 1* (1997). CERN-LHCC-97-16.
- Barsukov, K. (1960), ‘Transition radiation in waveguides’, *Sov. Phys. JETP* **10**, 787–789.
- Beck, G. (1948), ‘Contribution to the theory of the Cherenkov effect’, *Phys. Rev.* **74**, 795–802.
- Berger, M., Hubbell, J., Seltzer, S., Coursey, J. S. & Zucker, D. S. (1999), *XCOM: Photon Cross Section Database (version 1.2)[Online]*, National Institute of Standards and Technology, Gaithersburg, MD. Available: <http://physics.nist.gov/xcom>.
- Bethe, H. & Ashkin, J. (1953), *Experimental Nuclear Physics*, Vol. 1, Wiley, New York.
- Blunk, O. & Leisegang, S. (1950), ‘Zum Energieverlust schneller Elektronen in dünnen Schichten’, *Z. Phys* **128**, 500–505.
- Brun, R., Hagelberg, R., Hansroul, M. & Lassalle, J. C. (1978), ‘Geant: Simulation program for particle physics experiments. user guide and reference manual’. [CERN publication, CERN-DD-78-2-REV].
- Buskulic, D. et al. (1995), ‘Performance of the ALEPH detector at LEP’, *Nucl. Instrum. Meth.* **A360**, 481–506.

- Chamanina, J., Dolgoshein, B., Egorytchev, V., Fourletov, S., Kaoukher, S., Saveliev, V., Aplin, S. & Franklin, D. (2001), ‘Si-pixel transition radiation detector with separation of tr-photons and particle track by b-field. (proposal for tesla detector)’, pp. 1705 – 1733. Proceedings of the 2nd ECFA/DESY Study 1998-2001.
- Cherry, M., Hartmann, G., Mueller, D. & Prince, T. (1974), ‘Transition radiation from relativistic electrons in periodic radiators’, *Phys.Rev.D* **10**, 3594–3607.
- Cobb, J. H., Allison, W. W. M. & Bunch, J. N. (1976), ‘The ionization loss of relativistic charged particles in thin gas samples and its use for particle identification: 1. theoretical predictions’, *Nucl. Instr. Meth.* **133**, 315.
- Conceptual Design of a 500 GeV e^+e^- Linear Collider with Integrated X-ray Laser Facility* (1997). DESY 1997-048, ECFA 1997-182.
- Dabrowski, W., Bialas, W., Grybos, P., Idzik, M. & Kudlaty, J. (2000), ‘A read-out system for position sensitive measurements of x-ray using silicon strip detectors’, *Nucl. Instrum. Meth.* **A442**, 346–354.
- Durand, L. (1975), ‘Transition radiation from ultra relativistic particles’, *Phys. Rev. D* **11**, 89–105.
- Egorychev, V., Savelev, V. & Aplin, S. J. (2000), ‘Particle identification via transition radiation and detectors’, *Nucl. Instrum. Meth.* **A453**, 346–352.
- Egorytchev, V., Saveliev, V., Sosnonstev, V. & Fourletov, S. (1999), ‘Experimental results for test run with prototype of TRD HERA-B’. MPhI preprint 01-99.
- Ehret, K. (2000), ‘Commissioning of the HERA-B internal target: Using the HERA proton ring as a B-factory’, *Nucl. Instrum. Meth.* **A446**, 190–198.

- Ermilova, V., Chechin, V., Alakoz, A., Konteko, L. & Merzon, G. (1975), ‘On the Restricted Energy Loss of Relativistic Charged Particles in Matter’, *Nucl. Instrum. Methods* **124**, 42.
- Ermilova, V. K. & Chechin, V. A. (1976), ‘The ionization loss distribution at very small absorber thickness’, *Nucl. Instrum. Meth.* **136**, 551–558.
- Ermilova, V., Konteko, L. & Merzon, G. (1977), ‘Fluctuations and the Most Probable Values of Relativistic Charged Particle Energy Loss in Thin Gas Layers’, *Nucl. Instrum. Methods* **145**, 555.
- Frank, I. (1970), *Sov. J. Nucl. Phys* **19**, 90.
- Frank, I. & Ginzburg, V. (1945), ‘Radiation of a uniformly moving electron due to its transition from one medium into another’, *J.Exptl. Theoret. Phys.(USSR.)* **9**, 353–362.
- Garibian, G. (1958), ‘Contribution to the Theory of Transition Radiation’, *J.Exptl. Theoret. Phys.(USSR.)* **6**, 1079–1085.
- Garibian, G. (1959), ‘Radiation from a charged particle traversing a layered medium’, *Sov. Phys. JETP* **8**, 1003–1006.
- Garibian, G. (1961), ‘Radiation of a particle moving accross the interface of two media with account of multiple scattering’, *Sov. Phys. JETP* **12**, 237–239.
- Garibian, G. (1971), ‘Contribution to the theory of formation of transition X-radiation in a stack of plates’, *Sov. Phys. JETP* **33**, 23–29.
- Garibian, G. & Chalikian, G. (1959), ‘The radiation from a charged particle passing through a plate’, *Sov. Phys. JETP* **8**, 894.

- Hagiwara, K. et al. (2002), ‘The Review of Particle Physics’, *Physical Review* **D66 010001**.
- Henke, B., Lee, P., Tanaka, T., Shimabukuro, R. & Fujikawa, B. (1982), ‘Low Energy X-ray Interaction Coefficients: Photoabsorption, Scattering and Reflection’, *Atomic Data and Nuclear Data Tables* **27**, 1–144.
- Hubbell, J. (1969), ‘Photon Cross Sections, Attenuation Coefficients and Energy Absorption Coefficients from 10 keV to 100 GeV’, *Natl. Stand. Ref. Data Ser.* **29**.
- Hubbell, J., Veigele, W., Briggs, E., Brown, R., Cromer, D. & Howerton, R. (1975), ‘Atomic form factors, incoherent scattering functions, and photon scattering cross sections’, *J. Phys. Chem. Ref. Data* **4**, 471–538.
- Ispirian, K., Margarian, A. & Zverev, A. (1974), ‘A Monte-Carlo Method calculation of the Distribution of Ionisation Losses’, *Nucl. Instrum. Methods* **117**, 125.
- Jackson, J. D. (1998), *Classical Electrodynamics*, third edn, John Wiley and Sons, New York.
- J.Hanschildt (2000), ‘Optimization studies of Intermediate Tracker, ECFA/DESY Study of Physics and Detectors for a Linear Electron-Positron Collider’. Padova 5-8.5.2000.
- Klein, O. & Nishina, Y. (1929), ‘Ueber die Streuung von Strahlung durch freie Elektronen nach der neuen relativistischen Quantendynamik von Dirac’, *Zeit. f. Phys.* **52**, 853–868.
- Landau, L. (1944), ‘On the energy loss of fast particles by ionization’, *Jour. Phys. USSR* **8**, 201.

- Maccabee, H. & Papworth, D. (1969), ‘Correction to Landau’s energy loss formula’, *Phys. Lett. A* **30**, 241–242.
- Pafomov, V. (1958), ‘Radiation from an electron traversing a slab’, *Sov. Phys. JETP* **6**, 829–830.
- Ragusa, F. (2000), ‘Recent developments in the ATLAS pixel detector’, *Nucl. Instrum. Meth.* **A447**, 184–193.
- Ramsey, W. & Mackee, J. (1978), ‘A comment on the contribution of transition radiation to the x-ray background from proton induced x-ray emission’, *J. Phys. B* **11**, L313–L315.
- Saveliev, V. (1998), ‘The HERA-B transition radiation detector’, *Nucl. Instrum. Meth.* **A408**, 289–295.
- Saveliev, V. (2002), ‘Simulation of Transition Radiation’, *Mathematical Modelling. RAS.* **14 (11)**, 93–112.
- Scofield, J. (1973), ‘Theoretical photoionization cross sections from 1 to 1500 kev’. Lawrence Livermore National Laboratory Rep. UCRL-51326.
- Sjostrand, T. (1993), ‘Pythia 5.7 and Jetset 7.4 physics and manual’. [CERN publication, CERN-TH-7112-93].
- Sommerfeld, A. (1909), ‘Propagation of Waves in Wireless Telegraphy’, *Ann. Phys.* **28**, 665–737.
- Sternheimer, R. & Peierls, F. (1971), ‘General expression for the density effect for the ionisation loss of charged particles’, *Phys. Rev. B* **3**, 3681–3692.
- Understanding Matter, Energy, Space and Time: the Case for the Linear Collider* (2003). Available at: http://sbhepnt.physics.sunysb.edu/~grannis/ilcsc/lc_icfa_v6.3.pdf.

Valkar, S. et al. (2002), 'A calorimeter for the e^+e^- tesla detector: Proposal for research and development'. DESY-PRC-RD-01-02.

Vavilov, P. (1957), 'Ionisation losses of high energy heavy particles', *Sov. Phys. - JTEP* **5**, 749–751.

Zrelov, V. P. & Ruzicka, J. (1978), 'Some peculiarities of the optical transition radiation from high-energy particles at an inclined incidence.', *Nucl. Instrum. Meth.* **151**, 395.

APPENDIX: Flow Diagrams Describing Transition Radiation Simulation Programme

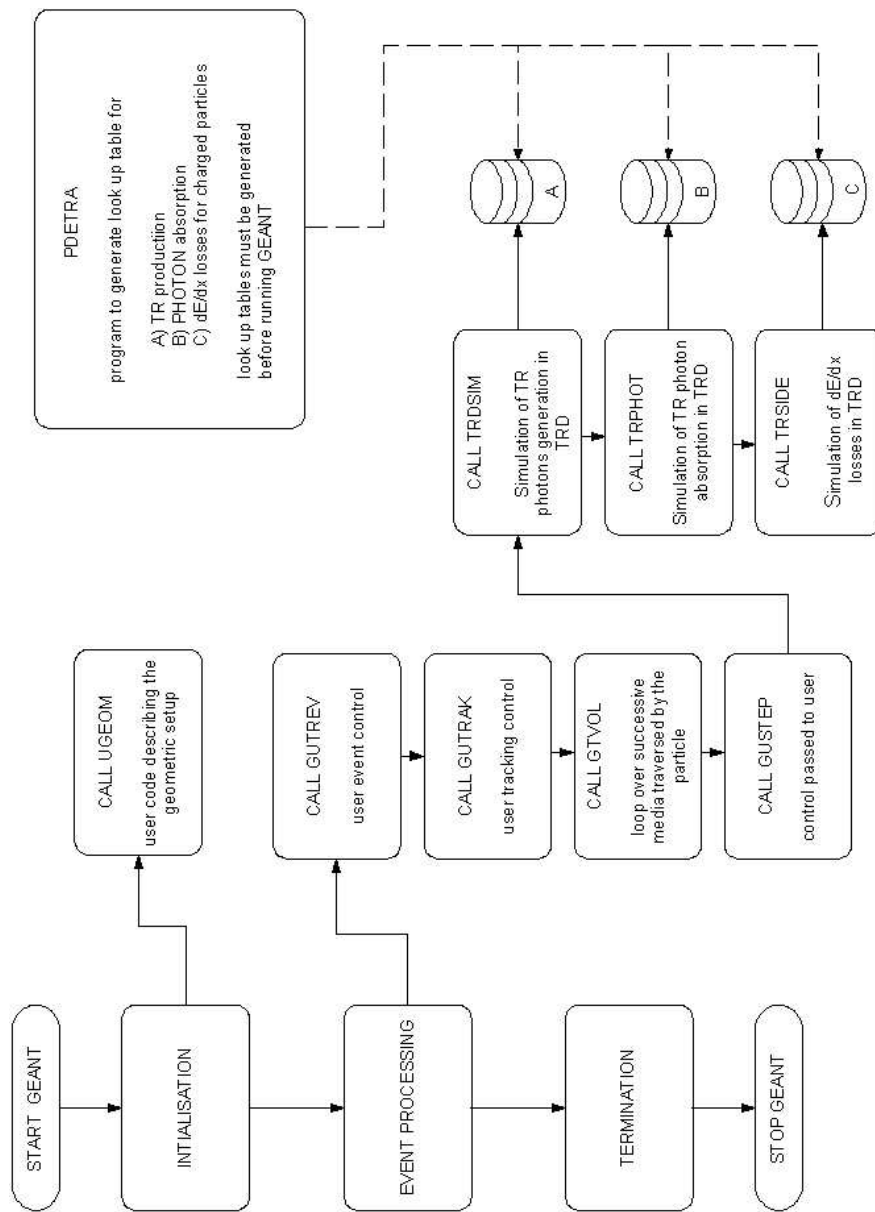


Fig. 5.1: Implementation of simulation programme in GEANT

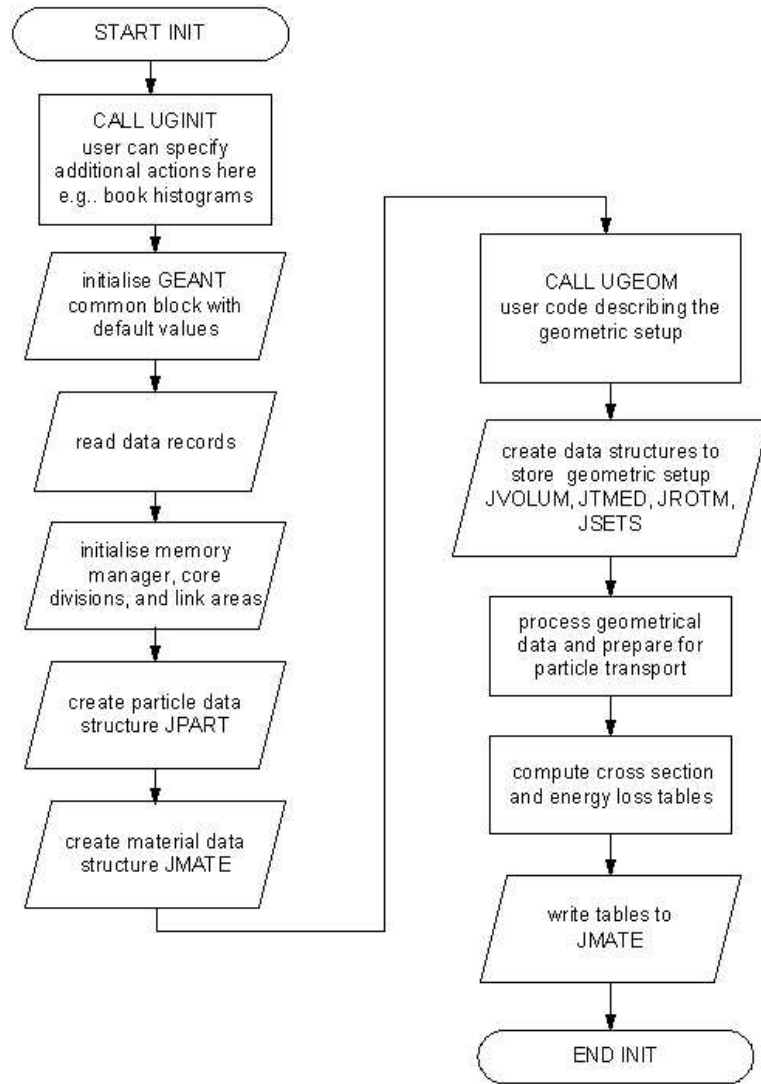


Fig. 5.2: *GEANT* initialisation

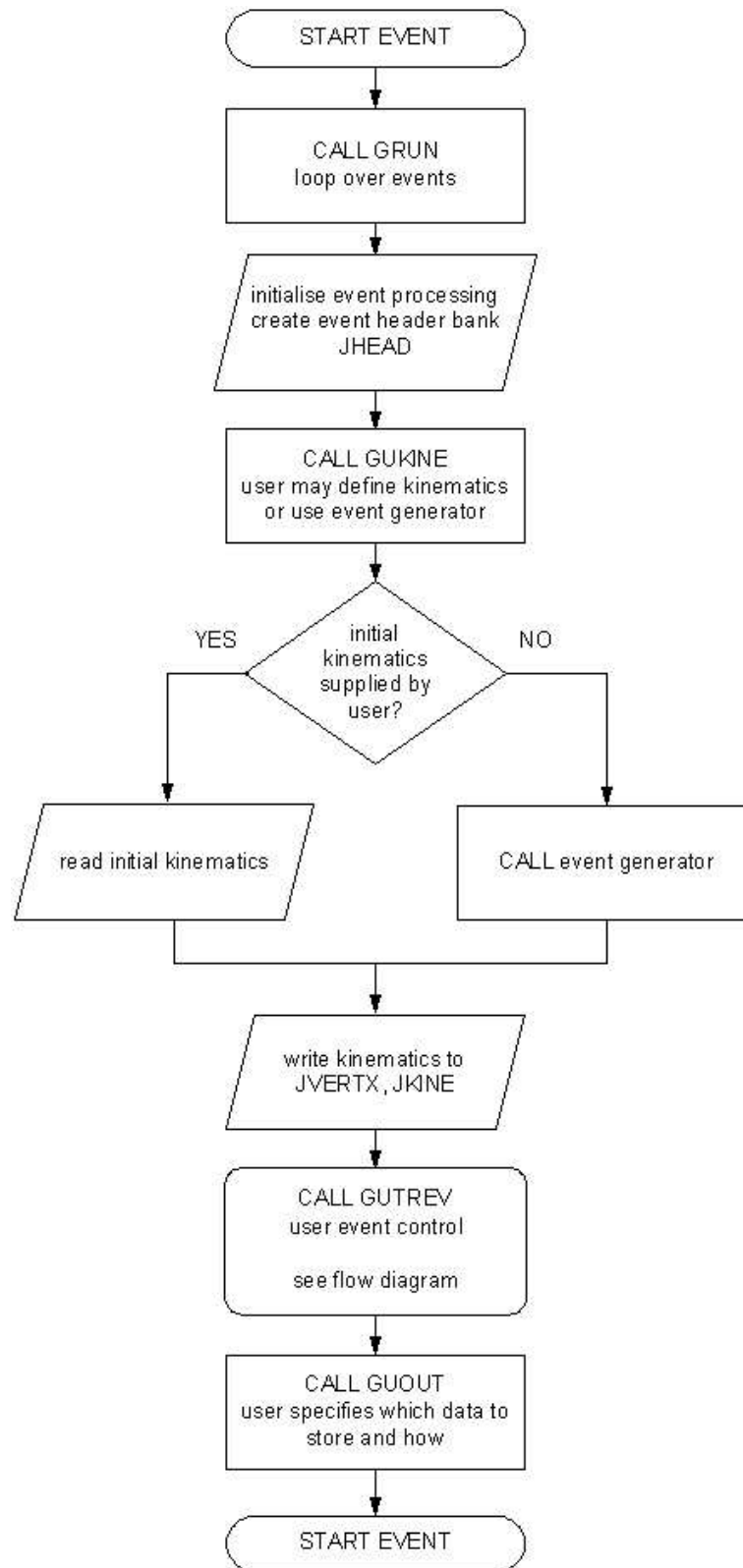


Fig. 5.3: *GEANT* event handling

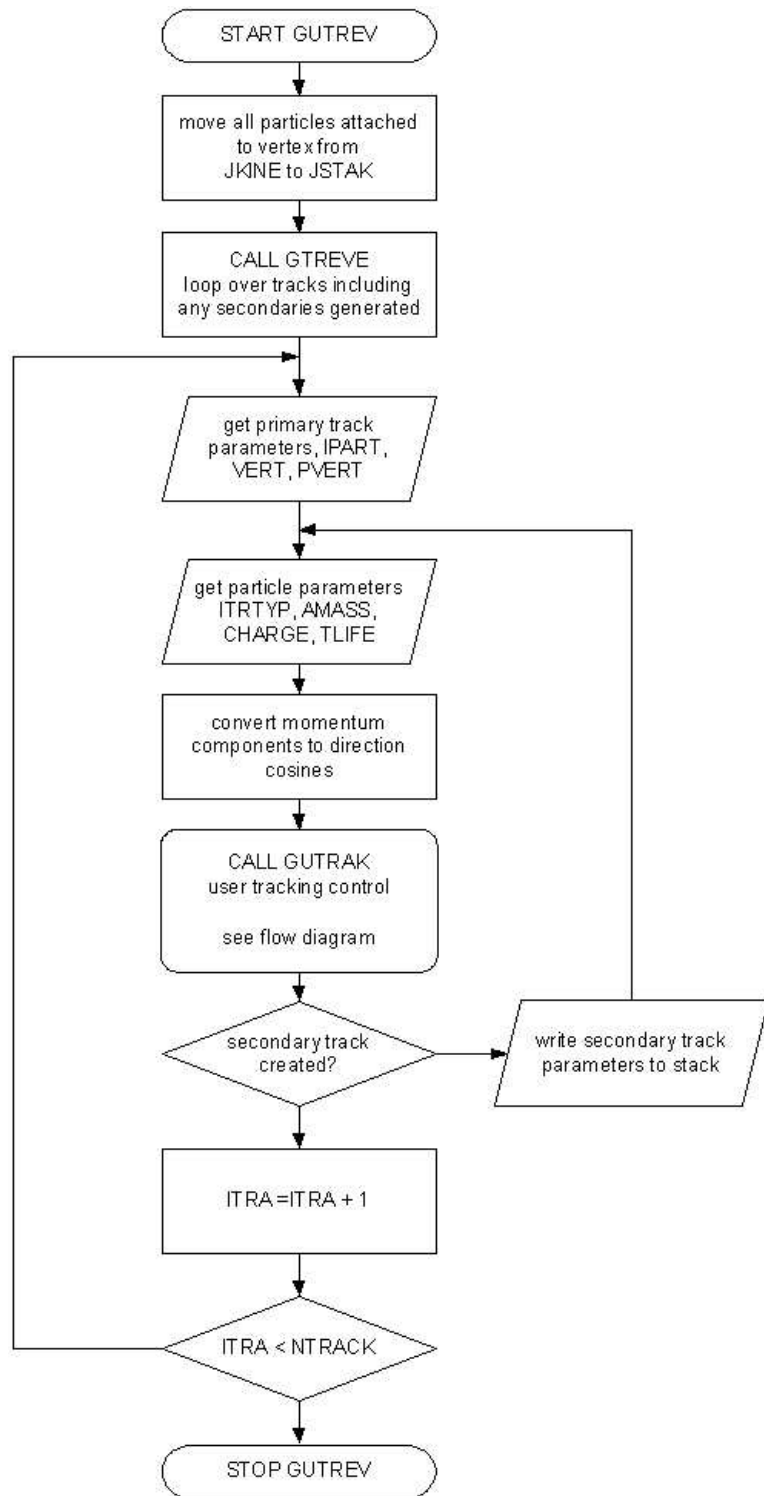


Fig. 5.4: *GEANT GUTREV*

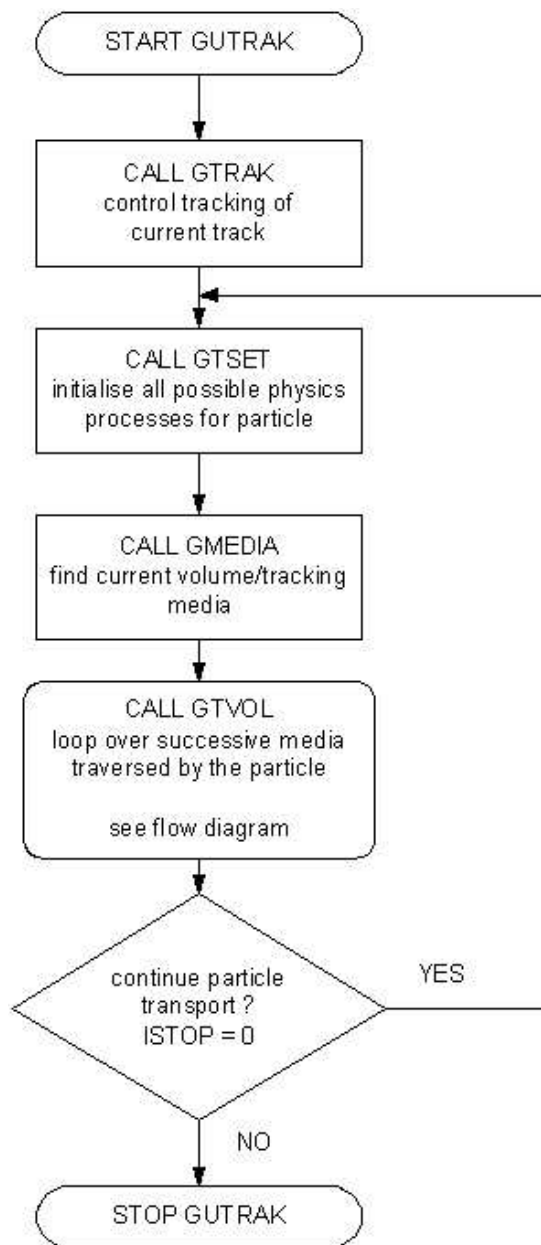


Fig. 5.5: *GEANT GUTRAK*

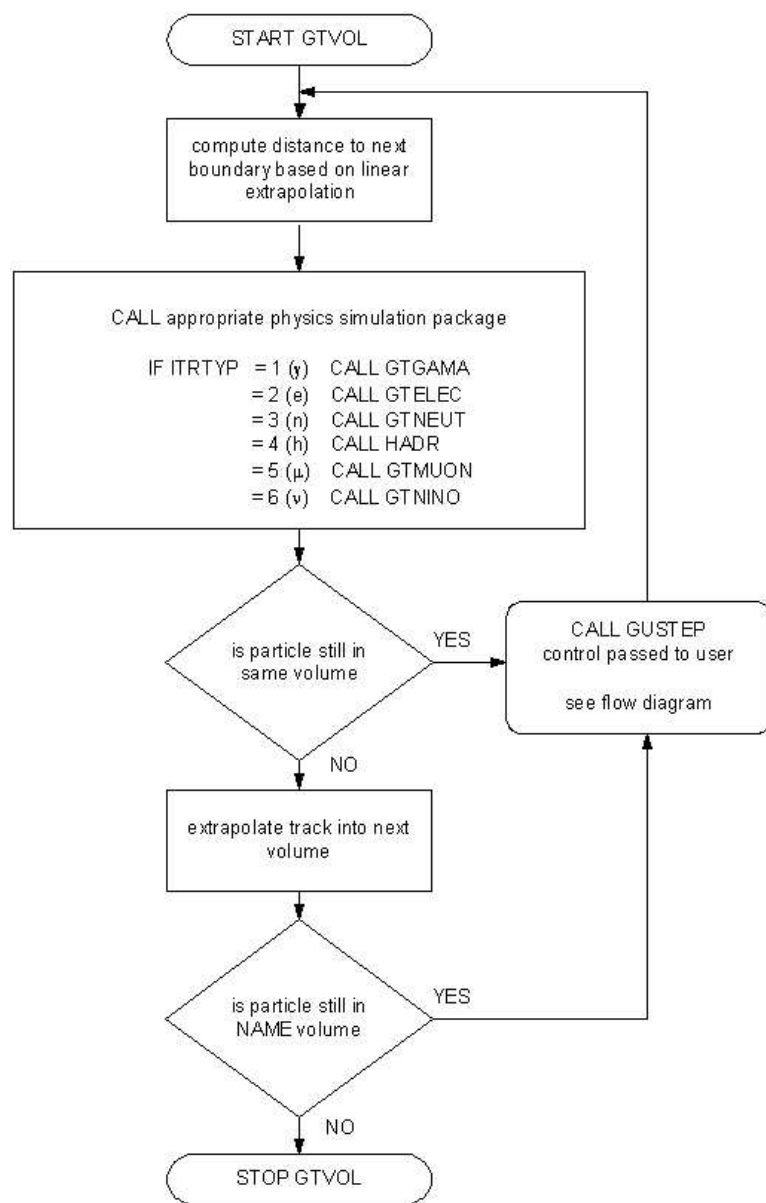


Fig. 5.6: *GEANT GTVOL*

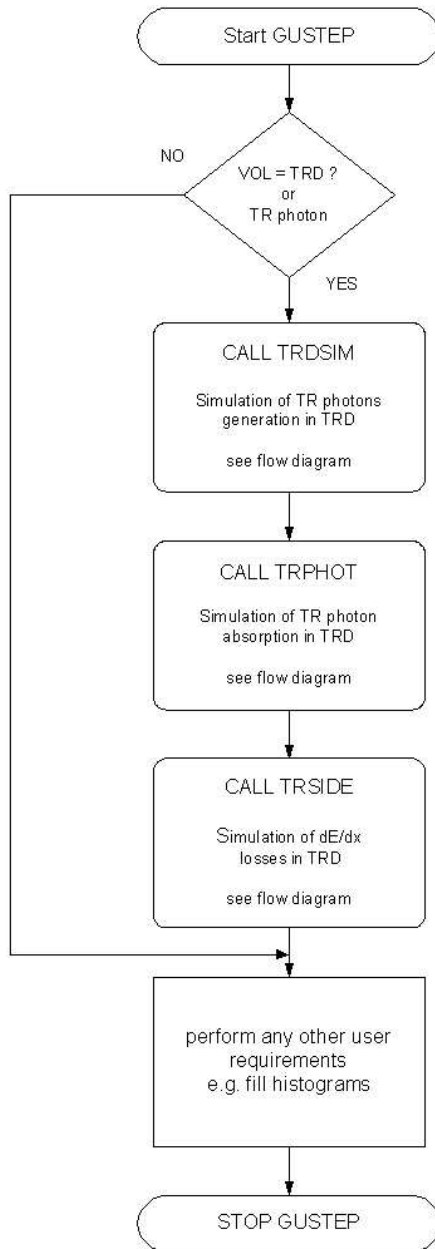


Fig. 5.7: *GEANT GUSTEP*

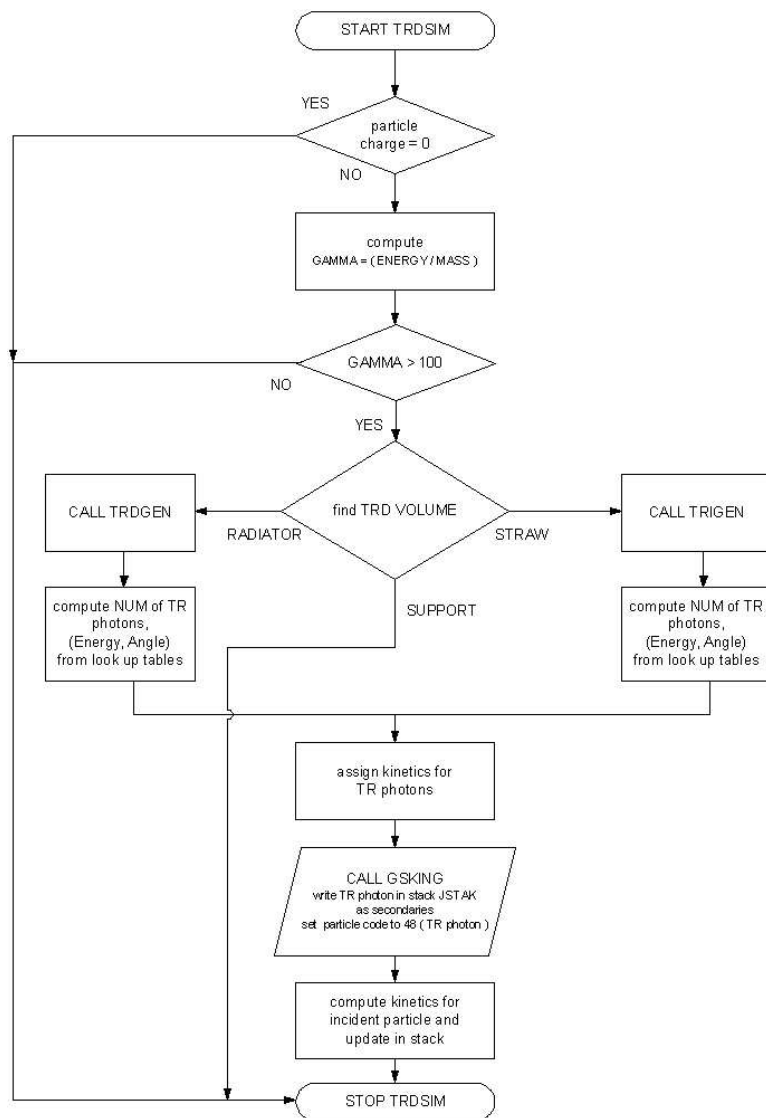


Fig. 5.8: Simulation programme TRDSIM.F

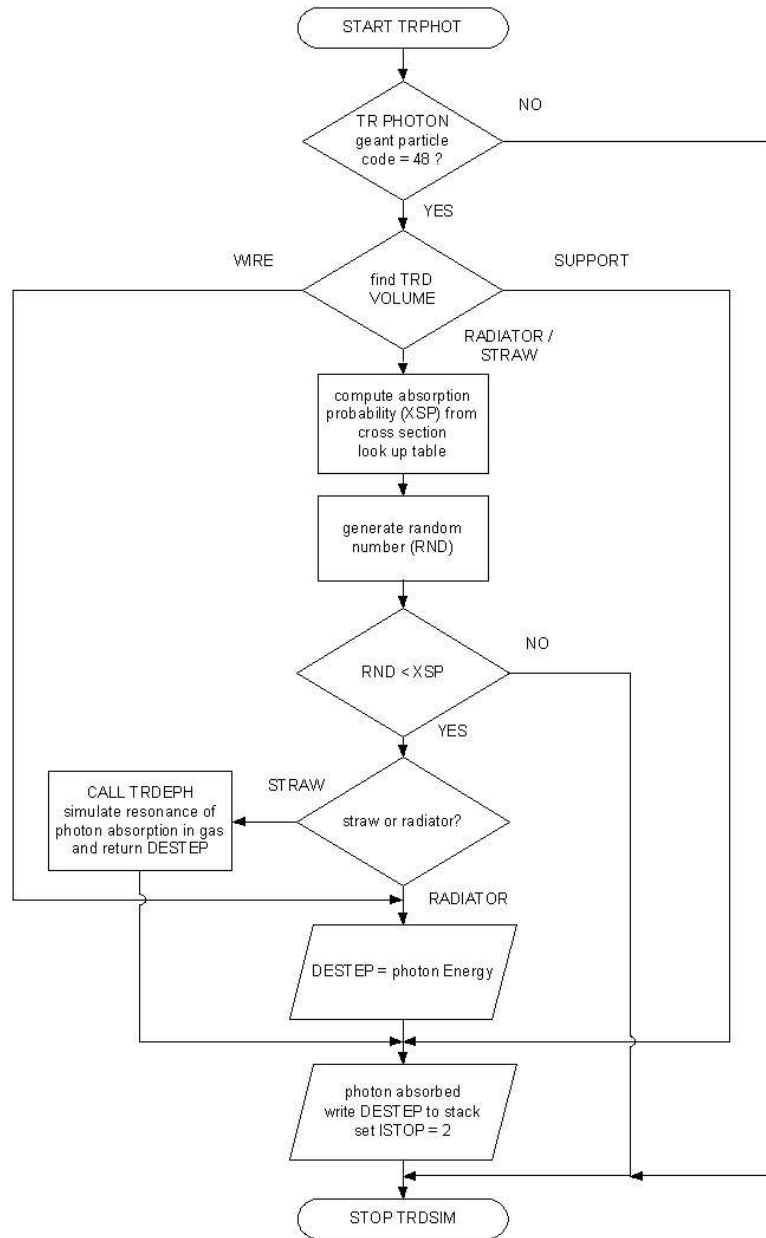


Fig. 5.9: *Simulation programme TRPHOT.F*

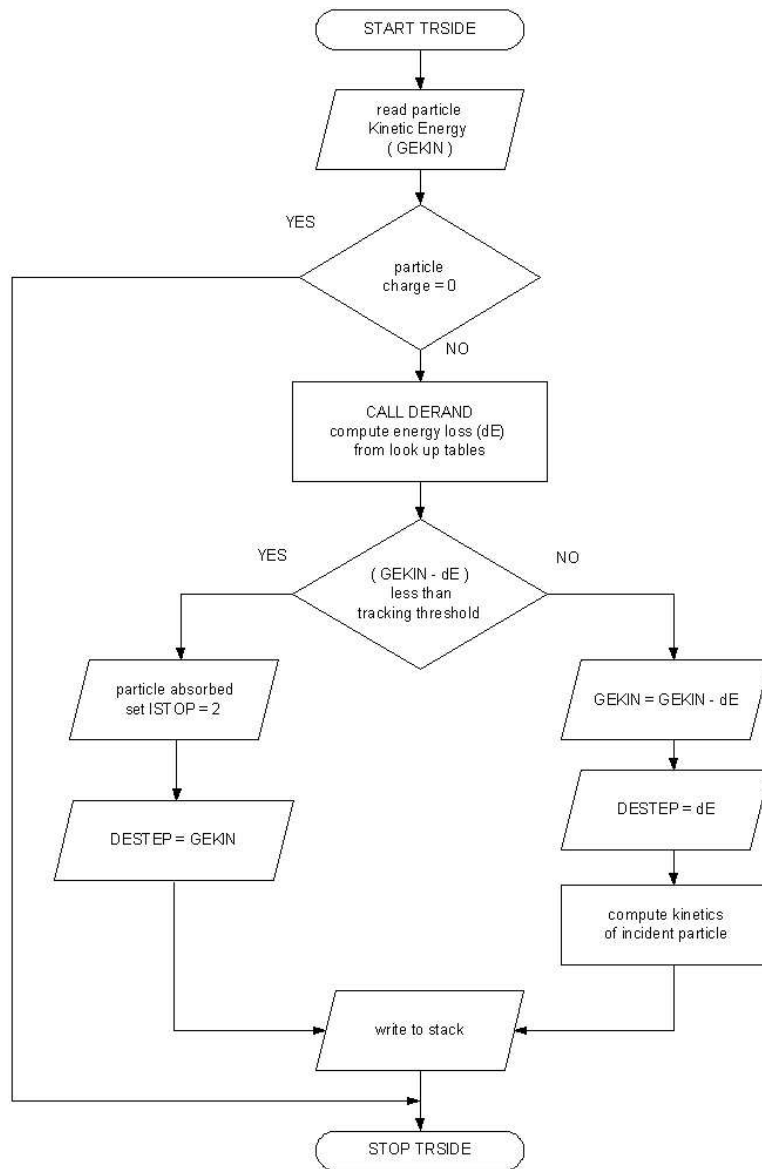


Fig. 5.10: *Simulation programme TRSIDE.F*